Physik - Department

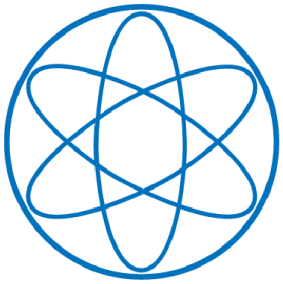

Optical Properties of Liquid Noble Gas Scintillators

Dissertation
von

Alexander Maximilian Neumeier

Technische Universität München

Technische Universität München

Lehrstuhl E15 für Experimentalphysik und Astroteilchenphysik

Optical Properties of Liquid Noble Gas Scintillators

Alexander Maximilian Neumeier

Vollständiger Abdruck der von der Fakultät für Physik der Technischen Universität München zur Erlangung des akademischen Grades eines

Doktors der Naturwissenschaften (Dr. rer. nat.)

genehmigten Dissertation.

Vorsitzender:	Univ.-Prof. Dr. Björn Garbrecht
Prüfer der Dissertation:	1. Univ.-Prof. Dr. Stefan Schönert
	2. Priv.-Doz. Dr. Andreas Ulrich
	3. Prof. Aksel Hallin, Ph.D., University of Alberta, Edmonton, Kanada (nur schriftliche Beurteilung)

Die Dissertation wurde am 29.06.2015 bei der Technischen Universität München eingereicht und durch die Fakultät für Physik am 04.08.2015 angenommen.

Abstract

Liquid noble gases, in particular, argon and xenon are widely used scintillator materials in particle detectors aiming to detect rare events. Due to their high scintillation efficiency, the possibility to be cleaned to a high level of purity, and their scalability to large detector volumes they are a very attractive detector medium for the direct dark matter search, high-energy neutrino physics and the neutrinoless double-beta decay. To reduce background, an event-by-event particle discrimination is mandatory which requires a profound knowledge of the optical scintillator properties. Pure liquid argon and xenon scintillate almost exclusively in the vacuum ultraviolet wavelength region. State of the art detector concepts using the intense vacuum ultraviolet scintillation signals are described and discussed.

Wavelength-resolved studies concerning the emission as well as the transmission of pure and xenon-doped liquid argon are presented. The excitation of the liquid noble gas samples was performed using low-energy (12 keV) electrons (from a conventional cathode ray tube) sent through a thin (300 nm) ceramic membrane into the liquid noble gas samples. Time-resolved studies were obtained by pulsing the electron beam with a pulse duration of 100 ns and performing time-to-amplitude conversion spectroscopy.

Wavelength-resolved emission spectra are presented for a wide wavelength range from 115 - 3500 nm, i.e., from the vacuum ultraviolet to the infrared. The results were obtained using a vacuum-ultraviolet photomultiplier, an InAs infrared photodiode, and a near-infrared photomultiplier.

The scintillation of pure liquid argon is restricted almost exclusively to an intense emission band in the vacuum ultraviolet (127 nm peak wavelength, 7.4 nm full width at half maximum). Under the present experimental conditions (12 keV electron energy) the conversion efficiency for pure liquid argon from electron-beam power to vacuum ultraviolet scintillation light is (21 ± 3) %. This corresponds to a scintillation efficiency of $(22\,000 \pm 3\,000)$ photons per MeV electron energy deposited.

Liquid argon doped with a small amount ($\sim$ 10 parts per million (ppm)) of xenon shows two intense and well separated emission bands in the vacuum ultraviolet (174 nm peak wavelength, 8.6 nm full width at half maximum) and in the near-infrared (1173 nm peak wavelength, 99 nm full width at half maximum). The conversion efficiency from electron-beam power to vacuum ultraviolet light has been determined as (14 ± 4) %. This corresponds to $(20\,000 \pm 6\,000)$ photons per MeV electron energy deposited. In addition, the conversion efficiency of electron-beam power to near-infrared light has been determined as (1.3 ± 0.4) % and the corresponding scintillation efficiency is $(13\,000 \pm 4\,000)$ photons per MeV electron energy deposited. The integral conversion efficiency from electron-beam power to light (vacuum ultraviolet + near-infrared) is (15.3 ± 4.4) %.

The time structures of the vacuum ultraviolet as well as the near-infrared scintillation feature in liquid argon doped with 10 ppm xenon are well suited for an application in a particle detector. The durations are below $\sim 2\,\mu$s in the vacuum ultraviolet and

below $\sim 1.2\,\mu$s in the near-infrared wavelength region. No intense and long-lived scintillation components raising the noise level and the dead time were observed. From a comparison of the time structures it seems that the vacuum ultraviolet emission is a transition in a cascade following the near-infrared emission.

Emission as well as transmission measurements have been performed. A deuterium arc lamp and a cell of a length of 11.6 cm containing liquid noble gas samples were used. The transmitted vacuum ultraviolet light was analyzed with a vacuum ultraviolet spectrometer. Pure liquid argon was fully transparent and showed no absorption features on the current level of sensitivity down to the short wavelength cut-off of the system at 118 nm. For pure liquid argon a lower limit of ~ 1.10 m for the attenuation length for its own scintillation light could be derived.

The transmission of liquid argon doped with different amounts of xenon has also been measured. Three distinct xenon-related absorption features were observed. The center wavelengths of the transmission minima are at 122.2 and 140.0 nm and can be attributed to transitions from the ground state to perturbed (~ 7 nm blue shifted) $^1P_1$ (n=1, $^2P_{\frac{1}{2}}$) and $^3P_1$ (n=1, $^2P_{\frac{3}{2}}$) atomic xenon states. The third transmission minimum is centered at 126.5 nm and can be attributed to a n=2 ($^2P_{\frac{3}{2}}$) trapped exciton (Wannier-Mott) impurity state which has no parentage in the states of isolated xenon atoms. A transition from the n=2 ($^2P_{\frac{3}{2}}$) trapped exciton (Wannier-Mott) impurity state to the $^3P_1$ (n=1, $^2P_{\frac{3}{2}}$) perturbed atomic xenon state is assumed to be reponsible for the newly-discovered near-infrared emission. A model explaining the intense near-infrared emission is proposed and experiments to prove the model are suggested.

The last part of the thesis is a proposal for a novel particle identification concept based on a simultaneous detection of vacuum ultraviolet and near-infrared signals in xenon-doped liquid argon. A scintillator with two optically well separated scintillation signals could pave the way towards a new and powerful particle identification concept if it turns out that both scintillation signals (vacuum ultraviolet and near-infrared) are strongly particle-dependent and xenon-doped liquid argon is suited for an application in a particle detector.

Zusammenfassung

Flüssige Edelgase, vor allem Argon und Xenon, sind weit verbreitete Szintillatormaterialien in Teilchendetektoren, welche auf die Detektion von seltenen Ereignissen ausgelegt sind. Aufgrund der hohen Szintillationseffizienz, der intrinsischen Reinheit und der Skalierbarkeit zu großen Detektorvolumina sind sie ein attraktives Szintillationsmedium in Teilchendetektoren, die bei der direkten Suche nach dunkler Materie, der Hochenergie-Neutrinophysik und dem neutrinolosen Doppel-Beta-Zerfall eingesetzt werden. Die Diskriminierung zwischen Untergrund und Signal wird mittels einer event-by-event Teilchenidentifikation realisiert, welche fundiertes Wissen über die optischen Szintillationseigenschaften voraussetzt. Die Lichtemission von reinem flüssigen Argon bzw. Xenon beschränkt sich fast ausschließlich auf den vakuumultravioletten Spektralbereich. Der Stand der Technik der Teilchendetektoren, welche diese intensive Szintillation im vakuumultravioletten Spektralbereich nutzen, wird erläutert und diskutiert.

Es werden wellenlängenaufgelöste Studien, sowohl über die Emission als auch über die Transmission, von reinem und xenon-dotiertem flüssigen Argon präsentiert. Die Anregung der flüssigen Edelgase wurde mit niederenergetischen (12 keV) Elektronen einer konventionellen Kathodenstrahlröhre durchgeführt. Die Elektronen wurden durch eine dünne (300 nm) Keramikmembran in die flüssigen Edelgasproben eingekoppelt. Zeitaufgelöste Szintillationsspektren wurden mit einem gepulsten Elektronenstrahl (Pulsdauer 100 ns) und einer Zeit-zu-Amplituden-Konversion aufgenommen.

Es werden wellenlängenaufgelöste Emissionsspektren in einem weiten Bereich von 115 - 3500 nm (vom vakuumultravioletten bis zum infraroten Spektralbereich) präsentiert. Die Ergebnisse wurden durch die Kombination eines Vakuumultraviolett-Photomultipliers, einer InAs-Infrarot-Photodiode und eines Nahinfrarot-Photomultipliers gewonnen.

Die Szintillation von reinem flüssigen Argon ist fast ausschließlich auf eine intensive Emissionsstruktur im vakuumultravioletten Spektralbereich beschränkt (127 nm Peakwellenlänge, 7.4 nm Halbwertsbreite). Unter den gegebenen experimentellen Bedingungen (12 keV Elektronenenergie) wurde die Konversionseffizienz von eingekoppelter Elektronenstrahlleistung zu vakuumultraviolettem Licht zu $(21 \pm 3)\,\%$ bestimmt. Das entspricht einer Szintillationseffizienz von $(22\,000 \pm 3\,000)$ Photonen pro MeV deponierter Elektronenenergie.

Schwach Xenon-dotiertes (~ 10 ppm (parts per million)) flüssiges Argon zeigt zwei intensive und optisch gut getrennte Emissionsstrukturen im vakuumultravioletten (174 nm Peakwellenlänge, 8.6 nm Halbwertsbreite) und im nahinfraroten (1173 nm Peakwellenlänge, 99 nm Halbwertsbreite) Spektralbreich. Die Konversionseffizienz von eingekoppelter Elektronenstrahlleistung zu vakuumultraviolettem Licht wurde zu $(14 \pm 4)\,\%$ bestimmt. Das entspricht einer Szintillationseffizienz von $(20\,000 \pm 6\,000)$ Photonen pro MeV deponierter Elektronenenergie. Zusätzlich wurde die Konversionseffizienz von eingekoppelter Elektronenstrahlleistung zu nahinfrarotem Licht zu einem Wert von $(1.3 \pm 0.4)\,\%$ bestimmt. Das entspricht einer Szintillationseffizienz

von $(13\,000 \pm 4\,000)$ Photonen pro MeV deponierter Elektronenenergie. Die integrale Gesamtlichtausbeute (Vakuumultraviolett + Nahinfrarot) beträgt $(15.3 \pm 4.4)\,\%$.

Die Zeitstrukturen der Emissionen von flüssigem Argon dotiert mit $\sim 10\,\mathrm{ppm}$ Xenon sind sehr gut für eine Anwendung in Teilchendetektoren geeignet. Beide Szintillationssignale haben eine Dauer, die nicht länger als $\sim 2\,\mu\mathrm{s}$ im Falle der Emission im vakuumultravioletten und nicht länger als $\sim 1.2\,\mu\mathrm{s}$ im Falle der Emission im nahinfraroten Spektralbereich ist. Es wurden keine intensiven und langlebigen Szintillationsstrukturen gefunden, die das Untergrundrauschen und die Totzeit erhöhen würden. Ein Vergleich der Zeitstrukturen beider Emissionen zeigt, dass die vakuumultraviolette Emission ein Folgeübergang der nahinfraroten Emission innerhalb einer Kaskade sein könnte.

Neben Emissionsmessungen wurden auch Transmissionsmessungen durchgeführt. Eine Deuteriumlampe wurde benutzt, um eine Zelle mit einer Länge von 11.6 cm, die die Flüssig-Edelgasproben enthielt, zu durchleuchten. Das transmittierte vakuumultraviolette Licht wurde mit einem Vakuumultraviolettspektrographen analysiert. Reines flüssiges Argon war absolut transparent und zeigte innerhalb der gegenwärtigen Sensitivität keinerlei Absorptionsstrukturen bis hin zum kurzwelligen Ende des sensitiven Wellenlängenbereichs der Apparatur bei 118 nm. Eine Untergrenze für die Abschwächlänge von reinem flüssigen Argon für sein eigenes Szintillationslicht konnte zu $\sim 1.10\,\mathrm{m}$ bestimmt werden.

Die Transmission von xenon-dotiertem flüssigen Argon wurde ebenfalls gemessen. Es wurden drei ausgeprägte Absorptionsstrukturen beobachtet, welche Xenon zugeordnet werden können. Die Mittenwellenlängen der Transmissionsminima sind bei 122.2 und 140.0 nm. Diese Transmissionsminima können Übergängen vom Grundzustand zu gestörten (7 nm blau-verschobenen) $^1P_1$ (n=1, $^2P_{\frac{1}{2}}$) bzw. $^3P_1$ (n=1, $^2P_{\frac{3}{2}}$) atomaren Xenon-Zuständen zugeordnet werden. Das dritte Transmissionsminimum hat eine Mittenwellenlänge von 126.5 nm und kann einem n=2 ($^2P_{\frac{3}{2}}$) Wannier-Mott-Exciton zugeordnet werden. Zu dem Wannier-Mott-Exciton gibt es keinen assoziierten Zustand im Falle von isolierten Xenon-Atomen. Ein Übergang eines n=2 ($^2P_{\frac{3}{2}}$) Wannier-Mott-Excitons zum gestörten $^3P_1$ (n=1, $^2P_{\frac{3}{2}}$) atomaren Xenon-Zustand könnte die Ursache für die kürzlich entdeckte intensive Emission im nahinfraroten Spektralbereich sein. Ein Modell, welches die intensive Emission im nahinfraroten Spektralbereich erklärt, wird vorgestellt und Experimente, um das Modell zu überprüfen, werden vorgeschlagen.

Der letzte Teil der Arbeit beschäftigt sich mit einem Vorschlag für ein neuartiges Teilchendetektorkonzept, welches den simultanen Nachweis der Emissionen von Xenon-dotiertem flüssigen Argon im vakuumultravioletten und im nahinfraroten Spektralbereich vorsieht. Ein Szintillator mit zwei optisch gut getrennten Lichtemissionen könnte zu einem neuen und sehr effizienten Teilchenidentifizierungskonzept führen, wenn sich herausstellt, dass beide Signale (im vakuumultravioletten und im nahinfraroten Spektralbereich) stark vom Projektil abhängen, welches die Szintillation hervorruft.

Contents

Preface

A major part of the following work has already been published in scientific journals. In case the reader's focus is only on specific aspects of this thesis, the results can also be found in the following publications:

A. Neumeier et al. ***"Intense vacuum ultraviolet and infrared scintillation of liquid Ar-Xe mixtures".***
Europhys. Lett. 109 12001, 2015 (editor's choice)
This letter describes the vacuum ultraviolet emission of xenon-doped liquid argon under low-energy electron-beam excitation. The scintillation efficiencies and time structures of the vacuum ultraviolet as well as the near-infrared emissions are presented. A comparison with pure liquid argon is provided. A novel detector concept using both scintillation signals simultaneously is discussed.

A. Neumeier et al. ***"Intense infrared scintillation of liquid Ar-Xe mixtures".***
Europhys. Lett. 106 32001, 2014 (editor's choice)
This letter describes the main result of the present thesis: The discovery of an intense near-infrared emission of xenon-doped liquid argon under low-energy electron-beam excitation; the scintillation efficiency has been determined and a possible application for a novel particle identification concept is discussed.

A. Neumeier et al. ***"Attenuation of vacuum ultraviolet light in liquid argon revisited".***
Nucl. Instrum. Methods Phys. Res. A, 2015,
http://dx.doi.org/10.1016/j.nima.2015.07.051
This is a technical paper which presents and describes issues related to transmission measurements in a more general sense. The transmission of a sample of pure liquid argon with a length of the optical path of 11.6 cm is presented. No xenon-related absorption features were discovered and a lower limit for the attenuation length of pure liquid argon for its own scintillation light is provided.

A. Neumeier et al. ***"Attenuation of vacuum ultraviolet light in pure and xenon-doped liquid argon - An approach to an assignment of the near-infrared emission from the mixture".***
Europhys. Lett. 111 12001, 2015 (editor's choice)
This is a publication which summarizes the results on the attenuation length of pure liquid argon for its own scintillation light. In addition, transmission data of xenon-doped liquid argon are presented and compared with pure liquid argon. The results are used as a hint for the identification of energy transfers from argon to xenon.

A. Neumeier et al. ***"Attenuation of vacuum ultraviolet light in liquid argon".***
Eur. Phys. J. C 72:2190, 2012
This publication presents wavelength-resolved transmission measurements of pure liquid argon. The optical path length of the sample cell was 5.8 cm. Xenon-related absorption features could be identified.

Alexander Neumeier
27.08.2015

Chapter 1

Introduction

1.1 Noble Gases - Highly Efficient Scintillators

It is known since the 1950s that discharge plasmas in low-pressure noble gases emit light in the so-called vacuum ultraviolet (VUV) spectral region ($\lambda < 200\,\mathrm{nm}$) [1, 2, 3, 4, 5]. The different light-emission processes are well studied and even led to the application of electron-beam induced noble-gas plasmas in excimer lasers [6, 7, 8].

Particle beams are a further approach besides discharges to generate plasmas in noble gases [9]. In the present thesis, low-energy (12 keV) electron beams sent through very thin (300 nm) ceramic membranes [10, 11, 12] are used to generate excited noble gases (in the gas and in the liquid phase). The light emission (scintillation) following electron-beam excitation is studied wavelength and time resolved.

Fig. 1.1 shows wavelength-resolved VUV emission spectra of electron-beam excited noble gases from helium to xenon at room temperature and at a pressure of 1000 mbar [13]. The conversion efficiency from electron-beam power to VUV light is $\sim 30\,\%$ for neon and argon and $\sim 40\,\%$ for krypton and xenon [14]. These high scintillation efficiencies, which are virtually constant in a pressure range from 500 to 1400 mbar, (and above) have even led to the application of electron-beam excited noble gases in VUV light sources [10, 12]. In the VUV there are only few alternatives for efficient light production in table-top setups.

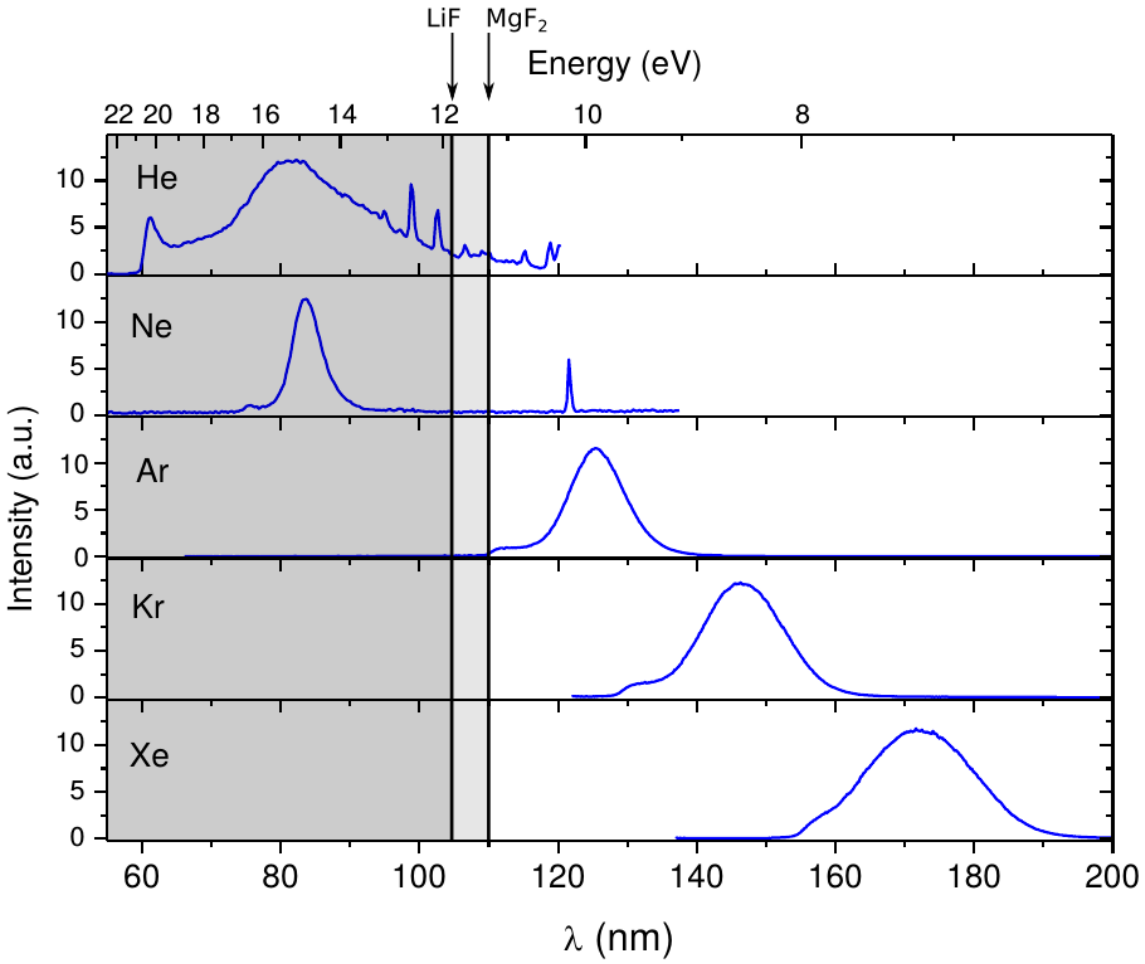

Figure 1.1: *Scintillation spectra of electron-beam excited gaseous He, Ne, Ar, Kr, and Xe at a pressure of* 1000 *mbar are shown (blue lines) [13]. The vertical black lines indicate the cut-off wavelengths of LiF and* MgF_2 *which are window materials that are widely used in vacuum ultraviolet spectroscopy. To observe the emission in the gray-shaded region a windowless light-detection technique has to be used. The small peak at 121 nm in the neon spectrum is due to a residual hydrogen impurity (Lyman-alpha line of hydrogen).*

1.2 Liquid Noble Gases - Applications in Rare Event Physics

From the last decades until now liquid noble gases have gained more and more attention as a detector medium [15]. Especially in the sector of rare event physics such as the direct search for dark matter [16, 17, 18, 19, 20, 21], high-energy neutrino physics [22, 23], and the search for the neutrinoless double-beta decay [24, 25, 26, 27] liquid noble gases are used extensively. Detailed overviews of the status of the direct search for dark matter using liquid noble gases in general can, e.g., be found in ref. [28] and more focused on xenon in ref. [29] and references therein.

Due to their high scintillation yield, the possibility to be cleaned to a high level of purity and their scalability to large detector volumes[1] liquid noble gases are a very attractive scintillator material for particle detectors. Cleaning here has to be understood in two ways. Liquid noble gases have to be cleaned chemically since impurities like water or oxygen lead to luminescence-light losses because of additional quenching and absorption processes [30]. The time structures of the scintillation light [31] are also affected by some impurites leading to a decreased particle discrimination potential especially in the case of single phase detectors (see subsection 1.3.1). In time projection chambers (TPCs, see subsection 1.3.2) oxygen, in addition, captures free electrons and thereby diminshes the ionization signal [30]. Also traces of xenon in pure liquid argon detectors lead to a severe change of the emission [32] and transmission [33] spectrum as well as the time structure [32] (see section 3.5). A further constraint on the purity is in terms of radioactivity, the so-called radiopurity. A high radiopurity leads to a low background and, thus, to a higher sensitivity.

However, due to technical reasons not all noble gases are suited as detector medium. Helium and neon[2] have boiling temperatures below the temperature of liquid nitrogen (LN_2, 77 K [34]) which makes cooling more expensive. One additional drawback is that their scintillation light is emitted to a great extent below 90 nm where no transparent window materials are available. Krypton is basically a suitable candidate for particle detectors, but it contains non-negligible amounts of the radioactive isotope ^{85}Kr which is a beta emitter with a half-life of 10.75 years and Q-value of 687 keV [35]. Argon, on the other hand, is a suitable candidate and, since it is the third most abundant gas in the atmosphere, very cheap. However, atmospheric argon contains cosmogenic ^{39}Ar which is a beta emitter with a half-life of 269 years and a Q-value of 565 keV [36]. This leads to an upper limit for liquid argon detector volumes due to pile-up. Therefore, for large liquid argon detectors, depleted argon from underground sources is conceived [37]. Xenon is also a suitable candidate but very expensive due to its very low abundance (in the atmosphere). In summary most of the projects in rare event physics focus either on argon or on xenon.

The large atomic mass difference between argon and xenon is advantageous for

[1] Ton-scale projects are currently under construction [28, 29] and multi-ton projects are conceived [21].

[2] One exception is MiniCLEAN [18] which is designed to interchange its targets between liquid argon and liquid neon.

the direct dark matter search: the energy transfer from a WIMP[3][38] recoiling off a target nucleus of the detector medium is - for kinematic reasons - maximal for target nuclei which have an atomic mass of the order of the WIMP mass. Therefore, different target media (e.g. argon and xenon as a complement to each other) with different atomic masses allow to cover a wider mass range in the WIMP search.

1.3 Liquid Noble Gas Scintillation Detectors - State of the Art

To observe such rare events like a WIMP transferring some momentum to a target nucleus, detectors with a low energy threshold (few keV) and a high particle discrimination power based on an event-by-event basis are mandatory. The crucial discrimination has to be performed between electron recoils, primarily induced by β and γ radiation[4], and nuclear recoils. In the case of nuclear recoils, neutrons are the most dangerous background since they can not be discriminated from a WIMP if they interact only once with a target nucleus within the detector. However, neutrons have a high probability to interact several times inside a detector and can be rejected if the individual interactions can be resolved. Therefore, these particle detectors are usually located deep underground to be shielded from cosmic rays and additional veto detectors surround the inner detector volume to tag atmospheric muons. The detectors are usually built from selected and screened radiopure materials. Fiducialization of the detector volumes restricts the sensitive detector volumes to the innermost part to get rid of events caused by the radioactivity of the housing and of the surrounding light detectors.

At the moment, basically two different liquid noble gas detector concepts (see subsections 1.3.1 and 1.3.2) are widely used and considered to be state of the art.

1.3.1 Single-Phase Detectors

Single-phase detectors have conceptionally a very straightforward design which is illustrated in Fig. 1.2. A large spherical volume of liquid noble gas is observed by light sensors, usually photomultipliers. The spherical geometry leads to a high optical coverage of the detector with photomultipliers. A high optical coverage decreases the threshold and, therefore, increases the sensitivity. Due to the spherical geometry also a rough event vertex reconstruction with a resolution of typically a few cm can be performed [28]. Particle discrimination is based only on the time structure of the signal. To get an idea of the expected pulse shapes in a liquid argon detector, Fig. 1.3 shows, for example, the scintillation time-structure measurements of pure liquid argon excited with a pulsed proton beam compared to a pulsed sulfur beam [39, 40].

[3]WIMP - **W**eakly **I**nteracting **M**assive **P**article: Hypothetical particle postulated to solve the cosmological dark matter problem.

[4]Which is the most abundant background for almost all experiments.

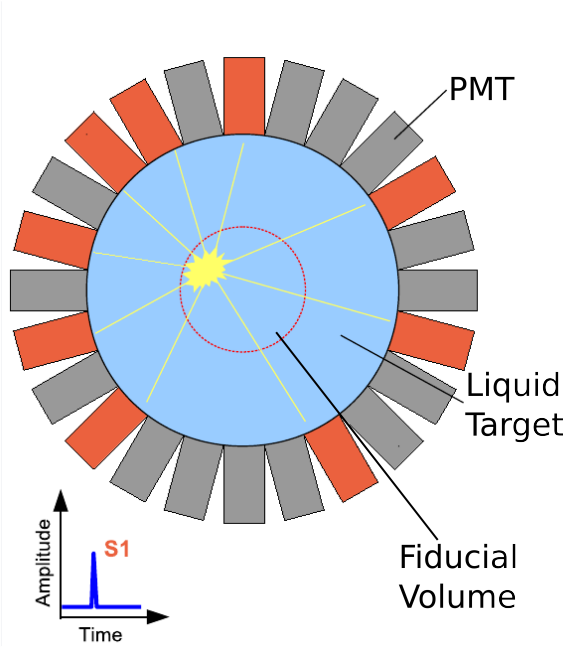

Figure 1.2: *The concept of a single-phase liquid noble-gas detector is illustrated. The spherical liquid noble-gas volume is surrounded by photomultipliers (PMTs). To reduce the background a fiducial volume is defined where events are accepted. The particle discrimination is based only on the time information indicated by the small illustration (S1) in the lower left corner. This figure is adapted from ref. [28].*

1.3.2 Double-Phase Detectors or Time Projection Chambers (TPCs)

Double-phase detectors (see Fig. 1.4) perform particle discrimination based on the simultaneous measurement of the scintillation light and the charge produced in an interaction. The detectors usually have a cylindrical shape where the top and the bottom are equipped with light sensors, usually photomultipliers (PMTs). The detector is not completely filled with liquid noble gas but on top the noble gas is kept in the gas phase. A particle interaction within the detector leads to a prompt scintillation signal denoted by S1 in Fig. 1.4. A strong electric field ($\sim 1\frac{\mathrm{kV}}{\mathrm{cm}}$) drifts the charge released in the interaction towards the upper gas-liquid phase-transition. When the electrons are extracted from the liquid and accelerated in the gas phase a second scintillation signal indicated by S2 in Fig. 1.4 is observed. This signal is proportional to the charge produced in the initial interaction. The light pattern on the top sensor array is used to derive the (x,y)-position, and the time difference between S1 and S2 times the drift velocity is used to derive the z-coordinate. This detector has a very good vertex reconstruction and, therefore, a powerful background rejection via fiducialization and multi-scatter identification. However, due to the decreased optical coverage compared to single-phase detectors the threshold can be worse than in a single-phase detector. A further drawback is the electric field which leads to technical

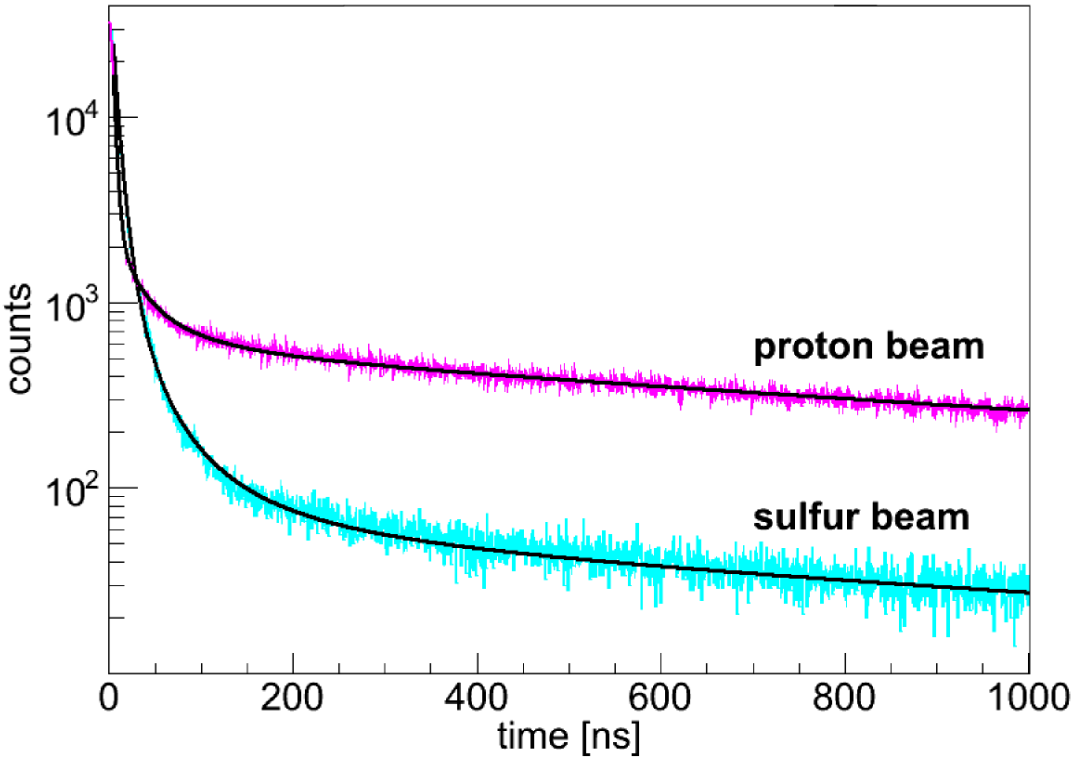

Figure 1.3: *The scintillation time spectra of pure liquid argon at the most intense emission wavelength of 127nm are shown for different ion beams. The spectra were scaled to match each other at t=0. The excitation with a proton beam leads to an enhanced slow component while the fast component has a shorter time constant compared to excitation with a sulfur beam. For further details see ref. [40] from where this figure has been adapted.*

difficulties with very high voltages when the detector volumes are increased [28].

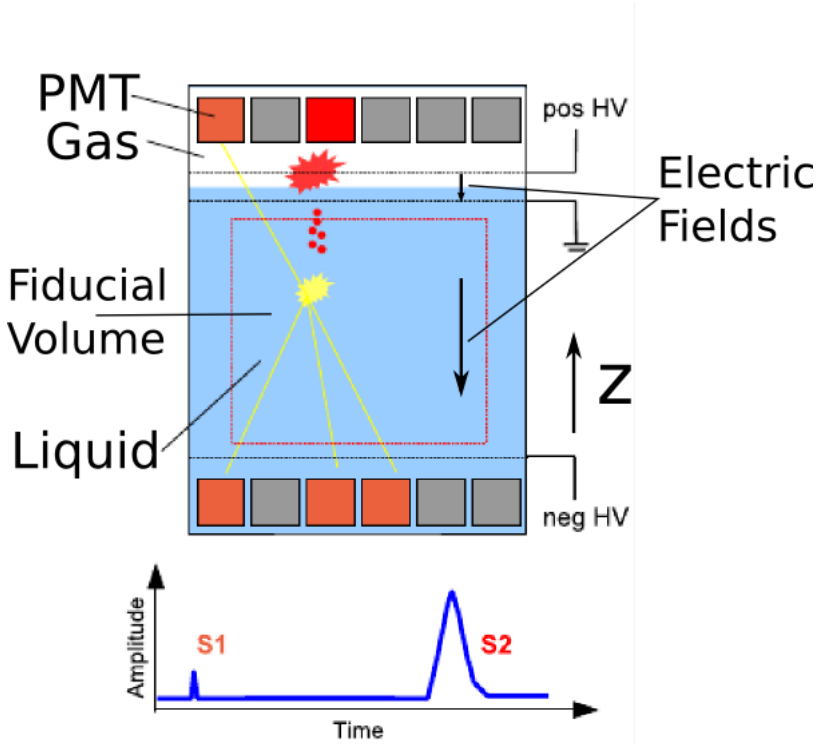

Figure 1.4: *The concept of a double phase noble gas detector is illustrated. The cylindrical detector volume is equipped on top and bottom with light sensors, usually PMTs. The particle discrimination is based on the simultaneous measurement of the light and the charge produced in an interaction. S1 corresponds to the first scintillation signal and S2 corresponds to the second scintillation signal which is proportional the charge released in the interaction. Electric fields accelerate the electric charges produced in a particle interaction. This figure is adapted from ref. [28].*

1.4 Scintillation Mechanism in the Vacuum Ultraviolet

A detailed explanation of the scintillation mechanism in the VUV can, e.g., be found in section 9.1 in ref. [39], in chapter two in ref. [41] and in section 2.2 in ref. [42]. Therefore, the whole mechanism is not repeated here in detail and the focus is solely on the important aspects.

Argon is chosen as a representative for all noble gases, but the mechanisms are similar for the other noble gases with s^2p^6 outer shell electron-configuration: neon through radon. Liquid noble gases will be described in the present work as a very dense gas whose scintillation mechanism is well examined. This assumption is supported by the fact that the spectrum of the emitted scintillation light in the liquid phase has been found to be very similar to that of the gas phase for excitation with electrons [31, 41, 43, 44], synchrotron radiation [45], α-particles [46, 47] and ion beams [40].

The emission spectrum which is observed when an incident particle interacts electromagnetically with argon atoms is strongly dependent on the density, i.e. the collision rate between the argon atoms. The electron-beam induced emission spectra of gaseous and liquid argon are shown in Fig. 1.5 and the corresponding excimer potential is depicted in Fig. 1.6. The different emission features can be understood within the potential diagram as follows: An incident particle which interacts with argon atoms leads either to ionized[5] or excited atoms. If the gas is very dilute, there is a low density of (or large mean internuclear distance between) argon atoms and the optical transition probability of the excited atoms to undergo a transition to the ground state is high compared to the collision probability with another argon atom. Therefore, the excited atoms decay back to the ground state thereby emitting[6] the characteristic resonance emission [49] at wavelengths of 104.8 and 106.7 nm [50]. Increasing the density leads to an increasing collision rate of excited argon atoms with atoms in the ground state. This increased collision rate can lead to the formation of strongly bound two-atomic argon molecules. These molecules are only bound in the excited state which can be seen by the attractive potential in Fig. 1.6. These molecules are called excited dimers or shortly excimers. The excimers exist in two states (singlet $Ar_2^*(^1\Sigma_u^+)$ or triplet $Ar_2^*(^3\Sigma_u^+)$ states). The excimer molecules are formed in different vibrationally excited states (represented as blue and red horizontal lines in the potential well in Fig. 1.6) before they decay to the ground state ($Ar_2^*\left(^1\Sigma_g^+\right)$). Transitions near the minimum form the so-called second continuum which is the dominant feature in the emission spectra centered at $\sim$ 127 nm (see Fig. 1.5) with a width of 7-10 nm (depending also on temperature [31]) for argon. The transitions are represented as blue solid (singlet) and red dashed (triplet) arrows. After the transition to the repulsive ground state the molecule separates into two neutral argon atoms.

The mean internuclear distance in the liquid phase is 3.6 Å [51] and indicated by the green dashed vertical line in Fig. 1.6. In the ground state potential there exists also a weak Van-der-Waals binding at a mean internuclear distance of 3.75 Å with a depth of approximately 12 meV [52]. Integrating the Boltzmann energy distribution of argon atoms at 86 K (liquid argon temperature) from zero to 12 meV leads to the conclusion that 65 % of all argon atoms in liquid argon have a thermal energy lower than the depth of the Van-der-Waals minimum. However, since the potential minimum of the excimer potential is at a mean internuclear distance of $\sim$ 2.4 Å there exists no bound ground state and the decaying argon excimers separate to two neutral argon atoms due to the strongly repulsive ground state potential. Thus, there is no reabsorption and argon should be highly transparent for its own scintillation light which is an important feature for a scintillator. Detailed and wavelength-resolved investigations of the transmission of VUV light in liquid argon can be found in refs. [33, 53].

Two additional emission features which are due to transitions from highly excited

[5] In the liquid phase excited atoms can be treated as quasi-free excitons and ionized atoms as electron-hole pairs [48].

[6] It has to be mentioned that resonance emission can actually only be observed if the light can leave the argon volume. Reabsorption leads to so-called "radiation trapping" which means that the light is absorbed again before it leaves the argon volume. Therefore, resonance emission can only be observed at very low argon pressures and in argon mixtures.

vibrational states have been observed in spectroscopic investigations of gaseous argon: The so-called first continuum [54] and the classical left turning point (LTP) [55]. A descriptive explanation can be derived from a consideration of the vibrational motion of the excited excimer molecules in a classical way. The motion shows two reversal points with temporarily increased probability of prescence. If an excimer molecule deexcites in the vincinity of the point of reversal with a large internuclear distance photons with higher energy and, thus, shorter wavelengths are emitted. This feature is the so-called first continuum. If an excimer molecule deexcites in the vincinity of the point of reversal with a small internuclear distance, photons with lower energy and, thus, longer wavelengths are emitted. This emission feature is called the classical left turning point (LTP) and can be seen in the spectrum in Fig. 1.5 in the gas phase at 155 nm.

A third additional emission feature can be seen in Fig. 1.5 in a wavelength region from $\sim (170 - 230)$ nm. This is the so-called third continuum [56, 57]. This emission feature originates from ionic excimers undergoing transitions at higher lying energy levels than those depicted in Fig. 1.6. The region of these transitions is indicated by the vertical arrow on top of Fig. 1.6. A detailed assignment of the different transitions and reaction chains can be found in ref. [58].

Wavelength-resolved studies of the emission of pure liquid argon using different incident ion beams showed that a particle discrimination based on the wavelength information alone is not feasible in any real detector [39, 40]. However, the time structure of the scintillation light can be used for particle discrimination which is briefly explained in the following: The singulet and the triplet excimers have different decay time constants (singlet: τ= 4.4 - 6 ns, triplet: τ= 1.1 - 1.7 μs [31, 59, 60]). The intensity ratio of singlet to triplet excimers depends on the excitation conditions (e.g., the incident particle) [39, 40] and leads to particle dependent scintillation time structures (pulse shapes). This feature is used, for example, in single-phase detectors to perform particle discrimination on an event-by-event basis.

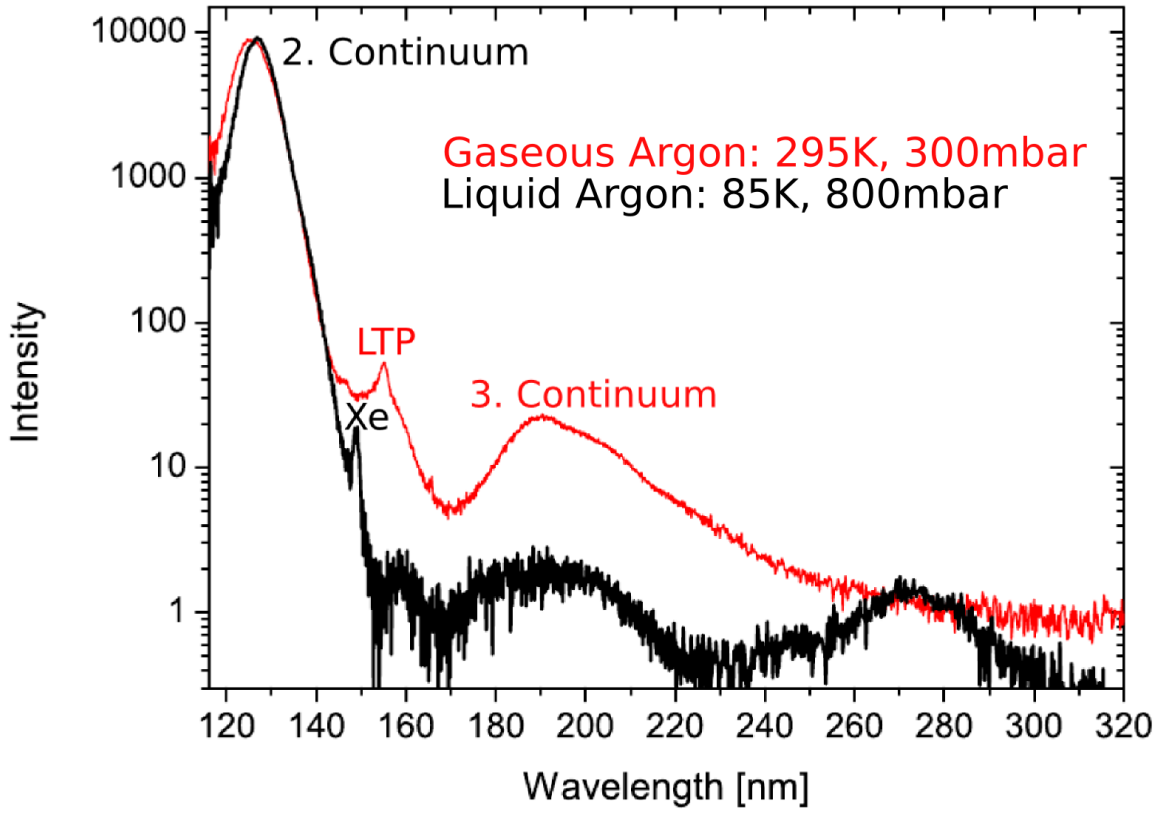

Figure 1.5: *The electron-beam (12 keV, 1.5 μA) induced VUV emission spectra of pure gaseous (red curve, 295 K, 300 mbar) and pure liquid (black curve, 85 K, 800 mbar) argon are shown. In the liquid as well as in the gas phase, the by far most dominant emission feature is the so-called second continuum emission at* $\sim$ 127 *nm peak wavelength. The emission feature in the gas phase at 155 nm is the so-called classical left turning point (LTP). The peak at 149 nm in the liquid phase is caused by a xenon impurity. At wavelengths longer than* $\sim$ 170 *nm the so-called third continuum is formed. The data have been adapted from ref. [44].*

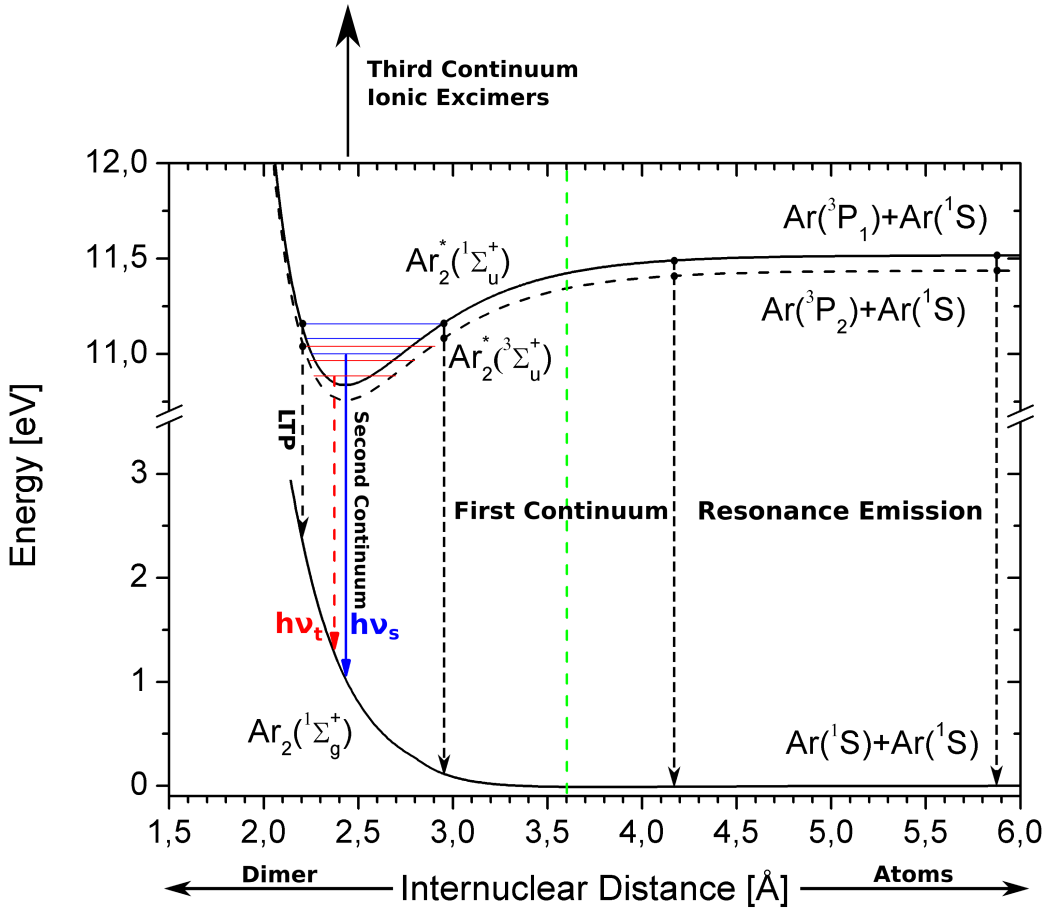

Figure 1.6: *The argon excimer molecule potentials [45, 61] and the corresponding emission processes are shown. The molecule potentials are dependent on the internuclear distance. The lower black curve exhibits the repulsive ground state potential. The green dashed vertical line denotes the mean internuclear distance of argon atoms in the liquid phase. The Van-der-Waals minimum at 3.75 Å (depth 12 meV) is not visible on the current energy axis. The upper solid black curve shows the potential of the singlet excimer ($Ar_2^*(^1\Sigma_u^+)$) formed by a neutral argon atom ($Ar(^1S)$) and an excited argon atom ($Ar(^3P_1)$). The upper dashed black curve shows the potential of the triplet excimer ($Ar_2^*(^3\Sigma_u^+)$) formed by a neutral argon atom ($Ar(^1S)$) and an excited argon atom ($Ar(^3P_2)$). At low collision rates (large internuclear distances) resonance emission can be observed. Increasing the density leads to the formation of excimer molecules in different vibrationally excited states (red and blue horizontal lines). A subsequent transition of the vibrationally relaxed excimer molecules leads to the dominant second continuum emission at ∼ 127 nm peak wavelength in Fig. 1.5. The decay of vibrationally excited excimers leads to the formation of the so-called first continuum and the classical left turning point (LTP). According to the Franck-Condon principle [62, 63] all transitions happen vertically. The third continuum originates from transitions in ionic excimers in higher lying energy levels (not shown here).*

1.5 A Discovery - Intense Infrared Emission from Xenon-doped Liquid Argon

Usually the VUV scintillation light in the detectors described above is detected by photomultipliers coated with wavelength shifters. These wavelength shifters absorb the VUV light and reemit light in the visible range which is subsequently detected by the photomultipliers. Thereby, the information on the initial light emission is only available wavelength integrated and convoluted with the time structure of the wavelength shifter.

The main goal of this work was to study the primary undisturbed scintillation light of pure liquid argon and especially liquid argon-xenon mixtures, wavelength and time resolved in a wide wavelength range from the vacuum-ultraviolet to the infrared (IR). This project has been motivated by the development of a new particle-identification concept for liquid noble gas detectors.

There were some hints in the literature that pure liquid argon scintillates also in the infrared [64, 65, 66, 67]. Also in a former work of our group (see Fig. 2 in ref. [44] and Fig. 1.7 of the present thesis) there was an increased signal at $\sim 970\,\mathrm{nm}$ close to the cut-off wavelength of the detection system. It was difficult to judge whether this emission feature was a real signal or just an artifact due to the responsivity correction of the detection system.

Therefore, a new detection and readout system was set up to extend the sensitive region of the experimental setup into the infrared region. Briefly, the light detectors (VUV photomultiplier and compact grating spectrometer) from the measurements presented in refs. [31, 41, 44]) were replaced by a thermoelectrically cooled indium arsenide (InAs) photodiode which has a sensitive region from 500 - 3500 nm. The light from the scintillating liquid noble gases was chopped and the signal from the InAs photodiode amplified (transimpedance preamplifier) and read out in a lock-in configuration for noise reduction. The results are presented in Fig. 1.8.

The lower panel in Fig. 1.8 shows the emission of pure liquid argon reached only after several distillation procedures to remove xenon from argon. The upper panel shows the infrared emission of liquid argon doped with 10 ppm xenon. Hence, the first important result is that no infrared emission from pure liquid argon has been detected with the InAs photodiode.

The second important result is that doping pure liquid argon with xenon results in an intense, asymmetrically shaped and broad emission in the near-infrared (NIR) with a peak wavelength of 1173 nm (FWHM: 99 nm). This emission could lead to a new particle discrimination principle based on the simultaneous detection of VUV and NIR scintillation in xenon-doped liquid argon [32, 68][7].

[7] Both results were published and elected to EPL highlight publications (editor's choice) in 2014 and 2015, respectively.

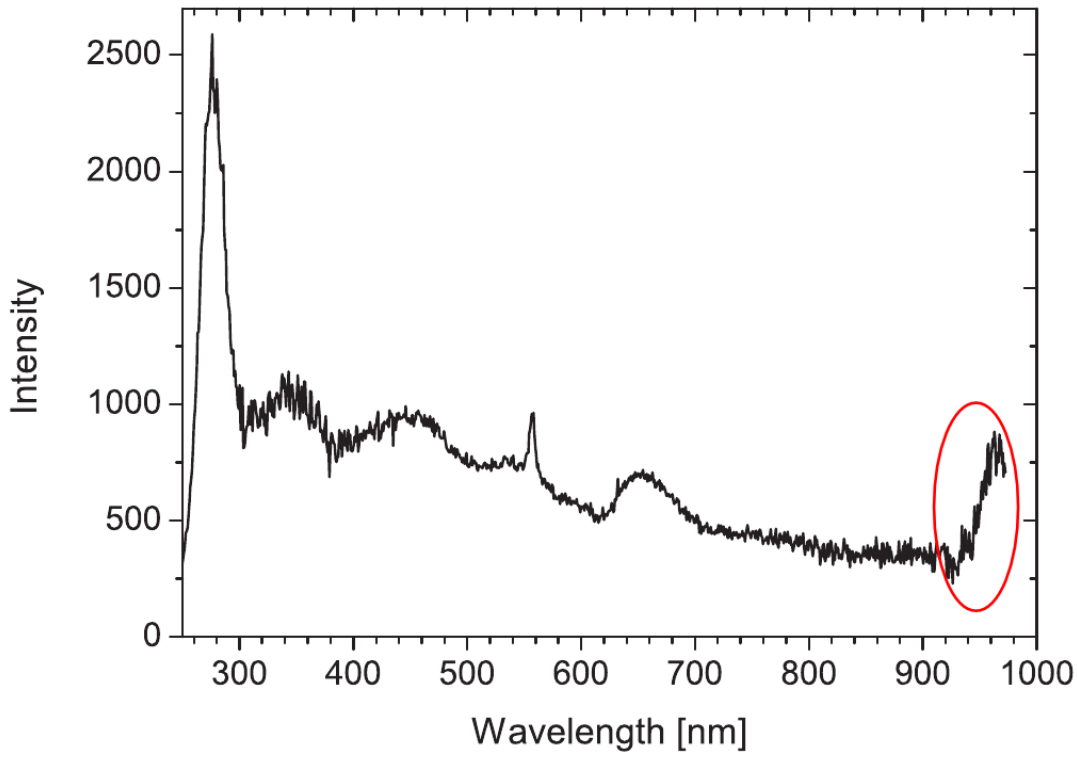

Figure 1.7: *The emission spectrum of electron-beam excited liquid argon from 250 - 970 nm is shown. The emission structure at 270 nm is also visible in Fig. 1.5. The red ellipsis close to the cut-off wavelength of the detection system indicates that pure liquid argon might have strong emission features in the near-infrared. The data have been adapted from ref. [44].*

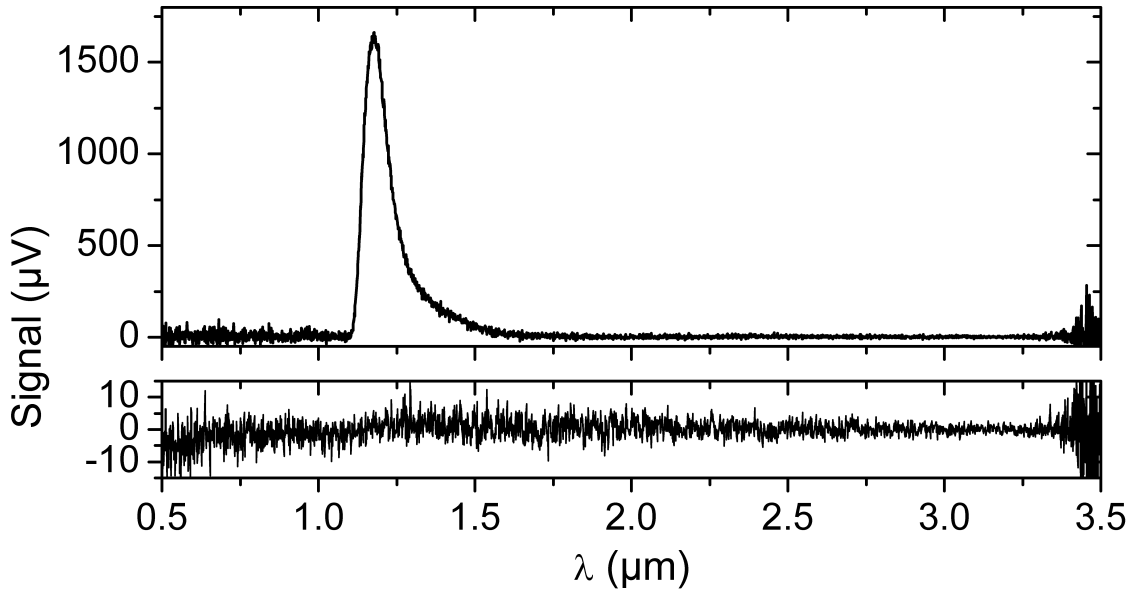

Figure 1.8: *The electron-beam induced scintillation of liquid argon doped with 10 ppm xenon (upper panel) and of pure liquid argon (lower panel) is shown. Pure liquid argon shows no emission from 500 to 3500 nm on the current level of sensitivity. Doping liquid argon with a small amount of xenon leads to an intense emission in the near-infrared. Note that the y-axis of both panels can be compared absolutely. The sensitivity of the setup was strongly increased in the measurement of pure liquid argon compared to xenon-doped liquid argon. Hence, a possible NIR emission from pure liquid argon has to be a factor of* ~ 150 *lower compared to xenon-doped liquid argon. The data have been adapted from ref. [68].*

Chapter 2

Experimental Setup

The excitation method for liquid noble gases which has been used in the experiments described in this work had been developed in the dissertation of Thomas Heindl (see chapter three in ref. [41]). A very detailed description can also be found in ref. [31]. The experimental setup is realized in a "table-top" configuration and therefore very convenient to work with. In the following, a brief overview of the experimental setup is presented and the most important aspects are illustrated. In the present thesis great attention is paid to the improvements which have been introduced compared to the experimental setup described in ref. [31] and [41].

2.1 Excitation of Liquid Noble Gas Samples

The excitation method is based on low-energy electrons (12 keV) from a conventional cathode ray tube coupled into the liquid noble gas samples through a 300 nm thin SiO_2/Si_3N_4 ceramic membrane[1] [10]. The scintillation light exits the cell containing the liquefied noble gas through a MgF_2[2] window and is analyzed with a VUV monochromator with different detectors for different wavelength ranges. The cathode ray tube could also be used in a pulsed mode which enabled time-resolved studies at selected wavelengths. Fig. 2.1 shows a schematic overview of the experimental setup.

The scintillation cell is almost exclusively made of copper. Fig. 2.2 shows a cut through the scintillation cell adapted from a technical drawing. The liquid noble gas volume is $\sim 2\,\mathrm{cm}^3$. The distance between the ceramic entrance membrane and MgF_2 exit-window is 2.3 mm. This distance is enough to perform measurements in the gas phase under moderate pressures as well as in the liquid phase since the penetration depth of ~ 10 keV electrons is of the order of 1 mm in the gas phase and 1μm in the liquid phase, respectively. A more detailed discussion with GEANT4 simulations[70] of the mean path lengths will follow in the sections on the efficiency measurements (see sections 3.3 and 3.4).

[1] The energy loss of 12 keV electrons in the membrane has been measured under vacuum conditions on both sides of the membrane to be $\sim 15\,\%$ [69].

[2] Transmission in a wavelength region from $\sim 115 - 7500$ nm.

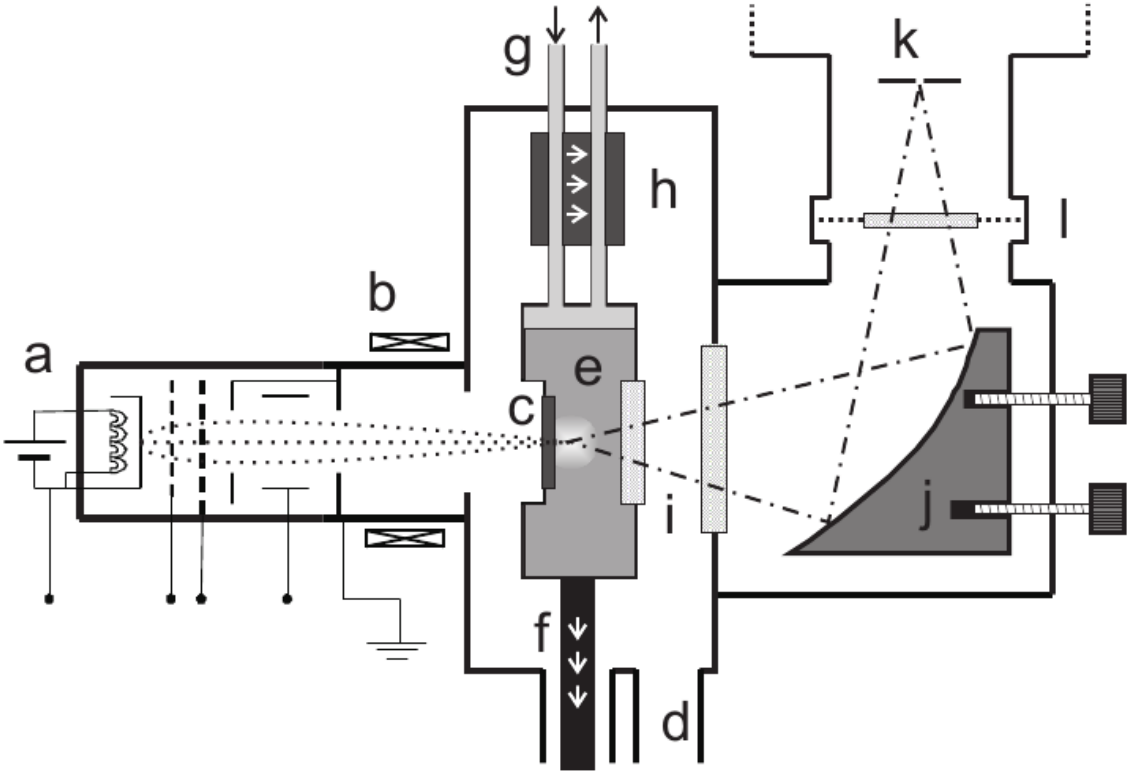

Figure 2.1: *A schematic overview of the experimental setup: (a) Cathode ray tube with heated cathode, extraction grid, a grid for beam pulsing and an electrostatic focussing grid. (b) Magnets for electromagnetic beam steering. (c) 300 nm thick ceramic entrance membrane which separates the vacuum of the cathode ray tube from the liquid noble gas volume. (d) The isolation volume and the volume of cathode ray tube have been evacuated by a turbomolecular pump. The liquid noble gas scintillation cell (e) was connected to a copper rod (f) attached to a liquid nitrogen dewar. The white arrows indicate the flow of heat. The gas in and outlet pipes (g) were thermally connected via a heat exchanger (h) to enable a continuous purification of the gas by evaporation, purification in the gas phase and recondensation into the copper cell. Two MgF_2 windows (i) enabled the propagation of scintillation light. An adjustable Al-MgF_2-coated elliptical mirror (j) focused the scintillation light on the entrance slit of the monochromator (k). An optical filter wheel (l) enabled to suppress different second diffraction orders mainly relevant for wavelengths longer than 200 nm. The figure is adapted from ref. [31].*

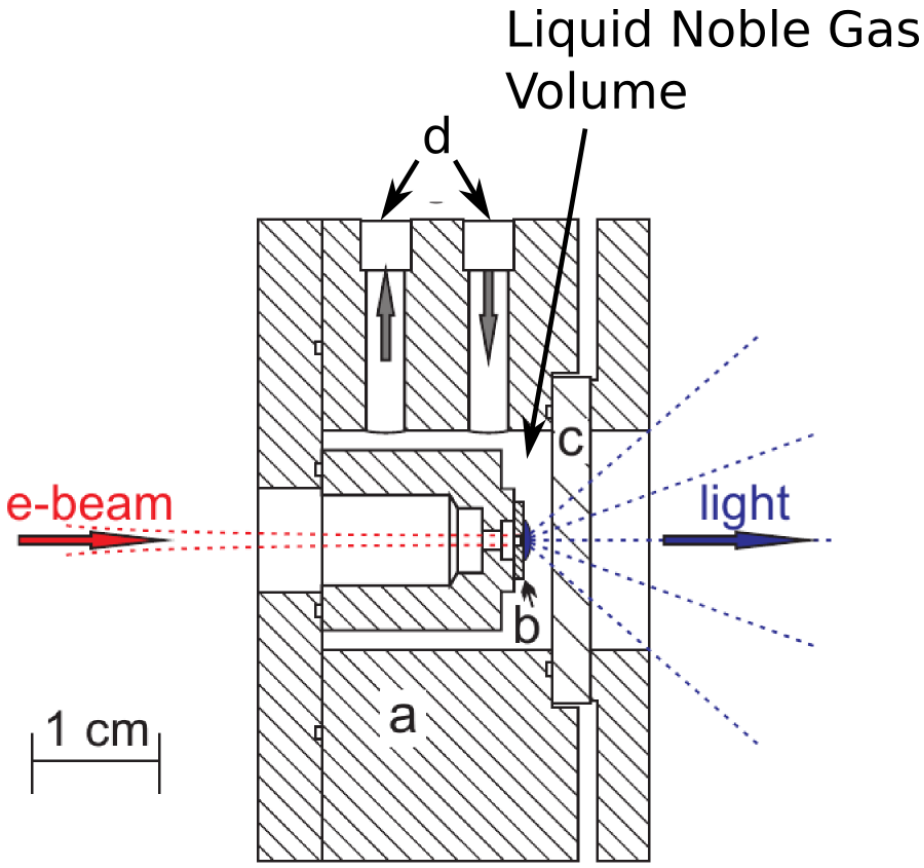

Figure 2.2: *A cut through the indium-sealed scintillation cell is shown. The cut goes through the optical axis. The main part (a) of the cell is made of copper. The electron beam in vacuum is coupled into the liquid noble gas samples through the 300 nm thin ceramic membrane (b) glued on the right end of a tubular workpiece manufactured from invar. The emitted scintillation light exits the cell through a MgF_2 window (c). On top of the drawing the gas in and outlet boreholes (d) are visible. The volume of the liquid noble-gas sample is $\sim 2\,cm^3$ and the distance between the point where the electrons enter the gas and the MgF_2 window is 2.3 mm. This figure is adapted from ref. [31].*

2.2 Gas Handling

The purity of the gases used in the scintillation experiments is a very important parameter in wavelength-resolved studies since impurity emissions are visible in the emission spectra already at very small concentrations. Impurities can influence the spectral emission as well as the temporal emission properties of the noble gases (see, e.g., liquid argon [31]). In the experiments described here the gas is kept in a closed, completely metal-sealed cycle and is continuously purified during the experiments using a metal-bellows compressor and a conventional noble gas purifier (SAES getters, Model: MONO TORR® PS4-MT3-R-2). From former experiments with liquid argon it is known that xenon is a critical impurity which is not removed by regular chemical purification [31, 33, 39, 40, 42, 44]. Therefore, an additional conically shaped copper vessel was designed and built which could be immersed into liquid nitrogen to an appropriate extent for a careful temperature controlled distillation process [53] to remove[3] xenon. Fig. 2.3 shows a schematic overview over the complete gas system and Fig. 2.4 a photograph of the distiller.

[3]The melting point of solid xenon is at 161 K (at 1000 mbar) which is higher than the boiling temperature of liquid argon (87 K) and liquid nitrogen (77 K).

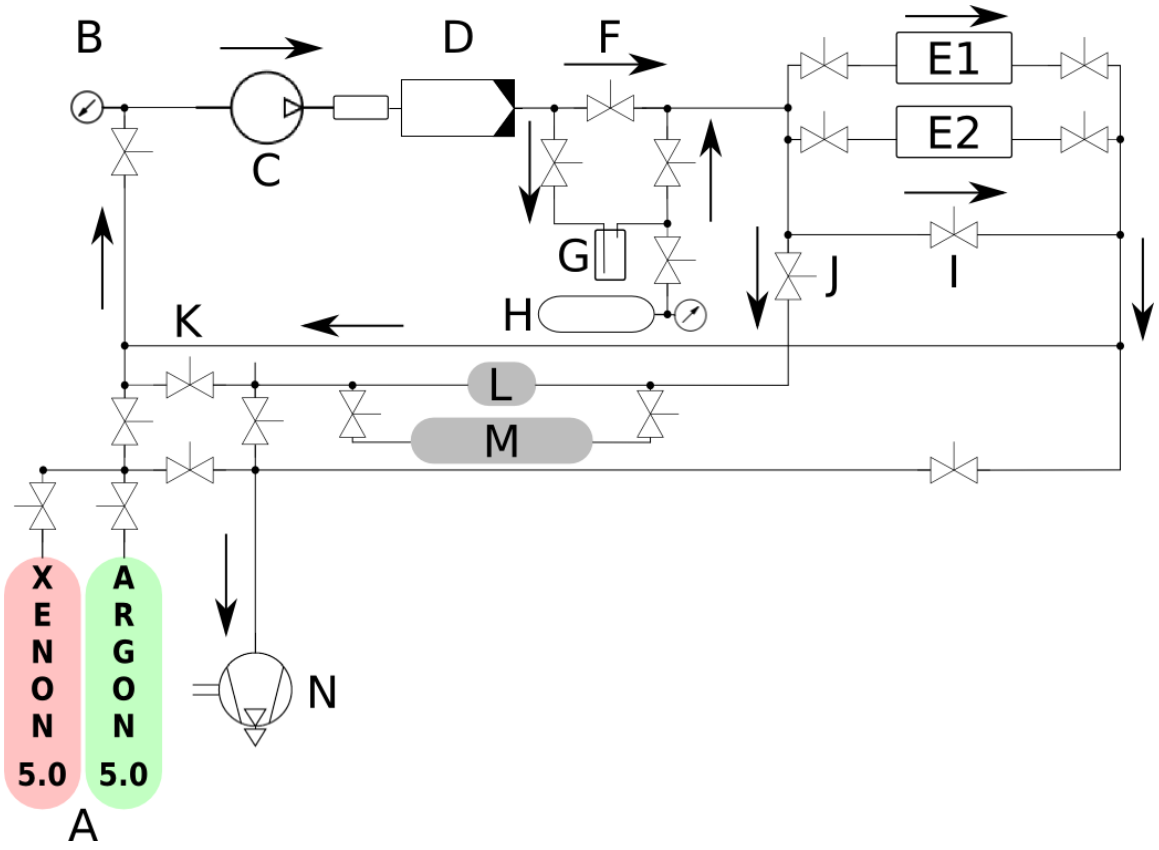

Figure 2.3: *A schematic overview of the gas system is presented. The gas (A, argon or argon-xenon mixtures) is filled into the system and the pressure could be measured with a precise capacitive manometer (B, MKS Baratron 390H 1000). During the measurements the gas is continuously circulated (indicated by the black arrows) by a metal-bellows compressor (C) through a gas purifier (D, SAES getters, Model: MONO TORR® PS4-MT3-R-2) and the experiments (E1, E2). E1 is the scintillation experiment and E2 is a transmission experiment which is described in section 4.1. A fractional distillation in a continuous flow mode could optionally be performed by closing the bypass valve (F). The conically shaped distiller (G) can be immersed into liquid nitrogen, thereby maintaining the distillation temperature by the depth of immersion. After the distillation the distiller is closed and heated up again and the distillated gas components are evaporated into the expansion volume (H). The flow of gas through the experiment was regulated by the bypass valves (I or J and K). Two gas reservoirs with different volumes (L: $\sim 3\,l$, M $\sim 23\,l$) were used to adjust the amount of gas for different liquid volumes. With a turbomolecular pump (N) the system could be evacuated. The drawing is adapted from ref. [53].*

Figure 2.4: *Left: The conically shaped distiller (G, in Fig. 2.3) is made of copper with a Pt-100 sensor glued to it for measuring the temperature at the bottom of the distiller. On the backside (not visible here) also a heating resistor is mounted which enabled a regulation of the temperature in a more precise way once the depth of immersion in liquid nitrogen was adjusted. Right: The distiller is immersed into a small dewar filled with liquid nitrogen. The gas is continuously circulated through the distiller from left to right which is indicated by the different lengths of water frozen to the gas pipes. The photograph is adapted from ref. [53].*

2.3 Wavelength-Resolved Light Detection

For the wavelength-resolved light detection from the vacuum ultraviolet to the infrared the same monochromator (McPherson 218) was used. The monochromator has a focal length of 30 cm in a criss-cross Czerny-Turner optical design with an aperture ratio of $\frac{1}{5}$. For the wavelength range from 115 nm to 850 nm a reflection grating with $1200\frac{\text{Lines}}{\text{mm}}$ with a blaze wavelength[4] of 150 nm was used (VUV grating, G1). According to the manufacturer, this leads to a dispersion[5] of $2.6\frac{\text{nm}}{\text{mm}}$ [71]. For the wavelength range from 500 to 3500 nm a reflection grating with $300\frac{\text{Lines}}{\text{mm}}$ with a blaze wavelength of 1000 nm was used (IR grating, G3) which leads to a dispersion of $10.4\frac{\text{nm}}{\text{mm}}$ [71].

To detect light in the wide wavelength range from the vacuum ultraviolet to the infrared, different detection principles involving different detectors are necessary. In this section the technique used in the vacuum ultraviolet is briefly outlined. A detailed description can be found in refs. [31] and [41]. The light detection in the infrared is a novel aspect which has been introduced in the experimental setup. Therefore, the infrared region is strongly emphasized.

2.3.1 Vacuum Ultraviolet to Visible

From the vacuum ultraviolet to the visible region a photomultiplier (ET Enterprises, D860B) with S20 cathode and MgF_2 entrance window was used. The sensitive wavelength region ranged from $\sim (110 - 850)$ nm. The measurements were performed in single photon counting mode with a typical dark count rate of 100 Hz and a maximum rate of 100 kHz which is well below pile-up conditions. The photomultiplier pulses were converted to digital pulses by a constant fraction discriminator. The digital pulses were counted for a certain user controlled integration time, and the number of counts was finally read out in correlation with the adjusted wavelength of the monochromator to obtain the emission spectra.

A pulsed electron beam was used for time-resolved measurements. The trigger signal from the power supply of the cathode ray tube which starts the electron beam was used as start signal. The first photomultiplier pulse from a detected photon was used as stop signal. The time difference between start and stop signal was converted to an analog voltage using a time-to-amplitude converter (Ortec 566). The output voltage was proportional to the difference between start and stop signal. The analog voltages were digitized by a 13 bit analog-to-digital converter (Ortec AD413A) and recorded in a histogram to obtain the time structure. The time-to-amplitude converter was calibrated using a precision pulse generator (Stanford Research Systems DG535).

[4] Wavelength region of maximum reflection.

[5] The resolution is calculated from the dispersion times the adjusted slit width of the monochromator.

Wavelength Calibration of the VUV Grating

The wavelength calibration of the setup with the VUV grating was carried out using the Lyman-alpha line of a deuterium arc lamp (Cathodeon Model V03) and the electron-beam induced scintillation of pure gaseous argon at atmospheric pressure and room temperature. Figs. 2.5 and 2.6 show the measured emission spectra. The discrete line radiation was used to calibrate the wavelength axis by comparing the measured line positions with the expected wavelength positions from NIST [50]. It turned out that in the vacuum ultraviolet wavelength region, the raw data have to be shifted by $\sim 0.53\,\mathrm{nm}$ to shorter wavelengths. This value increases to $\sim 0.65\,\mathrm{nm}$ towards longer wavelengths (see Fig. 2.6). Therefore, all the following spectra are corrected for these wavelength shifts. However, it has to be mentioned that in the vacuum ultraviolet wavelength region basically broad continuous emission structures are investigated (see, e.g., Fig. 1.5), thus, this correction only has a minor impact on the emission spectra presented.

Wavelength-dependent Responsivity in the VUV

One important aspect is the wavelength-dependent responsivity of the whole experimental setup from the generation of the scintillation light to its wavelength-resolved detection. To present spectra in the right relative intensity, the wavelength-dependent responsivity of the monochromator-detector system has to be known. This issue becomes especially severe in the vacuum ultraviolet region towards the short-wavelength cut-off where the responsivities of the cathodes of the photomultipliers as well as the transmission of the MgF_2 windows [72] decrease. Therefore, in all the raw-data spectra usually the short wavelength region is strongly suppressed and a relative correction has to be performed to obtain the right relative intensities proportional to the power of light emitted per unit wavelength.

However, it has to be emphasized that the issues described in this subsection do not influence the scintillation efficiency measurements presented in section 3.3. The scintillation-efficiency values in the vacuum ultraviolet have been obtained without applying any responsivity correction to the raw data. The present subsection is intended to present not only the responsivity of the experimental setup but rather in general the technical issues and the resulting systematic errors which have to be expected when vacuum ultraviolet radiation has to be recorded wavelength resolved with the right relative intensity.

From a former work [41] a calibrated electron-beam induced scintillation spectrum in a wavelength range from 115 to 250 nm of gaseous argon at 300 mbar was available. This spectrum has been obtained from a measurement in a calibrated[6] setup at identical conditions which was built to study the electron-beam induced emission of gaseous argon [14]. Since the responsivity measurement of the experimental setup

[6]The setup had been calibrated using a Cathodeon deuterium-lamp, traceable to: type V03, serial No. V0282, calibrated by PTB calibration mark PTB-065402. The uncertainties of the absolute flux of the calibrated lamp in different wavelength intervals were: 14 % from 116.0 to 120.4 nm, 36 % from 120.6 to 122.6 nm, 14 % from 122.8-170.0 nm and 7 % from 172.0 to 250.0 nm.

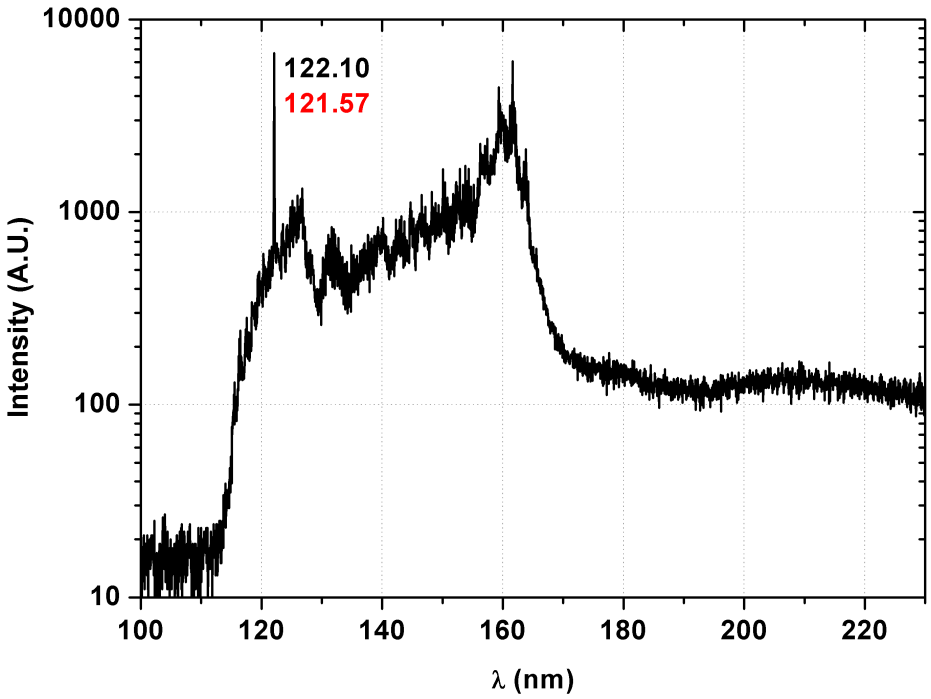

Figure 2.5: *A logarithmically scaled emission spectrum of a deuterium arc lamp (Cathodeon Model V03) with MgF_2 window is shown. The wavelength resolution was 0.03 nm and the step size 0.05 nm. The black number indicates the measured wavelength position of the of the Lyman-alpha line (in nm) and the red number is the expected value obtained by NIST [50]. A comparison between these numbers shows that the raw data have to be shifted $\sim$ 0.53 nm to the left to obtain the correct wavelength position. Note that below $\sim$ 117 nm the measured signal is only background since the MgF_2 window of the deuterium arc lamp begins to become opaque for lower wavelengths.*

was already $\sim$ 4 years old the measurement was repeated. The experimental setup was filled with 300 mbar gaseous argon at room temperature and a measurement in a wavelength interval from 115 - 230 nm was performed. The data were background corrected and divided by the calibrated argon spectrum to obtain the wavelength-dependent responsivity of the experimental setup. Fig. 2.7 shows the wavelength-dependent responsivity obtained from this measurement compared to the responsivity obtained by Heindl (see Fig. 3-10 in ref. [41]) four years ago.

The discrepancy between both measurements cannot be explained by the calibration errors of the deuterium lamp in different spectral regions. A first explanation could simply be an aging effect of the MgF_2 windows of the experimental setup since the measurements are taken at a time distance of four years. A second explanation could be an unresolved systematic error in the transfer of the measurements between

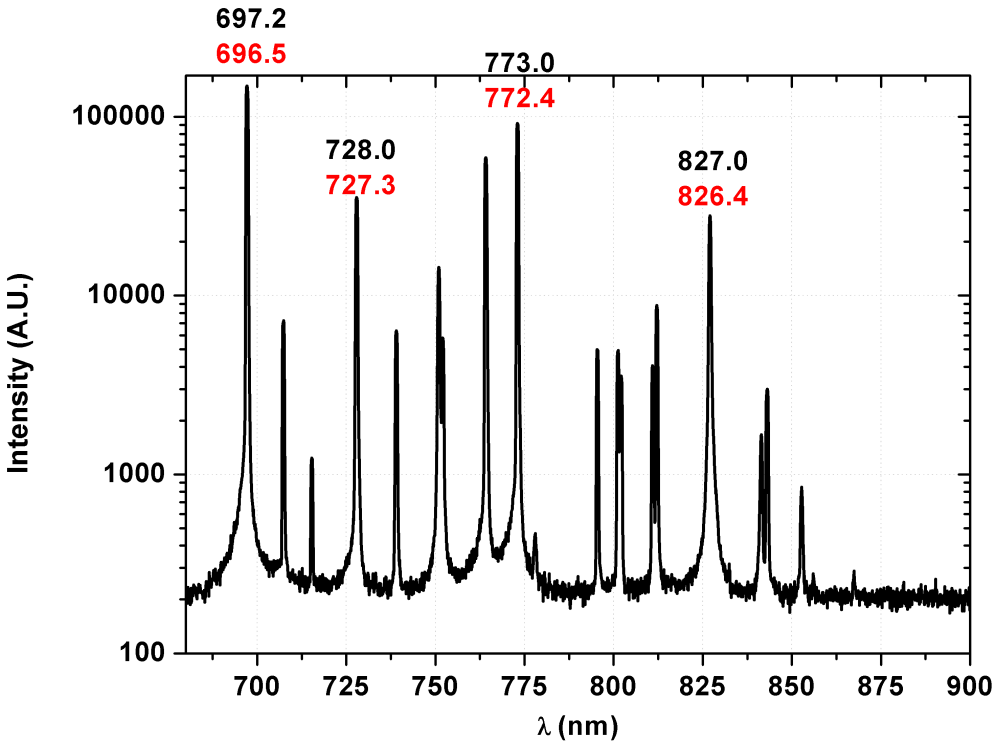

Figure 2.6: *A logarithmically scaled emission spectrum of the electron-beam (12 keV, 1.7 μA) induced scintillation of gaseous argon is shown. The gas was at room temperature and a pressure of 1045 mbar. The wavelength resolution was 0.3 nm and the step size 0.1 nm. The black numbers indicate the wavelength positions of the measured peaks (in nm) and the red numbers are the expected values obtained by NIST [50]. A comparison between these numbers shows that the raw data have to be shifted by* ~ 0.65 *nm to the left to obtain the correct wavelength position.*

two different experimental setups. However, it turned out that a more severe effect influences the obtained responsivity curve. The background correction of the raw data is a critical step. Fig. 2.8 shows the emission spectrum (raw data) of pure gaseous argon (T = 300 K, p = 300 mbar) under electron-beam excitation (12 keV, 1.5 μA). This raw data spectrum has been used to calculate the responsivity (black) curve shown in Fig. 2.7. In all the VUV spectra the background correction has been obtained by measuring spectra beginning at a wavelength of 100 nm. Since below 113 nm (cut-off wavelength of the MgF_2 windows [72]) no signal is expected, the average signal from 100 - 110 nm has been used as background value which was subtracted from the spectra before they were corrected with the responsivity. The red line in Fig. 2.8 denotes the background level obtained from calculating the average signal from 100 to 110 nm.

This background correction assumes a wavelength-independent background. The spectra obtained with the closed (dark) monochromator were perfectly flat. This

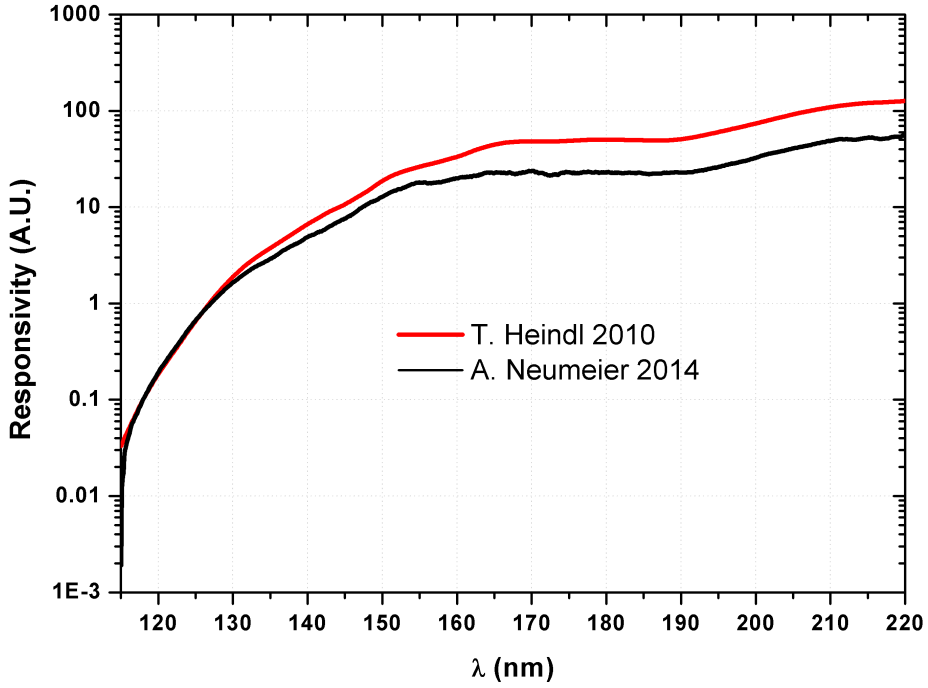

Figure 2.7: *The measured responsivities of the experimental setup from the short-wavelength cut-off at 115 nm to 220 nm are shown. The responsivities strongly decrease towards short wavelengths. The measurements show a similar spectral trend. However, the more recent measurement from 2014 (black line) shows a decreased relative responsivity beginning at 130 nm towards longer wavelengths compared to the measurement by Heindl in 2010 (red line, adapted from Fig. 3-10 in ref. [41]). The responsivities are scaled to one at 127 nm (scintillation wavelength of argon).*

aspect shows that the electronic noise is independent of the wavelength position of the monochromator and supports the assumption of a wavelength-independent background. However, stray light in the monochromator can not be assumed to be wavelength-independent. This issue can be disregarded if the light intensity in the spectra is high enough so that the background can be neglected compared to the signal. In wavelength regions where a low light intensity has been measured the impact of the background correction becomes more severe. Subtracting a higher background leads to a smaller signal and, hence, to a lower responsivity. However, especially in wavelength regions where a low signal is present in the raw data it is difficult to disentangle background and stray light from the real signal. Therefore, in these wavelength regions the background subtraction basically determines the responsivity curve. Stray light in general is difficult to handle since it is only present when the light source (which is analyzed) is turned on and absent when the light source is turned off. Stray light also depends on the amount of light entering the monochromator, i.e.,

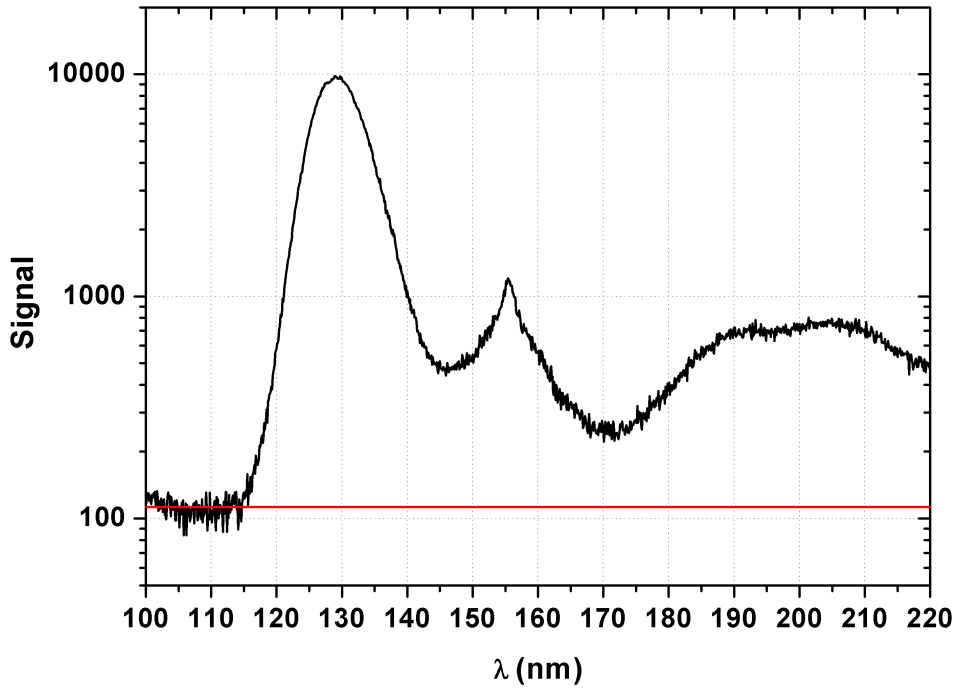

Figure 2.8: *The black curve shows a logarithmically scaled electron-beam (12 keV, 1.5μA) induced raw-data scintillation-spectrum of pure gaseous argon (T = 300 K, p = 300 mbar). The red horizontal line denotes the assumed background level which was calculated from the average signal between 100 and 110 nm. After background correction this spectrum was used to calculate the (black) wavelength-dependent responsivity curve in Fig. 2.7. The signal from 100 to 110 nm is not absolutely flat which indicates a contribution of stray light to the background level.*

on the slit width.

In section 3.3 wavelength-integrated VUV efficiency measurements[7] of the electron-beam induced scintillation of liquid argon-xenon mixtures in a wavelength region from 120 - 140 nm and from 155 - 190 nm will be presented. A comparison of the ratios of the measured integral efficiency values in these two wavelength regions with the ratios of the corresponding areas in the responsivity-corrected[8] emission spectra show that the wavelength region from 120 - 140 nm is overestimated by a factor of ~ 2 compared to the region from 155 - 190 nm. Therefore, when looking at the VUV spectra presented in chapter 3, one should keep this restriction in mind.

A further aspect which should be mentioned here is that the emission spectrum to obtain the wavelength-dependent responsivity has been measured when the scintilla-

[7]These measurements do not rely on any responsivity correction.

[8]Responsivity-corrected means that the raw-data spectra were background corrected and divided by the black responsivity curve in Fig. 2.7.

tion cell was filled with gaseous argon at a pressure of 300 mbar and room temperature. Using liquid noble gas samples increases the amount of transmitted scintillation light through the transition between liquid argon and the inner surface of the MgF_2 window (see c in Fig. 2.2). The increased refractive index of liquid argon compared to gaseous argon leads to a better adaption of the refractive indices at the transition between liquid argon and MgF_2 window (Fresnel formulas for normal incidence of light), and therefore, to a higher transmission. Since there is no wavelength-resolved data concerning the refractive index of liquid argon as well as xenon-doped liquid argon, no correction was applied to the data for this effect. However, the refractive index of pure liquid argon can be estimated by a density scaling from the gas phase into the liquid phase (in analogy to the strategy described in ref. [73]). Fig. 2.9 shows the wavelength-dependent refractive indices of pure liquid argon and cryogenic (80 K) MgF_2. The data for the wavelength-dependent refractive index of pure gaseous argon have been adapted from ref. [74] and the data for the wavelength-dependent refractive index of MgF_2 at cryogenic temperatures have been adapted from ref. [75]. Note that below 140 nm no measured values of the refractive index of gaseous argon are available (see ref. [74]), which leads to a situation where a density scaling from the gas into the liquid phase is performed without any measurements in the gas phase.

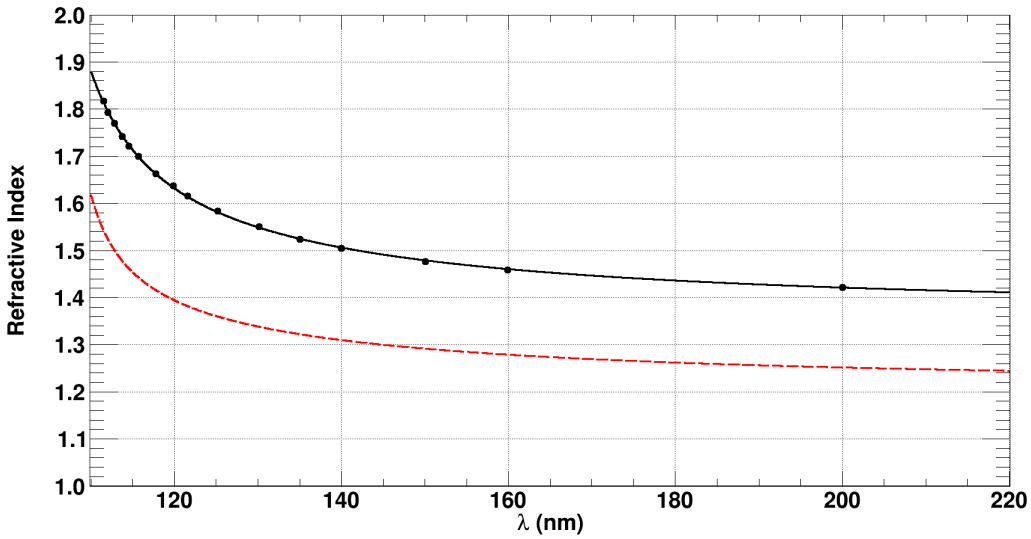

Figure 2.9: *The wavelength-dependent refractive index of MgF_2 at 80 K (black curve) adapted from ref. [75] is shown. The black dots show measurements and the black line shows a model fit [75] to the data. The red dashed curve shows the wavelength-dependent refractive index of pure liquid argon obtained from a density scaling of the data in the gas phase [74] analogous to the strategy presented in ref. [73].*

Since the responsivity calibration of the experimental setup has been obtained with the inner cell filled with gaseous argon it is interesting to calculate the relative variation of the transmission through the inner MgF_2 surface (see c in Fig. 2.2) when

the inner cell is filled with liquid argon. The relative variation is calculated according to eq. 2.1 and the result is shown wavelength-resolved in Fig. 2.10.

$$\mathrm{T} = \frac{1 - \left(\frac{\mathrm{n_{LAr}} - \mathrm{n_{MgF_2}}}{\mathrm{n_{LAr}} + \mathrm{n_{MgF_2}}}\right)^2}{1 - \left(\frac{\mathrm{n_{GAr}} - \mathrm{n_{MgF_2}}}{\mathrm{n_{GAr}} + \mathrm{n_{MgF_2}}}\right)^2} \tag{2.1}$$

$\mathbf{T} = \mathbf{T}(\lambda)$ Wavelength-dependent variation of the transmission through the inner MgF_2 surface when the cell is filled with liquid instead of gaseous argon

$\mathbf{n_{LAr}} = \mathbf{n_{LAr}}(\lambda)$ Wavelength-dependent refractive index of liquid argon

$\mathbf{n_{MgF_2}} = \mathbf{n_{MgF_2}}(\lambda)$ Wavelength-dependent refractive index of magnesiumfluoride

$\mathbf{n_{GAr}} = \mathbf{n_{GAr}}(\lambda)$ Wavelength-dependent refractive index of gaseous argon

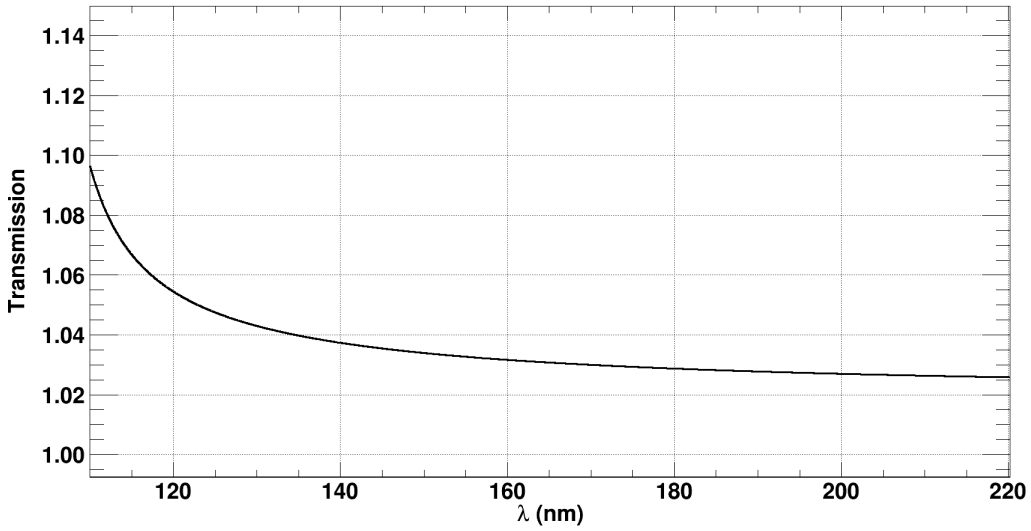

Figure 2.10: *The wavelength-dependent relative variation of the transmission through the inner surface of the MgF_2 window of the inner cell (see c in Fig. 2.2) is shown. The curve shows wavelength-resolved the relative variation of the transmission when the inner cell is filled with liquid instead of gaseous argon. The variation was calculated using eq. 2.1 and the data in Fig. 2.9. The data for gaseous argon have been adapted from ref. [74].*

A wavelength-independent (flat) variation of the transmission would not influence the relative intensities shown in the responsivity-corrected emission spectra when the inner cell is filled with liquid argon. However, based on the calculated curve in Fig. 2.10 a maximum variation of 9.5 % (at 110 nm) and a minimum variation of 2.5 % (at 220 nm) compared to the gas phase can be deduced. Consequently, a wavelength-dependent systematic error of maximal 7 % is introduced in emission spectra which

are corrected with the responsivity function (black curve in Fig. 2.7) between 110 and 220 nm. Note, however, that in any realistic experiment using liquid noble gases as scintillator medium, similar issues can be expected since the scintillation light has to be coupled out of the liquid into the detector through some transparent window material.

In the present setup the scintillation light has to propagate a distance of 2.3 mm in the liquid noble gas samples before it exits the scintillation cell through the MgF_2 window. In the case of pure liquid argon this distance is much smaller than the attenuation length (lower limit: $\sim$ 1.1 m [53]) and a modification of the emission spectrum due to attenuation effects can therefore be neglected[9].

A precisely calibrated setup could be obtained by removing the cathode-ray tube (a in Fig. 2.1) as well as the entrance membrane (c in Fig. 2.1) and replacing it by a calibrated light source (e.g. a deuterium lamp). However, there is still one problem which is unsolved: The elliptical mirror (j in Fig. 2.1) focuses only one certain area of the discharge within the deuterium lamp into the monochromator which leads to a different emission spectrum compared to the calibrated spectrum measured by, e.g., the PTB (Physikalisch-Technische Bundesanstalt). In addition, wavelength-resolved data of the refractive index of all the liquid noble gas samples measured in the present thesis would be needed to correct the spectra for the adaption of the refractive index as explained above.

In terms of particle detector development these responsivity and refractive index issues described above are of minor importance since the detectors usually measure the light emissions in a wavelength-integrated way. Consequently, the important results in the present thesis are the wavelength-integrated scintillation efficiencies and not the (absolutely exact) relative intensities in the emission spectra. In that sense all the VUV spectra presented from now on are corrected only with the responsivity curve measured by myself (black curve in Fig. 2.7) since this is the most exact responsivity measurement available at the time being.

Reproducibility Study in the VUV

A further aspect has been discovered in wavelength-resolved transmission measurements of liquid noble gas samples in the vacuum ultraviolet wavelength region which is termed "fogging" in refs. [33, 53] and briefly explained in the following. The cold scintillation cell (e in Fig. 2.1) containing the liquid acts as a cold trap for rest gas components in the outer insulation vacuum (pressure: $\sim 3 \cdot 10^{-7}$ mbar). The outer surface of the cryogenic MgF_2 exit window (c in Fig. 2.2) could be coated with rest gas components which alter wavelength-dependent its transmission in analogy to the observation in refs. [33, 53]. There, the impact on the transmission of the cryogenic MgF_2 windows is severe, in particular, for wavelengths shorter than 160 nm (see for camparison, e.g., Fig. 15 in ref. [53] or Fig. 4.4 in the present thesis). If a coating of the

[9]This is certainly true for pure liquid argon. However, absorption features of xenon in xenon-doped liquid argon can be identified in the emission spectra as will be presented in section 3.2 when emission and transmission spectra are compared (see Fig. 3.3).

cryogenic MgF_2 window with rest gas components would be a problem in the present setup, a systematically decreasing emission with time being cold should be observed. Therefore, a measurement campaign was performed to study the reproducibility of the measurements in the vacuum ultraviolet region with the cold scintillation cell. The gas system was filled with 1100 mbar pure gaseous argon (distillated[10] and purified) and the scintillation cell was cooled down to a temperature of ~ 95 K to keep the argon in the cold gas phase. After the cooling-down which took approximately 45 minutes the first electron-beam (12 keV, 3.0μA) induced emission spectrum (reference spectrum) was recorded. After that further emission spectra with identical settings were recorded in a time distance of 45 and 30 minutes, respectively, and normalized to the reference spectrum. Fig. 2.11 shows the result of the measurement campaign. The first important result is that a "fogging" effect is not an issue in the present experimental setup since wavelengths below 140 nm were reproduced perfectly for which the largest impact of the "fogging" effect could be expected. However, a growing xenon emission at 147 nm [50] peak wavelength can clearly be seen which has also been identified as an issue in former measurements [31, 33, 39, 40, 42, 44]. This is a hint that the cold scintillation cell acts as a cold trap which is continuously accumulating xenon from the gas system. For wavelengths longer than 160 nm the signal is $\sim 10\,\%$ increased after 3 h cooling time. However, it has to be mentioned that the signal at longer wavelengths ($\lambda > 160$ nm) in the corresponding emission spectra (see, e.g., the red curve in Fig. 1.5) is strongly decreased compared to shorter wavelengths which explains the increased noise in Fig. 2.11 for wavelengths longer than 160 nm. A 10 % variation can be neglected compared to the errors which can be expected from the responsivity correction (see, e.g., Fig. 2.7 and text). For comparison, the scanning time for the high-resolution measurements in the liquid phase (presented below) was typically 1 h and the scans were started ~ 1 h after filling the dewar with liquid nitrogen.

So far two explanations can be specified for the strongly reduced "fogging" effect in the present setup compared to the transmission measurements in refs. [33, 53] and Fig. 4.4: Firstly, the number of MgF_2 surfaces in the optical path which can be coated is different in the two setups. In the transmission measurements presented in refs. [33, 53] and Fig. 4.4 two cold MgF_2 surfaces instead of one in the present setup can be coated with rest gas components from the insulation volume. And secondly, in the present setup, the pressure of the outer insulation vacuum was lower by a factor of ~ 2 compared to the setup used in refs. [33, 53].

2.3.2 Visible to Infrared

To enlarge the sensitive region of the experimental setup from the vacuum ultraviolet to wavelengths longer than 850 nm different detection concepts were used which are explained in the following. From the visible to the infrared wavelength region, two different detectors were attached to the monochromator: A thermoelectrically cooled

[10] The argon gas was distillated before the scintillation cell was cooled down. During the measurements the distiller was bypassed.

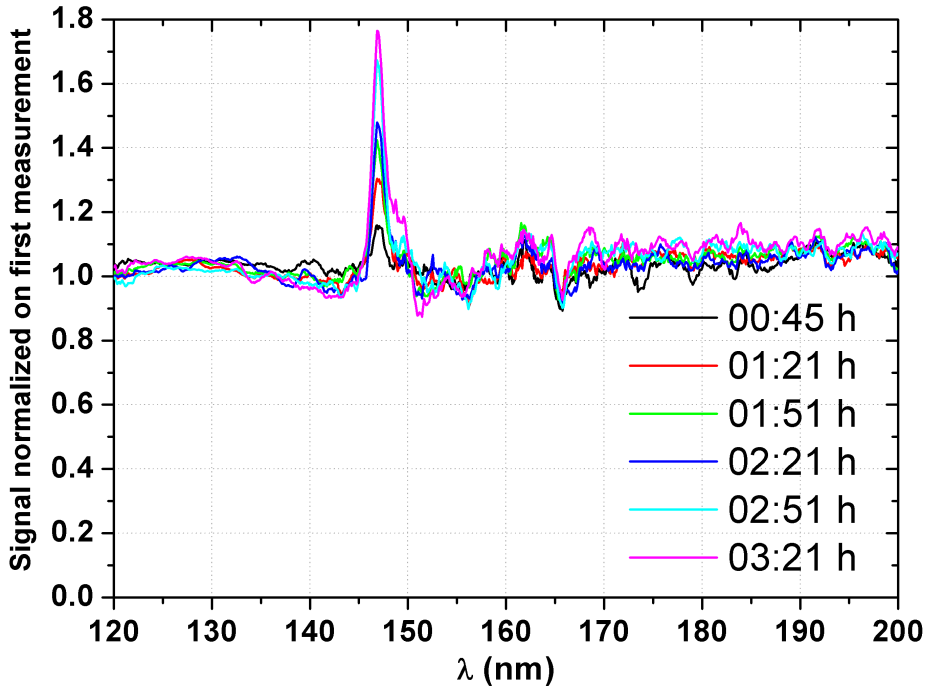

Figure 2.11: *The relative changes of electron-beam (12 keV, 3.0μA) induced emission spectra of cold (∼ 95 K) gaseous argon at several times after the first measurement are shown. The first spectrum (reference spectrum) was recorded when the scintillation cell reached a temperature of 95 K (45 minutes after the dewar was filled with liquid nitrogen). The different colors indicate measurement times relative to the reference spectrum. The short wavelength region is not affected by the "fogging" effect where the strongest impact would be expected [33, 53]. An accumulation of xenon in the cold cell can be observed due to the growing xenon resonce emission at 147 nm [50] peak wavelength.*

indium arsenide (InAs) infrared photodiode (Teledyne Judson, Model: J12TE3-66D-R01M-AST) and a near-infrared photomultiplier (Hamamatsu NIR-PMT Module H10330B-45 SEL). At first, the setup with the InAs infrared photodiode which is sensitive from 500 to 3500 nm is described:

InAs Infrared Photodiode

The signal of the InAs infrared photodiode was amplified with a transimpedance pre-amplifier (Teledyne Judson, Model: PA-6-60) and the signal to noise ratio was considerably improved by using a lock-in configuration.

Fig. 2.12 shows a photograph of the InAs infrared photodiode and Fig. 2.13 displays the responsivity curve provided by the manufacturer. In the experiments, the

temperature of the InAs photodiode was measured with a thermistor and adjusted with a microcontroller-based circuit to a constant value of -57 °C. The signal amplification and the readout chain of the InAs infrared photodiode is illustrated schematically in Fig. 2.14. The photocurrent of the InAs photodiode is converted to a voltage by a transimpedance pre-amplifier. The pre-amplifier gain is adjusted via the feedback resistor (R_F in Fig. 2.14) to a value of $1.01 \cdot 10^6 \frac{V}{A}$. At a frequency of 60 kHz the gain drops by -3 dB (i.e., a factor of $\frac{1}{\sqrt{2}}$ in amplitude) towards higher frequencies. For further lock-in detection, the scintillation light was chopped with a frequency of $\sim$ 110 Hz which is well below the bandwidth limit. The lock-in amplifier narrows the bandwidth of the signal to the chopping frequency and, therefore, improves the signal to noise ratio considerably. The output voltage of the lock-in amplifier is proportional to the intensity of the scintillation light and recorded in correlation with the wavelength position of the monochromator to obtain the scintillation spectra.

In all the experiments with the InAs photodiode, the monochromator was vented with air since the scintillation light had to be chopped with a regular chopper wheel in air to enable a lock-in amplification. Furthermore, the volume in front of the InAs photodiode could not be evacuated since this was neither tested nor recommended by the manufacturer. Influence from second or higher diffraction orders in the spectra could be excluded since the detector is sensitive beginning at 500 nm, i.e., it is "blind" in the vacuum ultraviolet spectral region where intense scintillation-light emission can be expected. The vacuum-tight light path was opened and the filter wheel (l in Fig. 2.1) was replaced by a chopper wheel which interrupted the scintillation light with a frequency of $\sim$ 110 Hz.

To obtain spectra in the right relative intensity all the spectra presented below are corrected with the reponsivity curve of the InAs infrared photodiode provided by the manufacturer (see Fig. 2.13). This is the only wavelength-dependent relative correction in the visible and infrared region since all the materials in the optical path (MgF_2 windows [76], Al-MgF_2-coated elliptical mirror[11] [77], reflection grating[12] and mirrors in the monochromator [77], sapphire window [79] of the InAs infrared photodiode) show a flat wavelength-dependent reflectivity and transmission in the wavelength region from 500 - 3500 nm.

Furthermore, an additional measurement with a calibrated tungsten strip lamp (OSRAM Wi 17/G, Nr.: 3261) positioned in the focal point of the elliptical mirror j (in Fig. 2.1)) showed that the wavelength-dependent responsivity of the mirror-monochromator system is flat from 500 to 1600 nm. A correction of the raw data with the responsivities of the detectors (InAs photodiode and near-infrared photomultiplier, see below) alone and the responsivity curves determined with the calibrated tungsten strip lamp resulted in the same emission spectra. However, it has to be mentioned that above 1600 nm, absorption bands were discovered which could not be

[11] From 500 to 2000 nm the reflectivity varies on a 10 % level which can be neglected compared to the variation of the detector responsivity in that wavelength region.

[12] Note that the blaze wavelength (λ_B) of the grating is 1 μm. A convenient description of the useful range of a reflection grating is the ($\frac{2}{3} - \frac{3}{2}$) - rule of thumb [78]. This means that the useful range of a grating is $\frac{2}{3} \cdot \lambda_B$ - $\frac{3}{2} \cdot \lambda_B$. It is not unusual to operate the grating out of that range. However, a higher variation of the wavelength-dependent reflectivity can be expected.

assigned unambiguously to a coating with absorbing material on the glass of the calibrated tungsten strip lamp or a real effect of the mirror-monchromator system. This has to be checked independently when continuous emission spectra at wavelengths longer than 1600 nm have to be measured using the present setup. Here, it is no problem since the emission spectrum of xenon-doped liquid argon (see Fig. 1.8, upper panel) does not extend to wavelengths longer than 1600 nm.

The sensitivity of the well adjusted setup was so high that even the thermal infrared emission of the glowing filament of the cathode ray tube could be detected (see Fig. 2.15). This is remarkable since the filament (a in Fig. 2.1) is completely out of focus of the elliptical mirror (j in Fig. 2.1) focusing the middle position of the entrance membrane (c in Fig. 2.1) into the monochromator entrance slit (k in Fig. 2.1). Therefore, all the infrared emission spectra presented below were corrected for this background radiation in the following way: In each measurement, the voltage and the current of the filament were documented. After the measurement of the scintillation of the liquid noble gas samples the high voltage (i.e., the electron beam) was turned off and the voltage and the current of the filament were adjusted to the values as in the measurement before. A background spectrum was recorded with the same settings but solely with the glowing filament as thermal radiation source. Fig. 2.15 shows (as an example) the thermal emission of the filament with a heating voltage of 6.8 V and a current of 232 mA. This emission spectrum can basically be understood as a black-body spectrum[13] convoluted with the emissivity of the material of the filament (barium oxide) and the transmission through the 300 nm thin SiO_2/Si_3N_4 ceramic entrance membrane. It was also checked that the ceramic entrance membrane itself does not scintillate in the infrared.

Near-infrared Photomultiplier

The second detector which was attached to the monochromator for infrared measurements was a near-infrared photomultiplier (Hamamatsu NIR-PMT Module H10330B-45 SEL). Fig. 2.16 shows the NIR-PMT module and the controller unit and Fig. 2.17 exhibits the wavelength-dependent responsivity (quantum efficiency and radiant sensitivity) of the photocathode measured by the manufacturer. The InP/InGaAsP photocathode is thermoelectrically cooled to -60 °C and sensitive from $\sim (900 - 1400)$ nm with an effective area of 1.6 mm in diameter. To improve the light collection without raising the area of the photocathode and consequently the dark count rate, the NIR-PMT is equipped with a BK7 anti-reflective coated condenser lens (diameter: 20 mm, focal length: 25.7 mm) which focuses incoming parallel light onto the photocathode. The NIR-PMT was mounted in front of the monochromator exit slit with an additional quartz[14] lens (anti-reflective coated) matched to the aperture ratio ($\frac{1}{5}$) of the monochromator to make the divergent light parallel before it is focused onto the photocathode of the NIR-PMT by the condenser lens. In the measurements pre-

[13] A simple estimation based on Wien's displacement law and the peak of the emission at $\sim$ 1700 nm leads to a temperature of the filament of $\sim$ 1700 K which is a reasonable value.

[14] Quartz shows a flat (wavelength independent) transmission within the wavelength range of the NIR-PMT. [81]

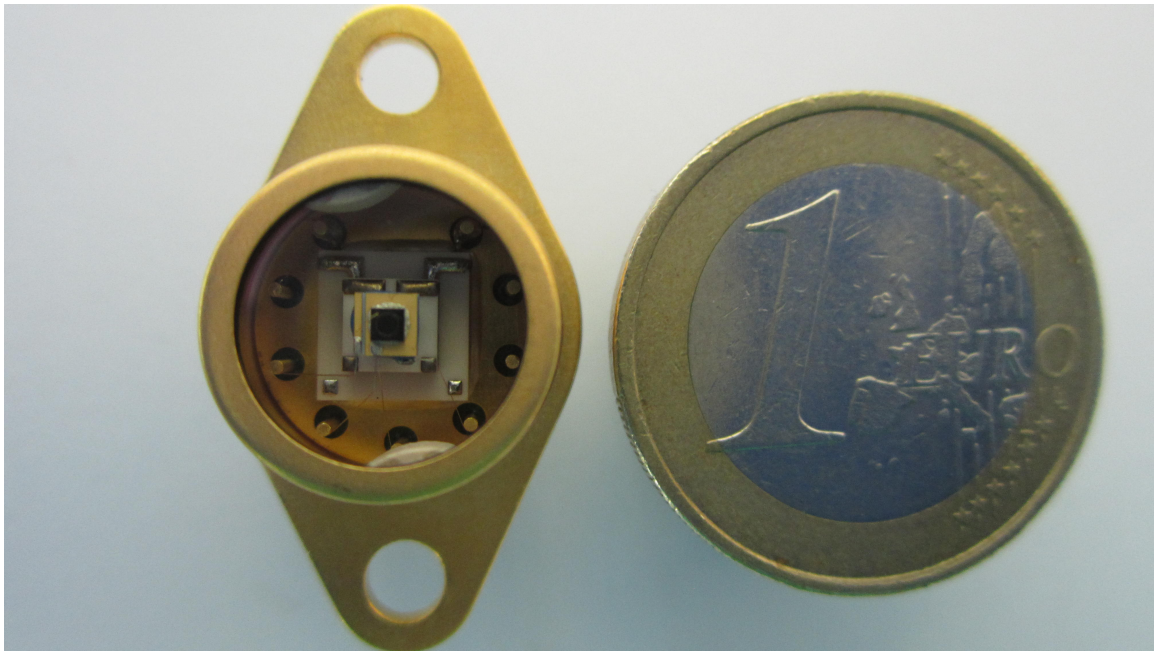

Figure 2.12: *A photograph of the thermoelectrically cooled InAs infrared photodiode (Teledyne Judson Technologies - J12TE3-66D-R01M-AST) is shown. The InAs photodiode (black square) has a circular active area with a diameter of 1 mm. For thermal noise reduction the InAs diode is mounted on a three stage Peltier element (white squares) for thermoelectric cooling down to -60 ℃. The window material is anti-reflective coated sapphire. A thermistor was incorporated in the housing for measuring the temperature of the diode. Right: A 1 Euro coin is shown for estimating the size.*

sented below, the supply voltage was adjusted to a value of -700 V which leads to a gain of $\sim 1 \cdot 10^6$. The high dynamic range of the photomultiplier compared to the InAs photodiode allows to record wavelength-resolved emission spectra with a high resolution and a high dynamic range. The wavelength resolution which was typically obtained in the measurements with the near-infared photomultiplier was 0.5 nm and with the InAs photodiode typically 5 nm. Due to the possibility to use the photomultiplier in single-photon counting mode, time resolved spectra could be obtained using the same standard time-to-amplitude conversion technology as described above with the photomultiplier used for the vacuum ultraviolet region. The time resolution was determined by the range of the time-to-amplitude converter and the following 13 bit analog-to-digital converter (Ortec AD413A) and was typically of the order of ns. For comparison the pre-amplifier of the InAs photodiode has a bandwidth of 60 kHz which leads to a time resolution of the order of 17μs when the gain already drops by a factor of $\frac{1}{\sqrt{2}}$.

The high wavelength resolution obtained with the NIR-PMT also allowed to check for a wavelength offset of the infrared grating (G3) by measuring the emission of gaseous argon doped with 1 ‰ xenon. In analogy to the procedure described above

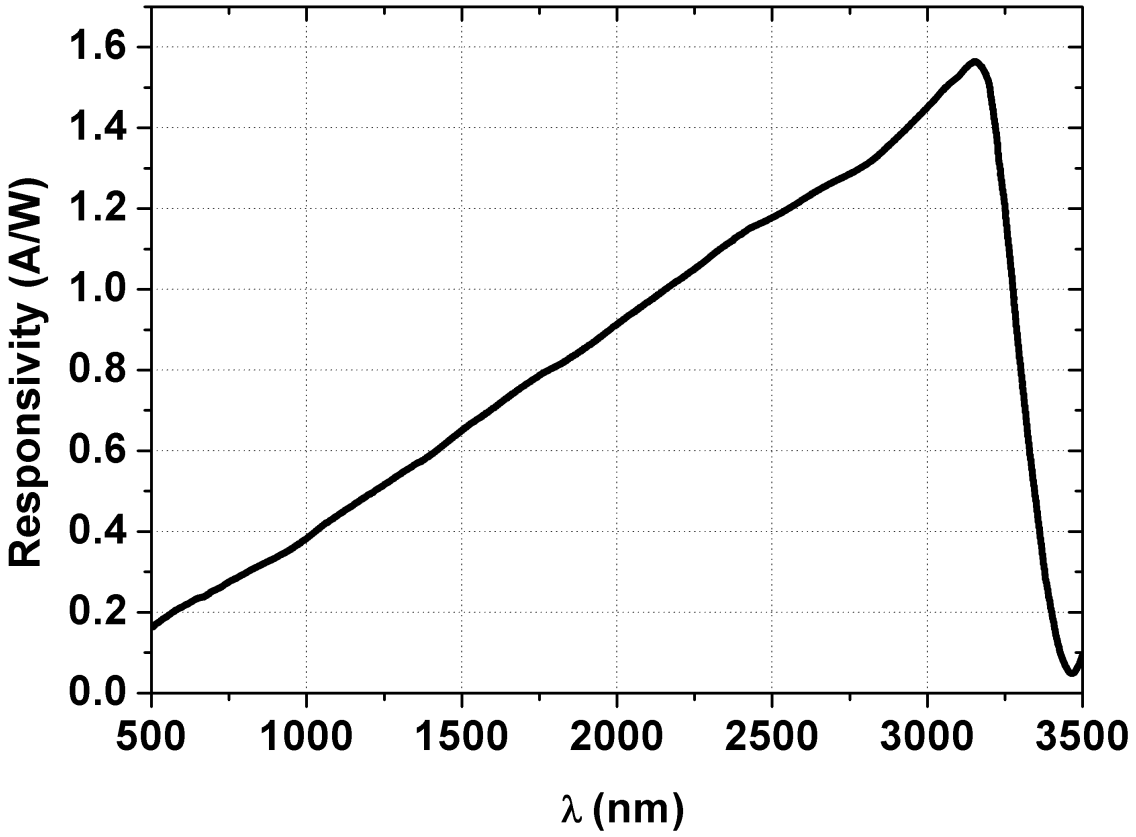

Figure 2.13: *The responsivity curve of the InAs infrared photodiode from 500 to 3500 nm provided by the manufacturer is shown. The responsivity increases almost linearily from 500 to 3150 nm, peaks at 3150 nm with* $1.54\frac{A}{W}$ *before it decreases very steeply.*

(with the VUV grating, G1) discrete line radiation was used to calibrate the wavelength axis by comparing the measured positions with expected wavelength positions of NIST [50]. Fig. 2.18 shows the electron-beam induced scintillation of gaseous argon doped with 1 ‰ xenon. A comparison of the wavelength positions of the emission lines with data from NIST for xenon transitions shows that the raw data have to be shifted by ~ 0.5 nm to shorter wavelengths. This correction is only applied to spectra recorded with the NIR-PMT. The wavelength resolution that could be obtained with the InAs infrared photodiode was 5 nm. Therefore, a correction of ~ 0.5 nm in wavelength position is not reasonable with a resolution which is an order of magnitude lower than the correction.

In all the spectra measured with the NIR-PMT, the background correction was obtained by measuring the count rates at wavelengths apart from the sensitive region of the photocathode and using this average signal as a background level. In all the spectra presented below the background is subtracted and a relative correction accounting for the responsivity (see Fig. 2.17) is also applied to the data. The amount of thermal radiation from the filament (see Fig. 2.15) could be neglected since the

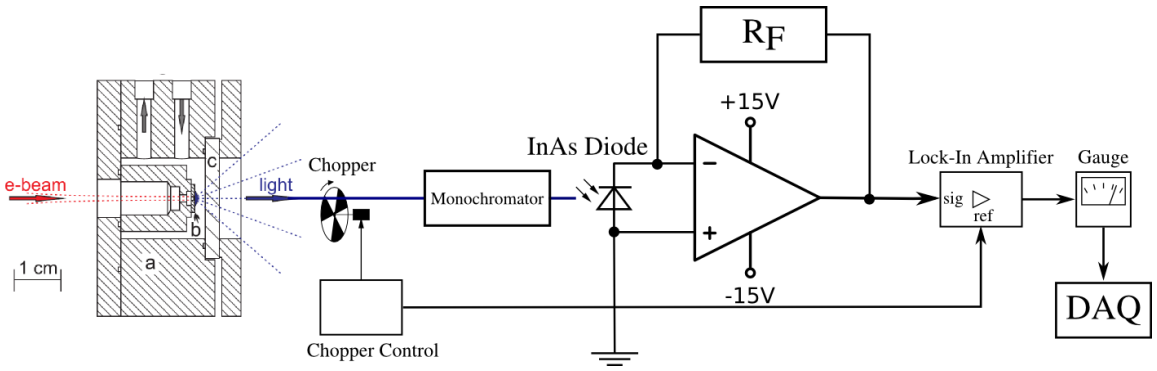

Figure 2.14: *The readout chain of the InAs infrared photodiode is illustrated schematically. From left to right: The electron beam excites the liquid noble gas samples and the scintillation light exits the cell through the MgF_2 window. A rotating chopper wheel on the optical axis periodically interrupts the scintillation light with a frequency of $\sim 110\,Hz$. The scintillation light is spectrally resolved in the monochromator and detected by the InAs photodiode. The photocurrent of the InAs photodiode is converted into a voltage by the transimpedance pre-amplifier (Teledyne Judson, Model: PA-6-60). The pre-amplifier creates a virtual ground at the inverting input (-) via the feedback resistor R_F. The value of the feedback resistor determines gain and bandwidth ($1.01 \cdot 10^6 \frac{V}{A}$ and $60\,kHz$). The square-wave voltage signal is coupled into a lock-in amplifier and integrated in correlation with the chopper signal on an RC element with adjustable integration time. Due to the narrowing of the bandwidth, the noise is decreased and, thereby, the signal to noise ratio is increased. The output signal of the lock-in amplifier is a voltage proportional to the scintillation light intensity which is finally recorded (DAQ, data acquistion) in correlation with the wavelength position of the monochromator to obtain the emission spectra.*

sensitive wavelength region of the NIR-PMT only extends up to $\sim 1350\,nm$. If thermal background would be an issue it should be visible as increasing signal towards the long wavelength end in Fig. 2.18 which is not the case.

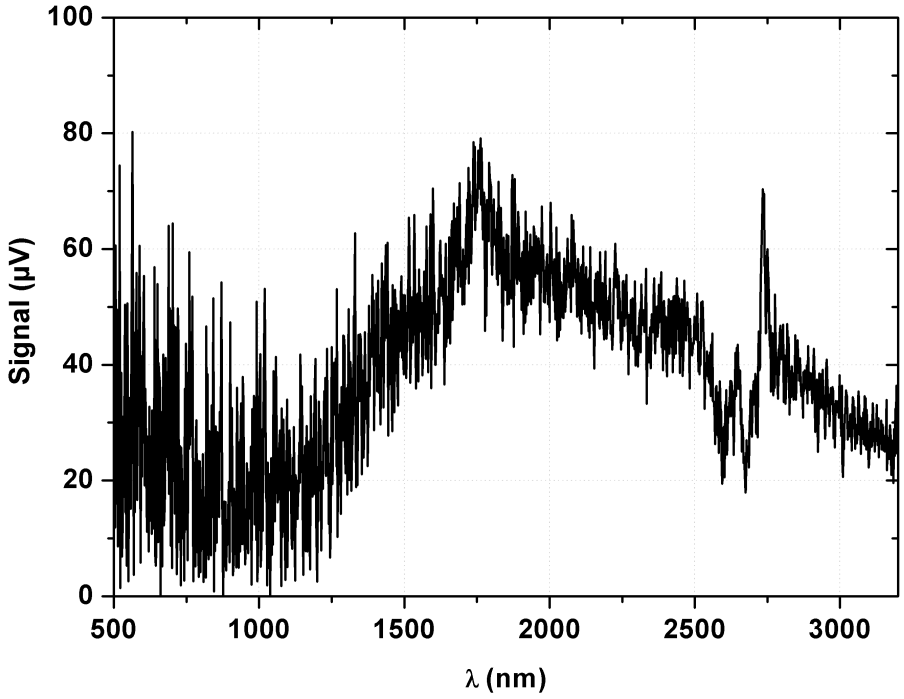

Figure 2.15: *Thermal emission spectrum of the glowing barium oxide filament of the cathode ray tube. The black body spectrum is convoluted with the emissivity of barium oxide and the transmission through the ceramic entrance membrane. The structure between 2500 and 2800 nm can be attributed to absorption due to water and carbon dioxide in the laboratory atmosphere [80].*

Figure 2.16: *A photograph of the near-infrared photomultiplier (NIR-PMT, left) and the controller unit (right). On top of the NIR-PMT a ventilator can be seen which dissipates the heat produced by the Peltier elements which cool the photocathode. On the front side the BK7 (anti-reflective coated) condenser lens can be seen which focuses incoming parallel light onto the photocathode. The controller unit regulates the temperature of the Peltier elements, the power supply, and the high voltage of the NIR-PMT.*

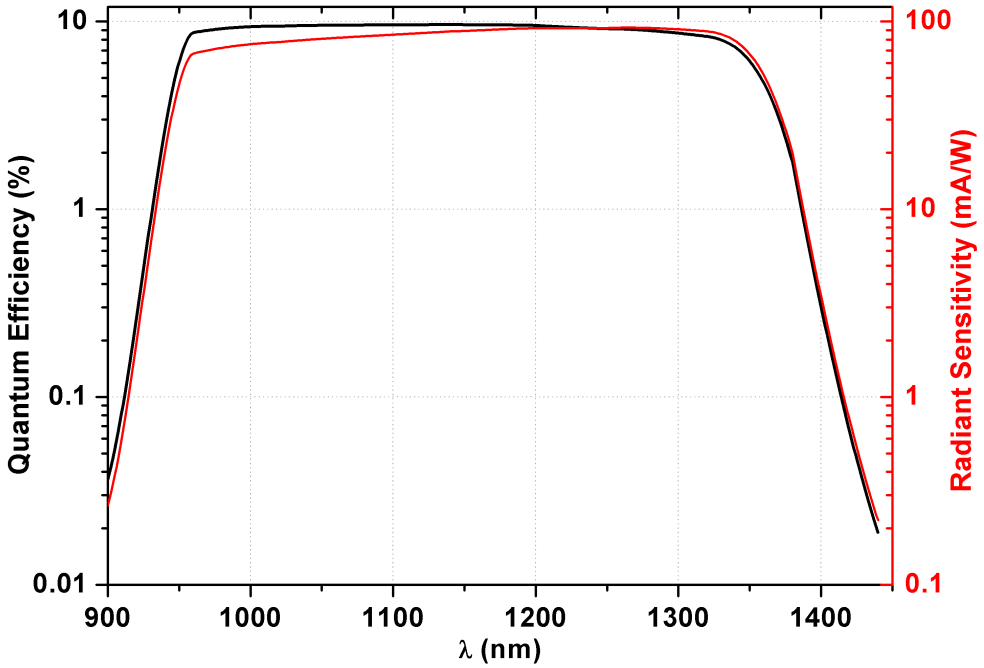

Figure 2.17: *The quantum efficiency (black, left ordinate) and the radiant sensitivity (red, right ordinate) versus wavelength of the NIR-PMT is shown. The data are provided by the manufacturer and were measured approximately 4 months prior to the measurements presented here. The radiant sensitivity curve is used for a relative correction of the raw data. Due to the flat (950 - 1350 nm) response curve the correction has a minor effect on the relative intensities in the spectra presented.*

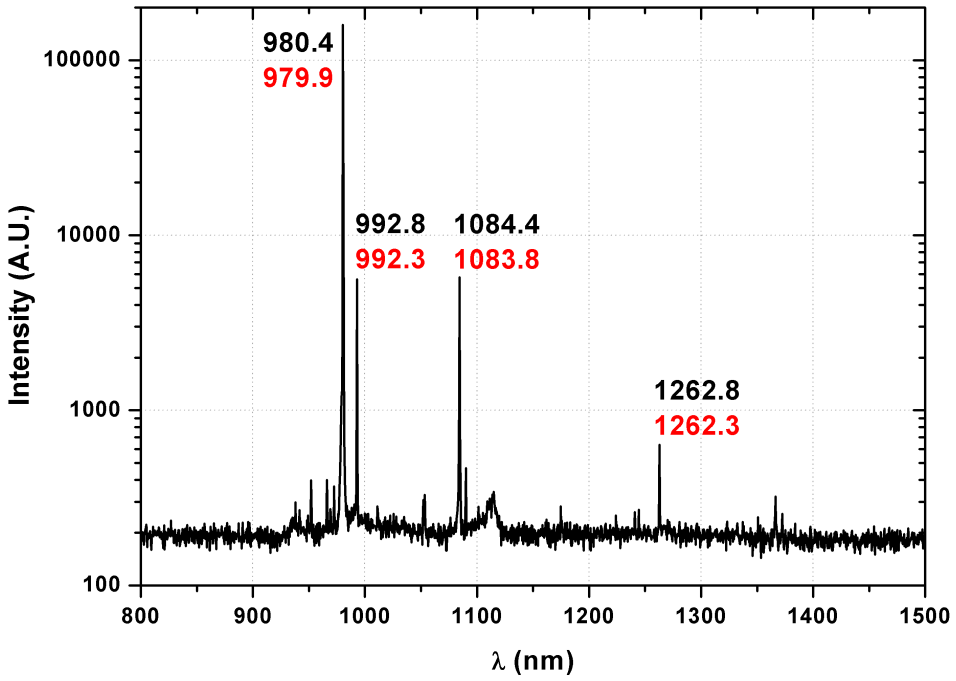

Figure 2.18: *The electron-beam (12 keV, 1μA) induced scintillation of gaseous argon doped with 1 ‰ xenon in the near-infrared. The spectrum was measured with the NIR-PMT. The resolution was 0.5 nm and the step size 0.1 nm. The black numbers show the wavelength positions (in nm) of the measured peaks and the red numbers for comparison the expected positions from xenon transitions expected by NIST [50]. From a comparison of the numbers it follows that the raw data have to be shifted by* ~ 0.5 *nm to shorter wavelengths.*

Chapter 3

The electron-beam induced scintillation of Pure and Xenon-Doped Liquid Argon from the Vacuum Ultraviolet to the Infrared

3.1 Wavelength-resolved Emission of Pure and Xenon-Doped Liquid Argon - Overview

Electron-beam (12 keV, 1.3 μA) induced scintillation of pure and xenon-doped liquid argon has been recorded in a wide wavelength range from 115 - 3500 nm. Fig. 3.1 shows[1] overview spectra representing part of the main results obtained in the present thesis. The upper panel shows the electron-beam induced scintillation of pure liquid argon and the lower panel depicts the electron-beam induced scintillation of liquid argon doped with 10 ppm xenon. To account for the wide wavelength range, the results obtained with the VUV photomultiplier (sensitive region: 115-850 nm) and with the InAs infrared photodiode (sensitive region: 500 - 3500 nm) are shown combined in the spectra on a logarithmic wavelength axis. The first important result is that pure liquid argon shows no scintillation in the infrared on the level of sensitivity which could be achieved with the InAs infrared photodiode. The second important result is that doping liquid argon with 10 ppm xenon leads to a shift of the main emission in the VUV from the argon excimer (127 nm peak wavelength) to the xenon excimer (174 nm peak wavelength) and simultaneously a second intense and broad scintillation feature in the near-infrared (NIR) is formed at 1173 nm peak wavelength. This discovery could pave the way towards a new particle discrimination concept based

[1]Note that in the VUV emission spectra presented in Figs. 3.1, 3.2 and 3.3 the wavelength interval from 120 to 140 nm is overestimated by a factor of ~ 2 compared to the wavelength interval from 155 to 190 nm (see subsection 2.3.1).

on the simultaneous detection of two optical signals in the VUV and in the NIR. The numbers next to the peaks are the wavelength-integrated scintillation efficiencies of the main emission features in photons per MeV electron energy deposited. The integration limits are: From 120 - 140 nm for pure liquid argon (upper panel, blue emission feature). From 155 - 190 nm for the VUV emission of xenon-doped liquid argon (lower panel, blue emission feature) and from 1100 - 1600 nm for the NIR emission of xenon-doped liquid argon (lower panel, red emission feature). The measurement procedure for the scintillation efficiencies in the different wavelength regions will be explained in detail in sections 3.3 and 3.4. The spectra are scaled in a way that the areas of the main emission features correspond to the scintillation efficiency values of the main emission features in photons/MeV. The different scalings between left and right axis are simply for demonstration purposes but they have the same absolute scale (left axis). A logarithmic representation of the wavelength axis is the only way to show both, the VUV as well as as the NIR emission in the same spectrum in a reasonable way since the full width at half maximum (FWHM) values differ by more than an order of magnitude (~ 10 nm for the VUV emission and ~ 100 nm for the NIR emission). Since both emissions have a comparable efficiency in terms of photons/MeV the peak intensity of the infrared emission would be 20 times smaller than represented now. Using the same ordinate for both emissions would lead to a situation where the NIR emission is depicted strongly suppressed compared to the VUV emission although the efficiencies (in photons/MeV) are comparable. This would misrepresent the physical meaning behind this discovery.

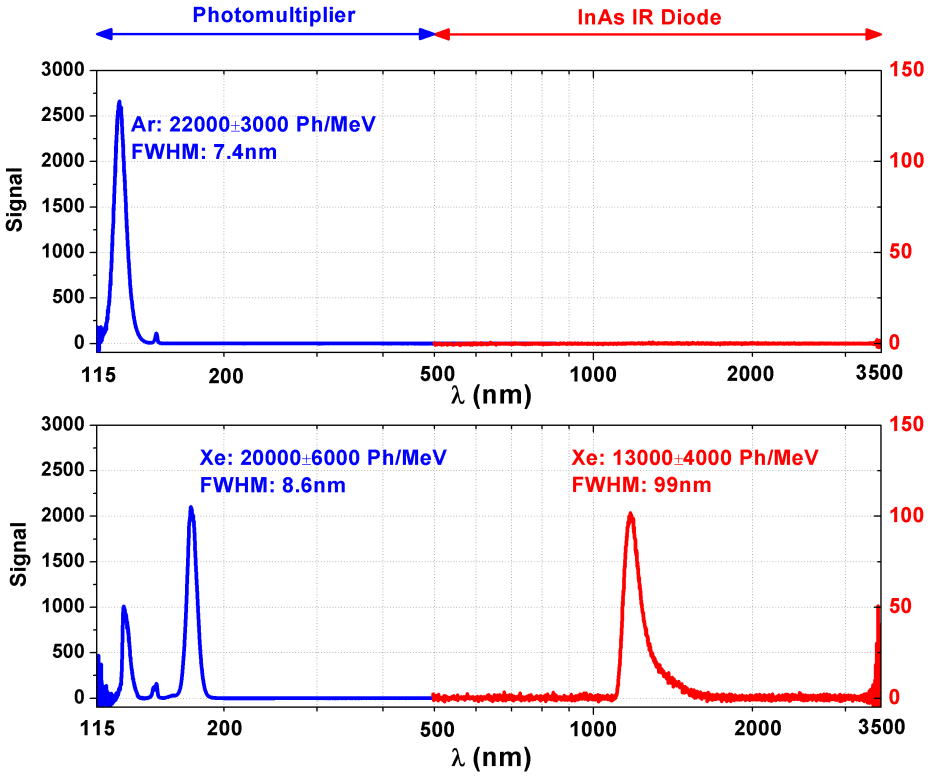

Figure 3.1: *The electron-beam (12 keV, 1.3 µA) induced scintillation of pure liquid argon (upper panel) and liquid argon doped with 10 ppm xenon (lower panel) is presented on a logarithmic wavelength axis. Pure liquid argon shows intense scintillation only in the VUV at 127 nm peak wavelength and no emission in the infrared (on the level of sensitivity of the InAs infrared photodiode) up to a wavelength of 3500 nm. The spectra are drawn from a combination of the results of the VUV photomultiplier (sensitive from 115 - 850 nm, blue curve) and the InAs infrared photodiode (sensitive from 500 - 3500 nm, red curve). The arrows on top of the upper panel indicate the wavelength regions measured with the different detectors. The signal of the photomultiplier in the wavelength region from 500 - 850 nm is not visible in this combined representation due to the increased noise of the InAs infrared photodiode. Doping liquid argon with 10 ppm xenon leads to a shift of the main VUV emission from the argon excimer (127 nm peak wavelength) to the xenon excimer (174 nm peak wavelength). In addition, an intense near-infrared emission is formed at 1173 nm peak wavelength. The small peak at 149 nm in the upper panel is due to a small residual xenon impurity from the gas system (compare Fig. 2.11). The numbers next to the peaks indicate the wavelength-integrated scintillation efficiencies in photons/MeV electron energy deposited and the full width at half maximum values (FWHM) of the main emission features. This figure is adapted from ref. [32].*

3.2 Spectral Modification with Xenon Concentration

A further aspect which has been studied is the amount of xenon which has to be added to liquid argon to result in an optimum light yield in terms of particle detector development. Therefore wavelength-resolved emission spectra with an exponential variation of the xenon concentration in argon have been recorded for the emission features in the VUV as well as in the NIR.

An important aspect which has to be mentioned here is that the actual xenon concentration in liquid argon in the cryogenic scintillation cell is difficult to determine. The preparation of the argon-xenon mixtures is performed in the gas phase when the scintillation cell is at room temperature. The amount of xenon in argon is controlled by measuring the partial pressure of xenon in the gas system prior to adding argon. When the scintillation cell is cooled to liquefy the scintillator material basically two counteracting processes have to be considered which alter the xenon concentration in the liquid compared to the gas phase: Firstly, the xenon concentration in liquid argon can to some extent be increased due to condensation of xenon atoms out of the buffer volume into the crygenic cell which acts as a cold trap for xenon. An upper limit of the xenon concentration in the liquid can be deduced from the complete amount of xenon which is filled into the gas system during the preparation of the mixtures in the gas phase. Approximately 40 % of the initial gas volume is condensed into the scintillation cell which corresponds to a maximum deviation of the xenon concentration in the cryogenic scintillation cell by a factor of ~ 2.5 if all the xenon is condensed out of the buffer volume into the cell. Secondly, the concentration in the liquid can to some extent be reduced due to condensation of xenon on the walls of the cryogenic cell. However, it has to mentioned that Cheshnovsky et al. [46] recorded α-induced scintillation spectra of liquid and solid noble gas alloys. An investigation of the optical absorption of xenon-doped liquid/solid argon indicated that the enrichment factor of xenon in liquid/solid argon (Xe-doping level 1-10 ppm) is less than ~ 2. A xenon aggregation in liquid argon seems also unlikely for xenon concentrations smaller than 30 ppm [82].

The additional alteration of the xenon concentration due to the accumulation of xenon from the initially "xenon-contaminated[2]" gas system in the cryogenic scintillation cell (see Fig. 2.11) can be neglected compared to the amounts of xenon (0.1, 1, 10, 100, 1000 ppm) which are intentionally added during the preparation of the argon-xenon gas-mixtures.

Since the exact amount of xenon in the cryogenic cell can not be determined the xenon-concentrations which are stated below always refer to the gas phase during the preparation of the argon-xenon mixtures.

[2]In the studies on pure liquid argon, xenon acted as an impurity which could not be removed completely from the gas system. The distillation procedure strongly reduces xenon in "pure" liquid argon but never removes it in such a way that the emission feature related to xenon (at 149 nm) in liquid argon vanishes completely.

3.2.1 Vacuum Ultraviolet

The electron-beam (12 keV, 1.3 μA) induced scintillation of liquid argon in the vacuum ultraviolet doped with xenon concentrations varied by factors of 10 is presented in Figs. 3.2 and 3.3 (upper panel). The most important trend which can be observed is a shift of the main emission from the argon excimer (127 nm peak wavelength) to the xenon excimer (174 nm peak wavelength). Note that at 10 ppm xenon[3] in liquid argon, the energy transfer from the argon excimer to the xenon excimer is almost complete (86 % compared to the 1000 ppm mixture).

The xenon emission at 149 nm can be attributed to weakly bound ArXe* excimers [83] and becomes smaller with increasing xenon concentration due to the branching ratio between argon-xenon and xenon-xenon excimer-formation. In addition, the undisturbed xenon resonance emission ($^3P_2 \rightarrow {}^1S_0$) at 147 nm begins to grow with increasing xenon concentration. Here it is interesting to note that at 10 ppm xenon in liquid argon both emissions (147 and 149 nm) have almost the same intensity. A xenon related absorption feature at 126.5 nm can be seen (very distinct in the 1 ppm mixture in the upper panel of Fig. 3.3) which broadens towards shorter wavelengths.

3.2.2 Infrared

The electron-beam (12 keV, 1.3 μA) induced scintillation of xenon-doped liquid argon in the infrared is shown in Fig. 3.4. The xenon concentrations were varied by factors of 10 from 0.1 ppm to 1000 ppm and the spectra were recorded using the InAs infrared photodiode. The different mixtures and the corresponding results could be reproduced very well within $\pm$10 %. The most important information is that adding xenon to liquid argon leads to the formation of an intense asymmetrically shaped near-infrared emission. The highest intensity was measured at a xenon concentration of 10 ppm in liquid argon with a peak wavelength of 1173 nm and a full width at half maximum (FWHM) of 99 nm [32]. Fig. 3.5 shows a high-resolution (wavelength resolution: 0.5 nm) spectrum of the electron-beam (12 keV, 1.3 μA) induced scintillation of liquid argon doped with 10 ppm xenon measured with a near-infrared photomultiplier (Hamamatsu NIR-PMT Module H10330B-45 SEL). Due to increased sensitivity of the photomultiplier and the huge dynamic range compared to the InAs infrared photodiode it was possible to confirm the asymmetrically shaped and intense near-infrared emission (1173 nm peak wavelength, FWHM: 99 nm) and to detect two minor emission features centered at 964 nm (FWHM: 28 nm) and 1024 nm (FWHM: 27 nm). The emission feature centered at 964 nm was probably already observed by Heindl et al. [44] in pure liquid argon (see Fig. 1.7). Until now it was not possible to clarify whether the near-infrared emission in Fig. 1.7 was real or an artifact from the normalization with the detector response function of the spectrometer used in that measurement. A measurement with the NIR-PMT in pure liquid argon will finally clarify this issue.

[3] A xenon concentration of 10 ppm in liquid argon leads to maximal light output in the near-infrared region (see Fig. 3.4).

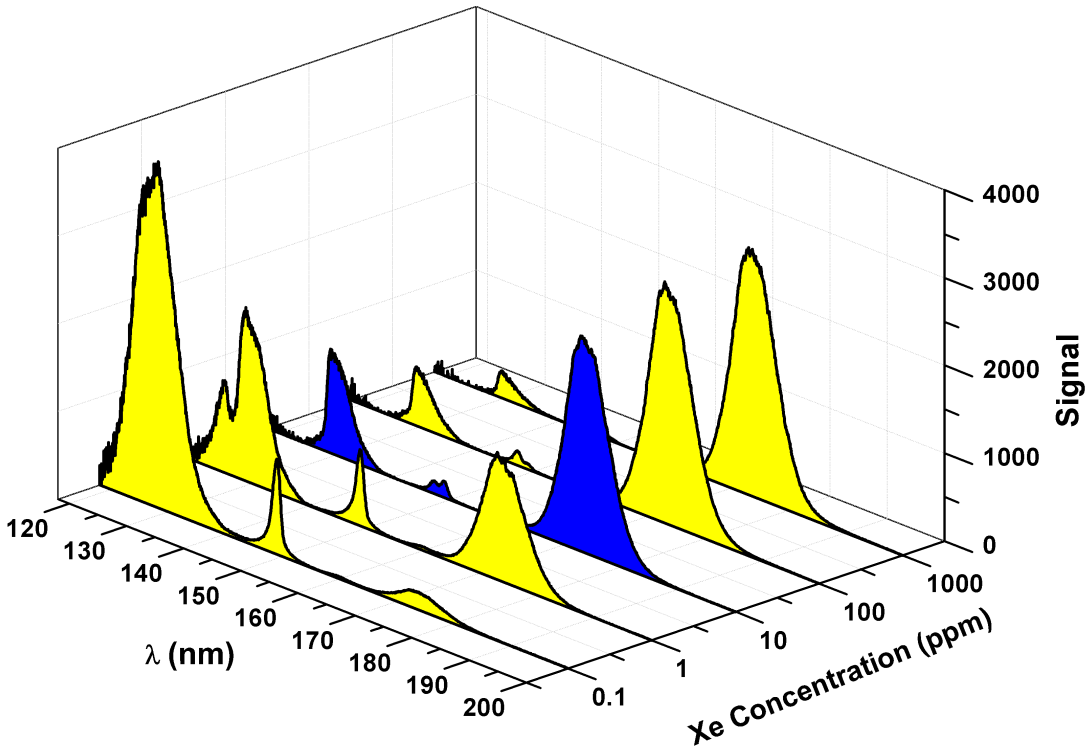

Figure 3.2: *The xenon-concentration dependent alteration of the electron-beam induced VUV emission of xenon-doped liquid argon is shown. A shift of the main emission from the argon excimer (127 nm peak wavelength) to the xenon excimer (174 nm peak wavelength) is clearly visible. The concentrations are changed by factors of 10. At a xenon concentration of 1 ppm a very distinct absorption dip at 126.5 nm can be seen which broadens towards shorter wavelengths with increasing xenon concentrations. At a xenon concentration of 10 ppm (blue shaded spectrum) the corresponding near-infrared emission has a maximum (see e.g. Fig. 3.4). This figure is adapted from ref. [32].*

In this context it also interesting to note that the intense near-infrared emission is formed only in the liquid and not in the gas phase [68]. Fig. 3.6 shows the electron-beam induced emission of argon doped with 1000 ppm xenon in the gas phase just before condensation and (for comparison) the emission of liquid argon doped with 10 ppm xenon. In a series of spectra in the gas phase in analogy to Fig. 3.4 it turned out that the intensity of the most prominent XeI line (Racah notation: $6s\,[1\frac{1}{2}]_2$ - $6p\,[\frac{1}{2}]_1$) at 0.98 μm [50] increases with xenon concentration. The strong energy transfer from argon to a 6s-6p line in xenon had been observed before [84, 85].

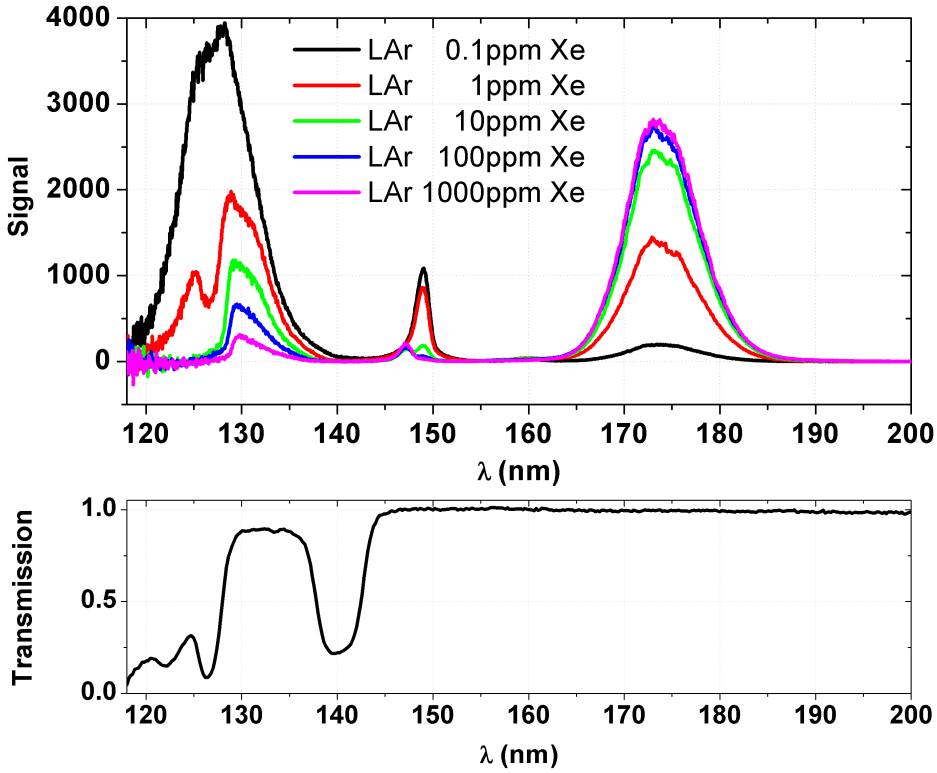

Figure 3.3: *The upper panel shows the electron-beam (12 keV, 1.3μA) induced VUV scintillation of xenon-doped liquid argon with xenon concentrations varied by factors of 10 (from 0.1 ppm to 1000 ppm) in analogy to Fig. 3.2. Note that at 10 ppm xenon in liquid argon, the energy transfer from the argon excimer (127 nm peak wavelength) to the xenon excimer (174 nm peak wavelength) is almost complete (86 % compared to the 1000 ppm mixture). The 10 ppm mixture has maximum light output in the near-infrared region (see Fig. 3.4). The ArXe* [83] emission at 149 nm decreases with increasing xenon concentration and the undisturbed xenon resonance line at 147 nm occurs. The lower panel shows the transmission spectrum of xenon-doped liquid argon (0.1 ppm xenon) measured with a deuterium light source and a length of the optical path of 11.6 cm. A strong xenon-related absorption feature at 126.5 nm center wavelength can be seen which is also visible in the upper panel (1 ppm mixture, red line). In the emission spectra presented here the light had to travel only 2 mm from the light emitting spot at the entrance membrane to the first MgF_2 window. This figure is adapted from ref. [32].*

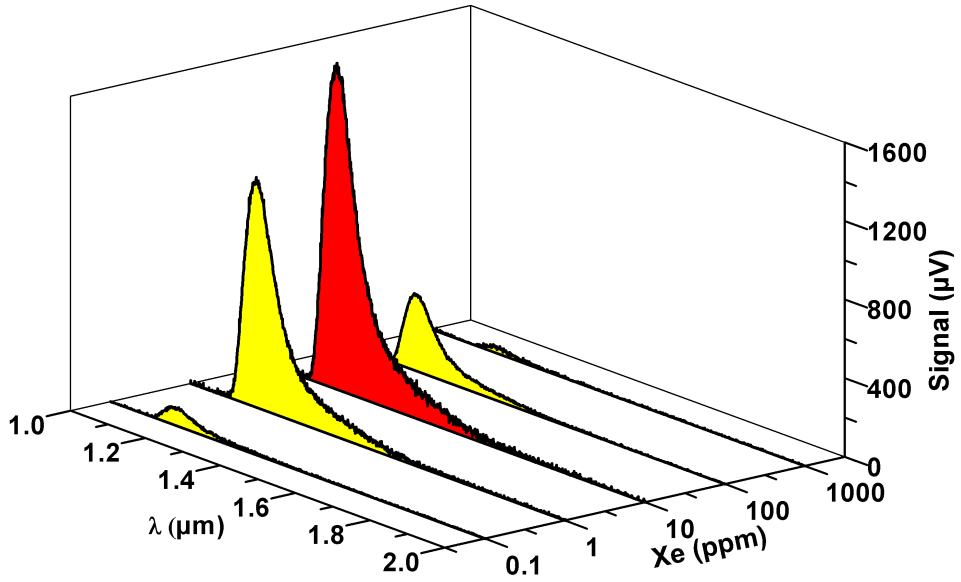

Figure 3.4: *The electron-beam (12 keV, 1.3µA) induced infrared emission of xenon-doped liquid argon is shown. The xenon concentrations in liquid argon were varied by factors of 10 from 0.1 to 1000 ppm. The red spectrum denotes the 10 ppm mixture for which the most intense IR emission was found. Note the different units of the wavelength axis (µm compared to nm in Fig. 3.2). The data have been adapted from ref. [68].*

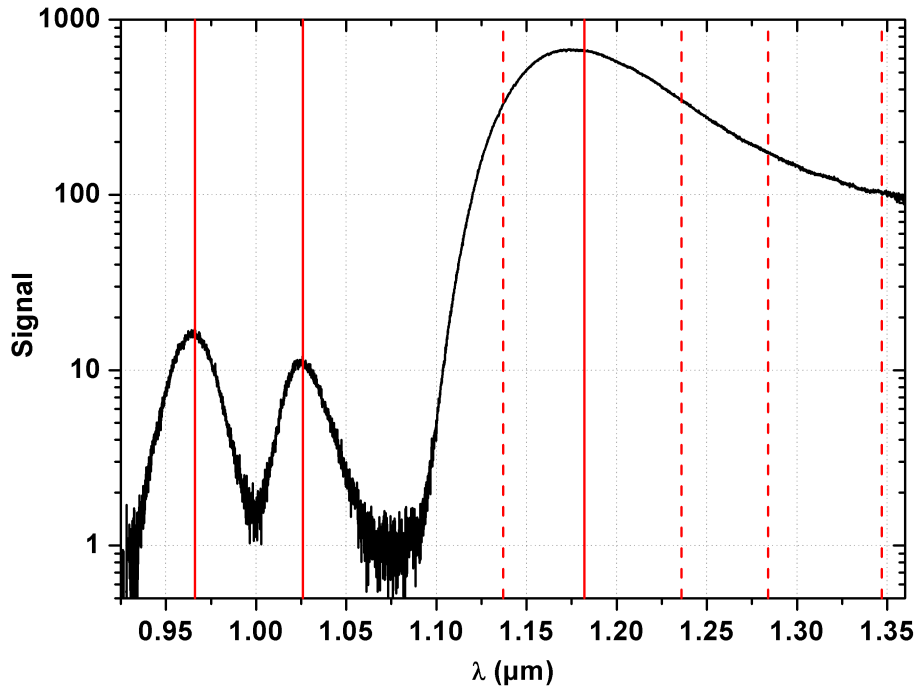

Figure 3.5: *A high-resolution near-infrared emission spectrum of liquid argon doped with 10 ppm xenon under electron-beam excitation (12 keV, 1.3 μA) is shown. The spectrum has been measured using a NIR-PMT (Hamamatsu NIR-PMT Module H10330B-45 SEL) and the wavelength resolution is 0.5 nm which is an order of magnitude higher than the measurements with the InAs infrared photodiode (wavelength resolution: 5 nm). The intense asymmetrically shaped near-infrared emission feature could be confirmed and the high sensitivity and the high dynamic range of the NIR-PMT enabled to detect two minor emission features centered at 964 and 1024 nm. The red solid lines denote wavelength positions where time structure measurements have been performed and time spectra are presented in section 3.5. The red dashed lines denote wavelength positions where additional time structure measurements have been performed. This figure is adapted from ref. [32].*

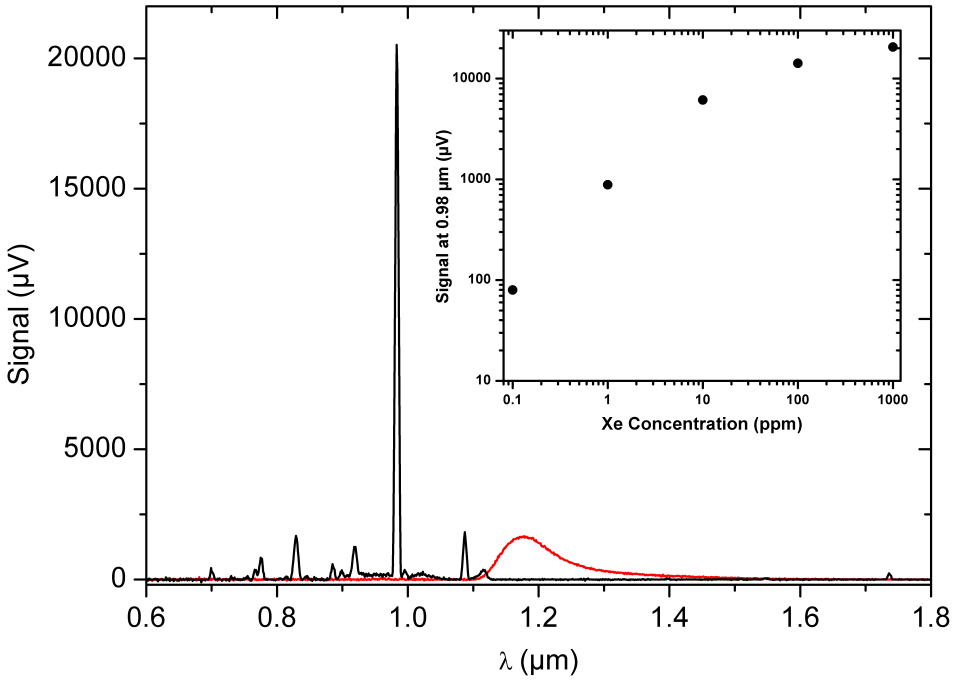

Figure 3.6: *The electron-beam induced emission spectrum of gaseous argon doped with 1000 ppm xenon (black line, T=100 K, p = 1255 mbar) is shown as well as the emission spectrum of liquid argon doped with 10 ppm xenon (red line). In the gas phase a strong energy transfer from argon to xenon is visible in the most prominent XeI line (6s-6p) at 0.98 µm. The inset shows the peak intensity of this line under variation of the xenon concentration by factors of 10. This figure is adapted from ref. [68].*

3.3 Efficiency Measurements in the Vacuum Ultraviolet

A very important parameter in the context of the application of the VUV (174 nm center wavelength) emission as well as the newly found near-infrared emission in particle detectors is the scintillation efficiency. A high scintillation efficiency leads to a high number of photons per event and thus to a high sensitivity of the detector. In this section the results on the scintillation efficiency in the vacuum ultraviolet of pure liquid argon and xenon-doped liquid argon are presented. The scintillation efficiency of pure liquid argon was also measured to perform a direct comparison between pure liquid argon and xenon-doped liquid argon under the same experimental conditions.

Due to the practically identical spectral shapes of the excimer emissions of pure liquid argon compared to pure gaseous argon and xenon-doped liquid argon compared to pure gaseous xenon, the scintillation efficiency of both emission features could be measured using the data in ref. [14]. The scintillation efficiencies of pure gaseous argon and pure gaseous xenon were measured in ref. [14] using exactly the same excitation method as in the present experiment. The excimer-light intensities were measured using a NIST/PTB calibrated optical semiconductor detector (SXUV-100, IRD inc.) at a certain distance (without any optical windows) between excimer light-source and detector. The conversion efficiency (energy efficiency) from electron-beam power to excimer light is $(33 \pm 4)\,\%$ for pure gaseous argon and $(42 \pm 5)\,\%$ for pure gaseous xenon. The conversion efficiencies are constant in a pressure range from $\sim (400 - 1400)\,\mathrm{mbar}$ [14].

To obtain the scintillation efficiencies in the liquid phase, the inner cell was filled with pure gaseous argon and pure gaseous xenon, respectively, at room temperature and a pressure of $\sim 1000\,\mathrm{mbar}$. Emission spectra were recorded with an electron energy of 12 keV and a current of $1.3\,\mu\mathrm{A}$. This corresponds to a power deposition of $(11.1 \pm 1.5)\,\mathrm{mW}$ in pure gaseous argon and $(9.1 \pm 1.3)\,\mathrm{mW}$ in pure gaseous xenon[4]. Then, pure liquid argon and liquid argon doped with 10 ppm xenon were prepared and liquefied. The practically identical shape of the emission of gaseous argon compared to liquid argon and gaseous xenon compared to xenon-doped liquid argon allowed a measurement of the wavelength-integrated scintillation efficiency. The integration limits are from 115 - 145 nm for pure liquid argon and from 150 - 200 nm for liquid argon doped with 10 ppm xenon.

However, the efficiency measurements rely on the exact amount of energy deposited in the gas compared to the liquid. Since this is a crucial parameter, a dedicated GEANT4 [70] simulation was performed to obtain the mean energy deposited in the scintillating medium behind the ceramic entrance membrane (see b in Fig. 2.2) by an incident 12 keV electron. Figs. 3.7 and 3.8 show GEANT4-simulated [70] distributions of deposited energies of 12 keV electrons (primary electrons) after the transmission through the entrance membrane. In the simulations a 12 keV

[4]GEANT4 simulations show that the mean energy deposited by an incident 12 keV electron after the ceramic membrane is 8.5 keV in gaseous argon and 7.0 keV in gaseous xenon. See discussion below.

electron beam with a diameter of 0.5 mm was sent through a 300 nm thin ceramic entrance membrane (77 nm SiO_2 and 223 nm Si_3N_4 [69]) and the amount of energy deposited behind the ceramic membrane in the gas and the liquid, respectively, was written into a histogram for each electron. In the case of pure argon, the mean energy deposited by a primary electron is 8.5 keV independent of the state of aggregation.

Fig. 3.8 shows that the distribution of the deposited energies in gaseous xenon compared to liquid argon doped with 10 ppm xenon is different although the amount of transmitted electrons is the same. The mean energy deposited by a 12 keV primary electron is 7.0 keV for pure gaseous xenon and 8.5 keV for liquid argon doped with 10 ppm xenon. Due to the higher atomic number of xenon compared to argon the probability for backscattering is higher for xenon which can be seen by the larger amount of low-energy depositions in the distribution of the deposited energies when gaseous xenon compared to liquid argon doped with 10 ppm xenon is the target medium after the entrance membrane.

According to the discussions in refs. [14, 69] where GEANT4 and CASINO-simulated electron-energy distributions after the transmission through the entrance membrane were compared to measurements, a 10 % error is assumed for the results obtained by the GEANT4 simulation.

In Fig. 3.9 the electron-beam induced emission spectrum of pure gaseous argon compared to pure liquid argon is shown. The energy efficiency is calculated according to eq. 3.1:

$$\varepsilon_{LAr} = \frac{\int_{115\,nm}^{145\,nm} S_{LAr}(\lambda)d\lambda}{\int_{115\,nm}^{145\,nm} S_{GAr}(\lambda)d\lambda} \cdot \varepsilon_{GAr} \tag{3.1}$$

ε_{LAr}**:** Energy efficiency of liquid argon

$S_{LAr}(\lambda)$**:** Measured signal when the inner cell is filled with pure liquid argon

$S_{GAr}(\lambda)$**:** Measured signal when the inner cell is filled with pure gaseous argon

ε_{GAr}**:** Energy efficiency of gaseous argon ((33 ± 4) % [14])

The result is that the energy efficiency drops from (33 ± 4) % [14] to (21 ± 3) % when the argon is liquefied. With a mean scintillation wavelength of 127 nm this corresponds to a scintillation efficiency of (22 000±3 000) photons per MeV electron energy deposited.

This value is approximately a factor of two below the scintillation efficiency (40 000 ± 2 000 photons/MeV) measured by Doke et al. [86, 87] and not consistent within the error bars. A variation of the beam current from 1.3 μA down to 100 nA showed a constant scintillation efficiency. However, track-to-track quenching can not be excluded completely since the beam current could not be reduced below 100 nA in a controlled way. A GEANT4 [70] simulation showed that the mean track length which the electrons travel before they are stopped is $\sim 2.7\,\mu$m and the mean

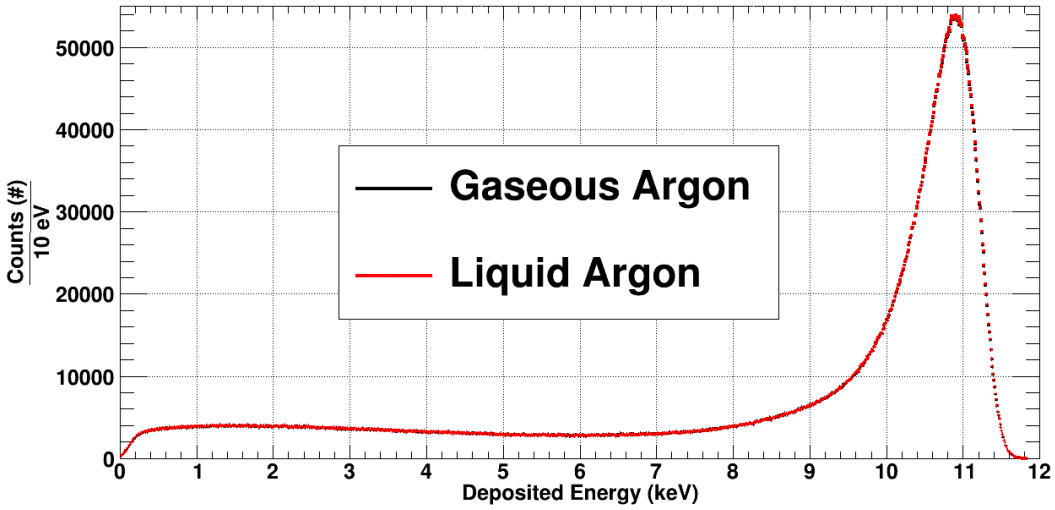

Figure 3.7: *The simulated distributions of the energies deposited in pure gaseous argon (black line) and pure liquid argon (red line) are shown. In the GEANT4 simulations* 10^7 *primary (12 keV) electrons were sent through a 300 nm thin ceramic entrance membrane (77 nm* SiO_2 *and 223 nm* Si_3N_4 *[69]) and the amount of energy deposited behind the ceramic membrane in the gas and the liquid, respectively, was recorded for each electron. The distribution is the same for gaseous and liquid argon. Therefore, the black curve is not visible due to the overlaying red curve. The mean energy deposited by a 12 keV incident electron is 8.5 keV in both cases and 91 % of all electrons are transmitted through the entrance membrane. Note that the distribution shown here takes into account backscattered electrons from the medium behind the entrance membrane.*

distance perpendicular to the entrance membrane is $\sim 1.5\,\mu$m. Therefore, the excitation process happens in a very thin layer of argon close to the entrance membrane. A radiationless deexcitation of atoms and molecules at the surface of the entrance membrane may be an additional reason for the reduced scintillation efficiency compared to refs. [86, 87]. However, note that Doke et al. [86, 87] used relativistic electrons with an energy of 0.976 MeV and a range of 0.39 cm from a radioactive source[5] compared to 12 keV electrons ($\sim$ 8.5 keV after the entrance membrane with a range of 2.7 μm) from a cathode ray tube in the present experiment. To compare the excitation conditions caused by different incident projectiles and energies, the linear energy transfer (LET) is calculated according to eq. 3.2:

[5] Internal conversion electrons from ^{207}Bi.

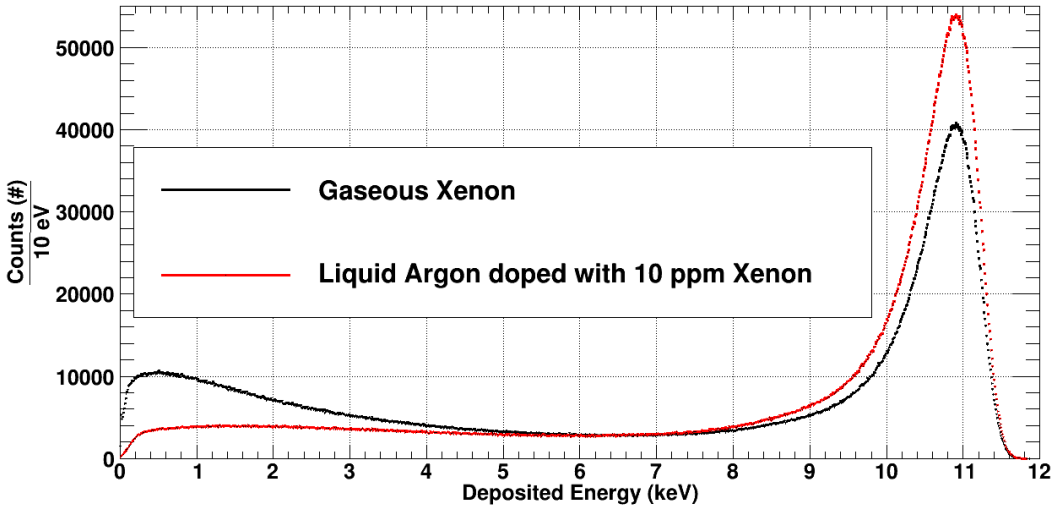

Figure 3.8: *The simulated distributions of the energies deposited in pure gaseous xenon (black line) and liquid argon doped with 10 ppm xenon (red line) are shown. In the GEANT4 simulations* 10^7 *primary (12 keV) electrons were sent through a 300 nm thin ceramic entrance membrane (77 nm* SiO_2 *and 223 nm* Si_3N_4 *[69]) and the amount of energy deposited behind the ceramic membrane in the gas and the liquid, respectively, was recorded for each electron. Due to the increased backscattering in gaseous xenon the amount of low-energy depositions is higher compared to liquid argon doped with 10 ppm xenon. The mean energy deposited per primary electron in gaseous xenon is 7.0 keV and 8.5 keV for liquid argon doped with 10 ppm xenon. The amount of transmitted electrons through the ceramic entrance membrane is 91 % in both cases. Note that the distribution shown here takes into account backscattered electrons from the medium behind the entrance membrane.*

$$\mathrm{LET} = \frac{\mathrm{E}}{\mathrm{x} \cdot \rho} = 22.6 \, \frac{\mathrm{MeV} \cdot \mathrm{cm}^2}{\mathrm{g}} \tag{3.2}$$

LET Linear energy transfer in $\frac{\mathrm{MeV \cdot cm^2}}{\mathrm{g}}$

E Energy of the incident electrons ($8.5 \cdot 10^{-3}$ MeV after the entrance membrane)

x Mean Track length of the electrons until they are stopped ($2.7 \cdot 10^{-4}$cm)

ρ Density of liquid argon ($1.394 \frac{\mathrm{g}}{\mathrm{cm}^3}$)

The relativistic electrons Doke et al. used had an LET of $1.8 \, \frac{\mathrm{MeV \cdot cm^2}}{\mathrm{g}}$ [86, 87] and the electrons used in the current experiment had an LET of $22.6 \, \frac{\mathrm{MeV \cdot cm^2}}{\mathrm{g}}$. According to Fig. 2 in ref. [87] the scintillation efficiency decreases for lower LETs which consequently cannot explain the scintillation efficiency measured with the current setup. There are also measurements with nonrelativistic protons [87] with an energy

of 38.2 MeV and a range of 1.8 cm which leads to an LET of 18.3 $\frac{\mathrm{MeV \cdot cm^2}}{\mathrm{g}}$ which is very close to the LET of the present experiment. The published scintillation efficiency from Doke et al. [87] (at an LET of 18.3 $\frac{\mathrm{MeV \cdot cm^2}}{\mathrm{g}}$) is a factor of two higher than the current measurement and in apparent disagreement.

However, calculations aiming to model the quenching processes in liquid argon under charged-particle impact show that quenching is not only affected by the LET but also by the detailed structure of the excited volume [88]. This means that at the same LET, different particle tracks can develop different quenching ratios depending on the detailed structure of the density of the energy deposited. Therefore, the results obtained by Doke et al. [86, 87] and in the current experiment do not necessarily contradict each other. The energy range and therefore the shape of the excited volumes are completely different in the current experiment compared to that of Doke et al. [86, 87]. The small excitation volume in the current experiment could lead to a decreased scintillation efficiency (quenching) due to scintillator non-proportionality which is caused by exciton-exciton quenching [89]. This discussion shows that more detailed investigations on the scintillation efficiency are necessary. Especially in the low-energy region it is important to understand quenching effects since pushing the low-energy thresholds of particle detectors towards the low-energy limit requires a profound knowledge of the scintillation efficiency in that energy region.

It has to emphasized that the efficiency measurements presented in the current chapter can be traced back to a NIST/PTB calibrated optical semiconductor-detector without any optical elements between excimer light-source and detector. Furthermore this is the first time that the scintillation efficiency of liquid argon has been measured using such low-energy electrons. For further details see refs. [31, 32, 41].

To obtain the VUV energy efficiency of xenon-doped liquid argon, the reduced mean electron energy deposited in gaseous xenon compared to liquid argon doped with 10 ppm xenon has to be included in the calculation which is shown in eq. 3.3:

$$\varepsilon_{LArXe} = \frac{\int_{150\,nm}^{200\,nm} S_{LArXe}(\lambda)d\lambda}{\int_{150\,nm}^{200\,nm} S_{GXe}(\lambda)d\lambda} \cdot \varepsilon_{GXe} \cdot \frac{\bar{E}_{GXe}}{\bar{E}_{LArXe}} \tag{3.3}$$

ε_{LArXe}**:** Energy efficiency of liquid argon doped with 10 ppm xenon

$S_{LArXe}(\lambda)$**:** Measured signal when the inner cell is filled with liquid argon doped with 10 ppm xenon

$S_{GXe}(\lambda)$**:** Measured signal when the inner cell is filled with gaseous xenon

ε_{GXe}**:** Energy efficiency of gaseous xenon ((42 ± 5) % [14])

$\bar{E}_{GXe}$**:** Mean energy deposited per primary (12 keV) electron in gaseous xenon ((7.0 ± 0.7) keV, see Fig. 3.8)

$\bar{E}_{LArXe}$**:** Mean energy deposited per primary (12 keV) electron in liquid argon doped with 10 ppm xenon ((8.52 ± 0.85) keV, see Fig. 3.8)

In Fig. 3.10 the electron-beam induced emission spectrum of pure gaseous xenon compared to liquid argon doped with 10 ppm xenon is shown. A comparison of the wavelength integrated (150 - 200 nm) intensities (according to eq. 3.3) shows that the energy efficiency of liquid argon doped with 10 ppm xenon is $(14 \pm 4)\,\%$. The mean (and peak) scintillation wavelength in xenon-doped liquid argon is at 174 nm, thus, the scintillation efficiency is (20 000±6 000) photons per MeV electron energy deposited.

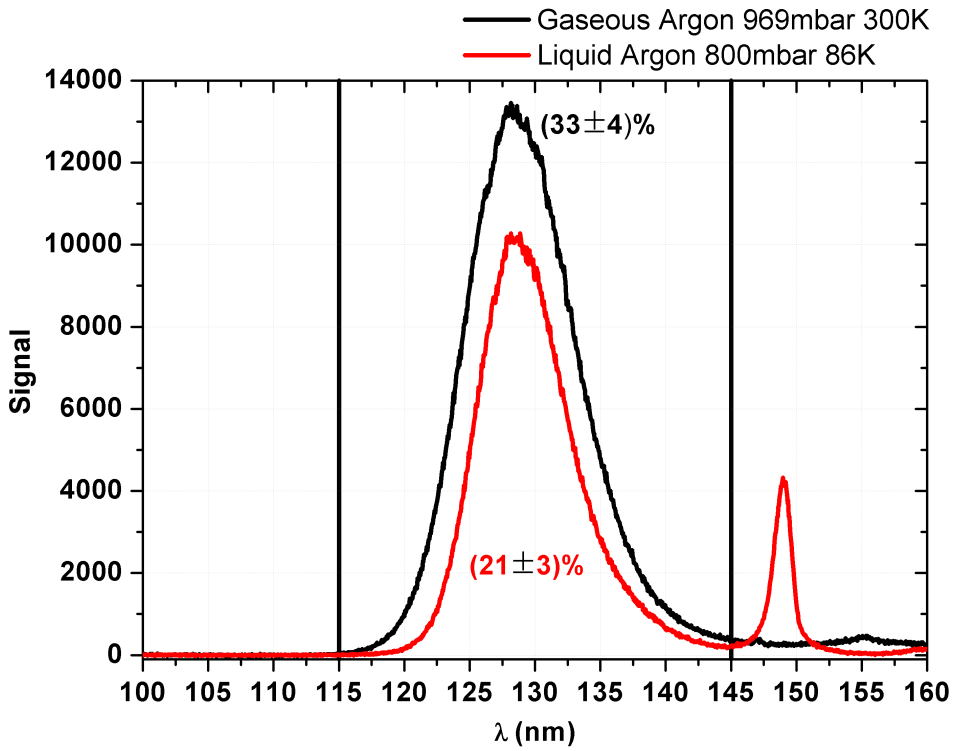

Figure 3.9: *The electron-beam induced (12 keV, 1.3 μA) scintillation of gaseous (black line) and liquid (red line) argon is shown. The black vertical lines indicate the integration limits (115 - 145 nm) to obtain the wavelength-integrated energy efficiency. The black number is the conversion efficiency from electron-beam power to excimer light for gaseous argon at room temperature adapted from ref. [14]. The red number is the conversion efficiency for liquid argon using the ratio of the integrals according to eq. 3.1 in the gas and the liquid phase. The emission feature in liquid argon at 149 nm peak wavelength can be attributed to a xenon impurity. Note that no responsivity correction (see Fig. 2.7) is applied to the spectra which leads to a strongly exaggerated representation of the xenon impurity-emission compared to the argon excimer.*

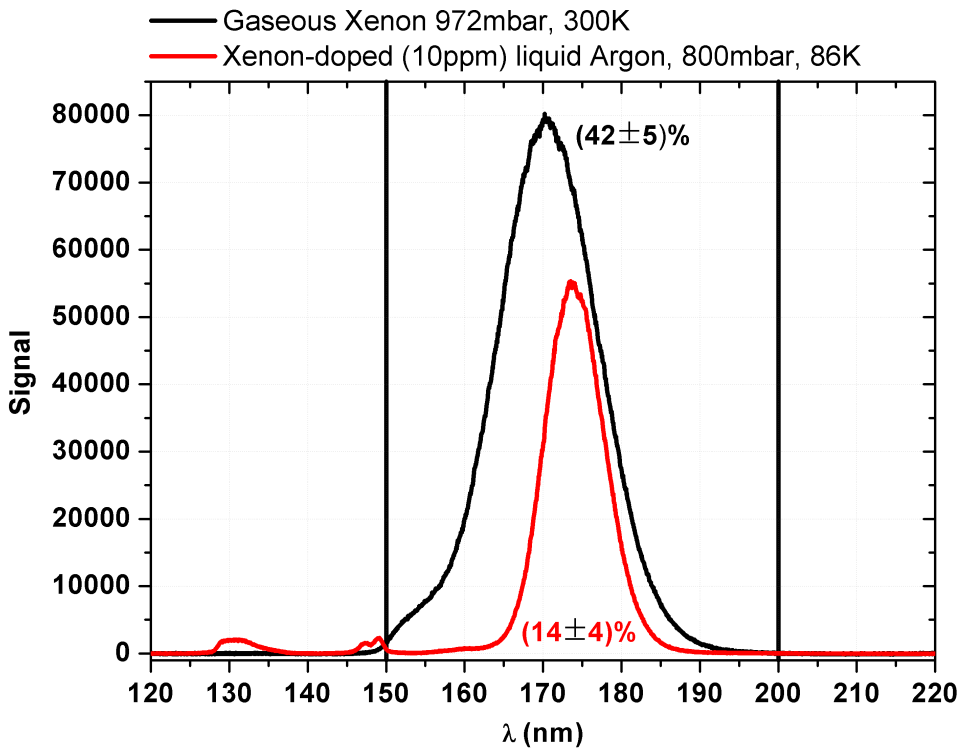

Figure 3.10: *The electron-beam induced (12 keV, 1.3 μA) scintillation of gaseous xenon (black line) and liquid argon doped with 10 ppm xenon (red line) is shown. The black vertical lines indicate the integration limits (150 - 200 nm) to obtain the wavelength-integrated energy efficiency. The black number is the conversion efficiency from electron-beam power to excimer light for gaseous xenon at room temperature adapted from ref. [14]. The red number is the conversion efficiency for liquid argon doped with 10 ppm xenon using the ratio of the integrals in the gas and the liquid according to eq. 3.3. Due to the identical spectral shape and the almost identical wavelength region no responsivity correction (see Fig. 2.7) is applied to the spectra. In addition, it has to be mentioned that the responsivity curve is basically flat in that wavelength region. Therefore, the wavelength-integrated efficiency values are independent of the wavelength-dependent responsivity of the experimental setup.*

3.4 Efficiency Measurements in the Infrared

In analogy to the vacuum ultraviolet emission also the scintillation efficiency of the newly found near-infrared emission has to be measured to judge whether an application in a particle detector is feasible. To measure the wavelength-integrated scintillation light intensity the elliptical mirror (j in Fig. 2.1) was removed and the InAs infrared photodiode was mounted at a distance of approximately 21 cm between the infrared-emitting spot and the detector surface. The photocurrent of the InAs infrared photodiode was amplified and converted to a voltage by the transimpedance pre-amplifier (Teledyne Judson, Model: PA-6-60) and read out with a digital storage oscilloscope (LeCroy Waverunner 6050). To get rid of drift effects and offset problems the electron beam was pulsed with a repetition rate of 5 kHz and a pulse duration of 100 μs. The light intensity could be measured using the signal difference between on and off-time of the electron-beam. Fig. 3.11 shows, as an example, a measurement obtained with a mean beam current of 0.7 μA i.e. 1.4 μA in the pulse.

Prior to the measurements it was carefully checked that the focus and the magnets of the electron beam are optimized to maximal light intensity. This is important because the beam current is measured within the high voltage power supply of the cathode ray tube and therefore one has to make sure that the current which is measured in the high-voltage power supply also reaches the entrance membrane without defocusing or steering losses.

The upper panel in Fig. 3.11 shows the trigger signal for the pulsed electron beam from the high voltage power supply of the cathode ray tube using the full bandwidth of the oscilloscope (500 MHz). The lower panel in Fig. 3.11 shows the measured signal from the transimpedance pre-amplifier. The pre-amplifier has a bandwidth of 60 kHz and the data were digitally low-pass filtered with a bandwidth of 80 kHz and averaged 10 000 times to improve the signal to noise ratio. The mean values of the signal with beam on and off are indicated by the horizontal black lines in the lower panel. The measured infrared intensity is proportional to the signal difference between beam on and off. The signal difference was determined for each of the eight steps in the lower panel of Fig. 3.11 and an average value was calculated.

Fig. 3.12 shows the measured signal of the pre-amplifier under beam-current variation. The data point at 1.4 μA beam current corresponds to the analysis of the data presented in the lower panel of Fig. 3.11. The pre-amplifer signal shows a linear trend with beam-current variation. Note that the line does not go through zero which indicates an offset in the absolute measurement of the beam current. However, due to the measurement of a series of beam currents it is possible to use the gradient which is independent of an offset in the beam-current measurement. The signal variation with changing beam current is determined to $(82.2 \pm 5.3)\frac{\mu V}{\mu A}$.

The energy efficiency in the near-infrared calculated according to eq. 3.4 is (1.3 ± 0.4) % and the corresponding scintillation efficiency is $(13\,000 \pm 4000)$ photons per MeV electron energy deposited.

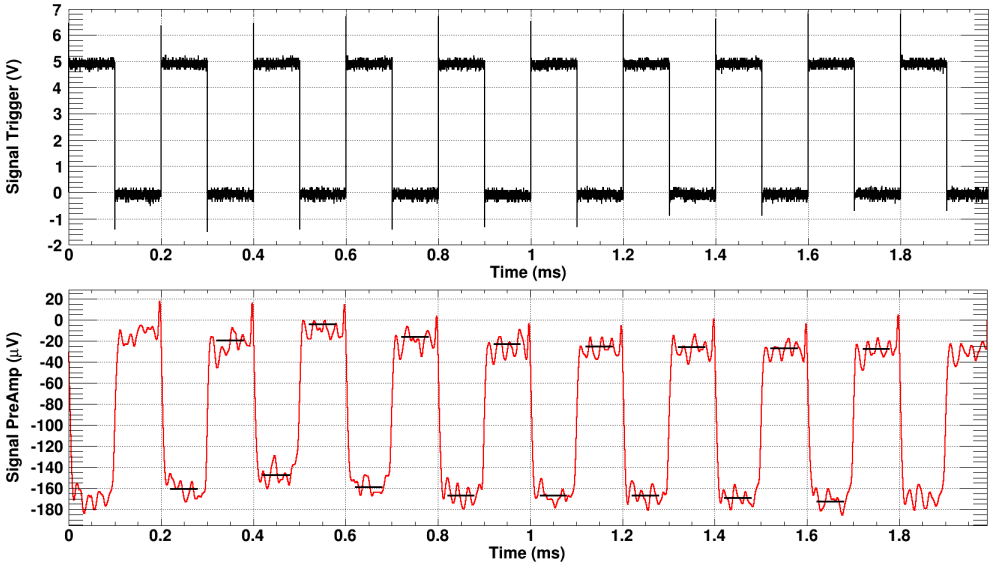

Figure 3.11: *The trigger signal from the high-voltage supply of the pulsed cathode ray tube measured with a digital storage oscilloscope (LeCroy Waverunner 6050) is shown (upper panel). The electron beam was pulsed with a repetition rate of 5 kHz and a pulse duration of 100 µs which corresponds to a duty cycle of 50 %. The mean beam-current was 0.7 µA and, thus, 1.4 µA during the pulse. The trigger signal was measured using the full bandwidth (500 MHz) of the oscilloscope. The measured signal from the pre-amplifier of the InAs infrared photodiode is shown in the lower panel. The pre-amplifier has a bandwidth of 60 kHz and the signal was digitally low-pass filtered with a bandwidth of 80 kHz and averaged 10 000 times to improve the signal-to-noise ratio. The black horizontal lines are the mean values of the signal when the electron beam is on and off, respectively.*

$$\varepsilon_{NIR} = \frac{x \cdot 4 \cdot \pi \cdot d^2}{G \cdot A_{Det} \cdot R(\lambda) \cdot \bar{E}_{el}} \tag{3.4}$$

ε_{NIR}**:** Energy efficiency of liquid argon doped with 10 ppm xenon in the near-infrared

$x = (82.2 \pm 5.3)\,\frac{V}{A}$**:** Measured pre-amplifier signal under beam-current variation (see Fig. 3.12)

$d = (210 \pm 10)\,mm$**:** Distance between infrared emitting spot and surface of the InAs infrared photodiode

$G = 1\,005\,000\,\frac{V}{A}$**:** Measured gain of the pre-amplifier according to the datasheet

$A_{Det} = 0.78\,mm^2$**:** Active area of the InAs photodiode (active diameter: 1 mm)

$R(\lambda)$**:** Wavelength-dependent responsivity of the InAs infrared photodiode (see Fig. 2.13)

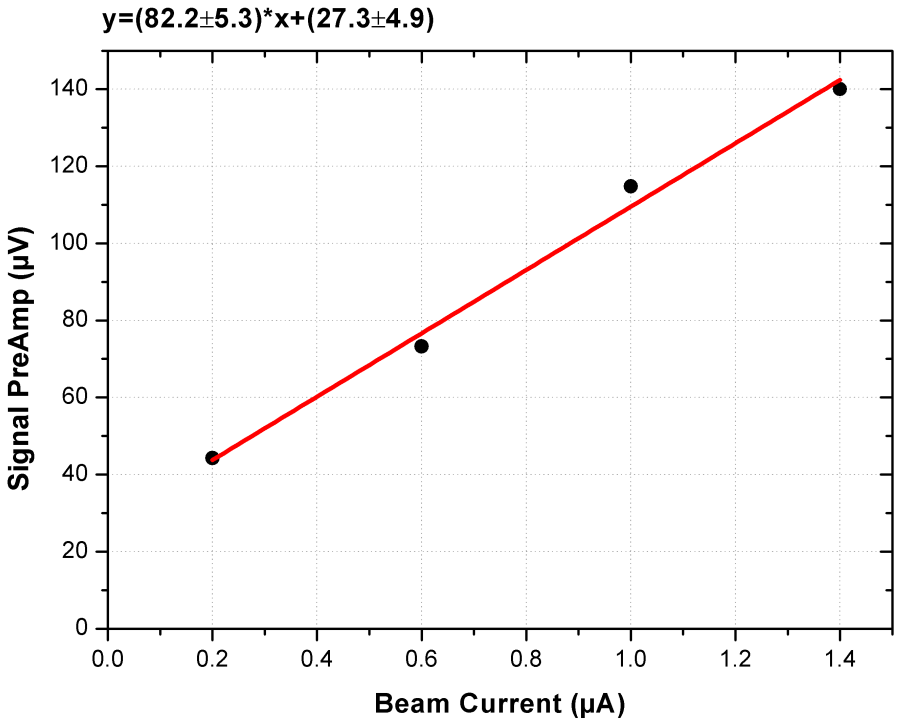

Figure 3.12: *The measured pre-amplifier signal under beam-current variation is shown. The data point at 1.4 µA corresponds to the analyzed data from the lower panel of Fig. 3.11. The pre-amplifier voltage and consequently the emitted near-infrared radiation shows a linear variation (red line, described by the equation on top of the figure) with beam current. An offset in the absolute measurement of the beam current is also visible. For the calculation of the scintillation efficiency the gradient of the signal variation with beam current is used which is independent of the offset.*

$\bar{E}_{el}$**:** Mean energy deposited per primary (12 keV) electron in liquid argon doped with 10 ppm xenon ((8.52 ± 0.85) keV, see Fig. 3.8)

The asymmetric shape of the near-infrared emission leads to a 4 % error in the energy efficiency if simply the responsivity ($R(\lambda = 1173\,nm) = 0.48\,\frac{A}{W}$) at the peak of the near-infrared emission is used in eq. 3.4. Therefore the energy efficiency is calculated including the spectral information in the following way: The measured near-infrared raw-data spectrum was background corrected and scaled to an integral (integration limits: 1100 - 1600 nm) amount of signal equal to the measured (and wavelength integrated) pre-amplifier signal ($x = (82.2 \pm 5.3)\,\frac{V}{A}$). Efficiency values at each measured wavelength position in the emission spectrum were calculated using eq. 3.4 where x corresponds to the signal in the scaled spectrum at a certain wavelength. The integral efficiency could be obtained by integrating the wavelength resolved efficiency spectrum. The scintillation efficiency in photons per MeV electron energy deposited was calculated in a similar way.

Here it is interesting to note that although the energy efficiency ($(1.3 \pm 0.4)\,\%$) in the near-infrared is an order of magnitude smaller than in the VUV ($(14 \pm 4)\,\%$) the scintillation efficiencies in photons per MeV electron energy deposited have comparable values (NIR: $13\,000 \pm 4\,000$ compared to VUV: $20\,000 \pm 6\,000$) due to large energy difference (factor of approximately 7) between VUV and near-infrared photons.

A systematic aspect which is not included in the calculation is the loss of scintillation light due to reflection at the surfaces of the two MgF_2 windows (see Fig. 2.1) in front of the InAs infrared photodiode. An estimation[6] of the loss of scintillation light based on Fresnel's formulas for normal incidence of light shows that scintillation light losses are of the order of 8 %. Note that in any real experiment where the scintillating medium is separated from the light detector by a window, similar light losses have to be expected.

At this point it is interesting to summarize the results (of the efficiency measurements) obtained so far. The wavelength-integrated scintillation efficiencies of pure liquid argon in the VUV and liquid argon doped with 10 ppm xenon in the VUV as well as in the near-infrared enable to calculate wavelength-integrated scintillation efficiencies of the other mixtures by comparing the integrals of the emission spectra. The efficiencies of the argon-excimer emission in xenon-doped liquid argon are calculated by integrating the spectra in Fig. 3.2 from 120 to 140 nm and normalizing them to the measured efficiency of pure liquid argon ($(22\,000 \pm 3000)$ photons per MeV electron energy deposited, see the upper panel of Fig. 3.1). The xenon-excimer scintillation efficiencies of xenon-doped liquid argon in the VUV are calculated by integrating the spectra in Fig. 3.2 from 155 - 190 nm and normalizing the values to the measured efficiency of liquid argon doped with 10 ppm xenon ($(20\,000 \pm 6000)$ photons per MeV electron energy deposited, see the lower panel of Fig. 3.1). The scintillation efficiencies in the near-infrared are calculated by integrating the spectra in Fig. 3.4 from 1100 - 1600 nm and normalizing them to the measured efficiency of liquid argon doped with 10 ppm xenon in the near-infrared ($(13\,000 \pm 4000)$ photons per MeV electron energy deposited). The wavelength-integrated scintillation efficiencies in the VUV and in the near-infrared are shown in Fig. 3.13 for xenon concentrations varied by factors of 10.

[6] This estimation is based on the models for the wavelength dependence of the refractive indices of liquid argon [73, 74] and MgF_2 [75] which are extrapolated to the infrared region.

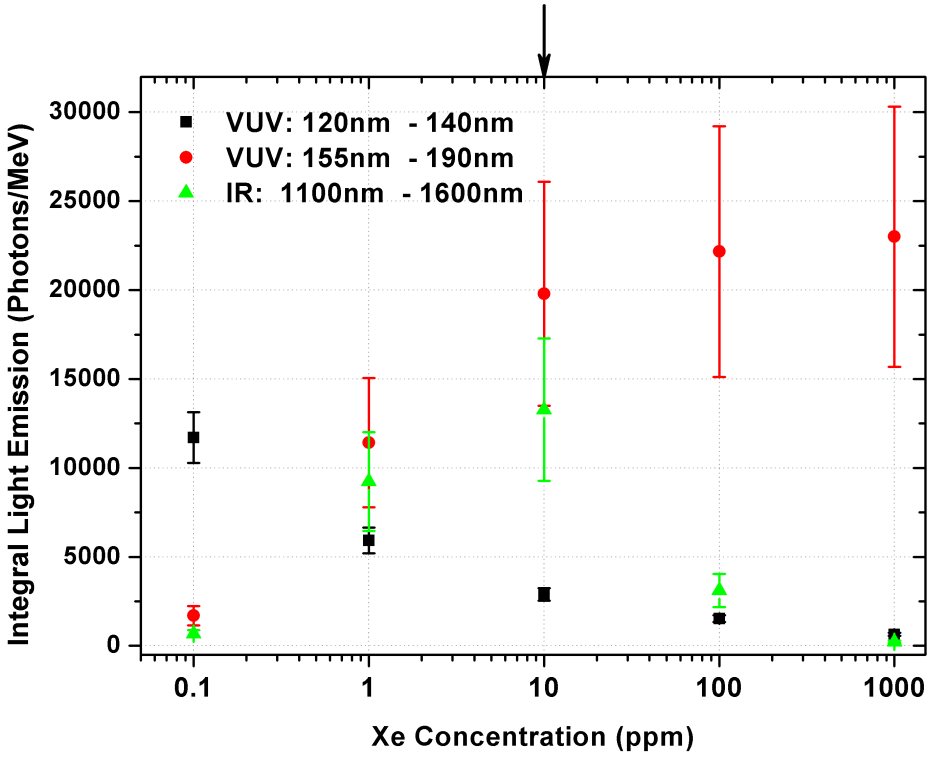

Figure 3.13: *The integral amount of scintillation light (in photons per MeV electron energy deposited) from argon excimers (120 - 140 nm, black squares) and xenon excimers (155-190 nm, red dots) are shown for xenon concentrations varied by factors of 10. The green triangles represent the integral (1100 - 1600 nm) amount of light from the near-infrared emission. The energy transfer from argon to xenon is clearly visible by the decreasing argon emission and the increasing xenon emission in the VUV. The 10 ppm mixture shows maximal light output in the near-infrared and, in addition, the energy transfer in the VUV is almost complete (86 % compared to 1000 ppm mixture). The black arrow on top of the figure indicates the 10 ppm mixture which has also a maximum in the overall light output. This figure is adapted from ref. [32].*

3.5 Time-Structure Measurements using a Pulsed Electron Beam

The time structure of the emitted scintillation light after the excitation by an incident particle is a further important aspect to judge the feasibility of xenon-doped liquid argon as detector medium. A short decay time after the excitation of the scintillating medium leads to a low noise level and a low dead-time which are important figures of merit for a particle detector.

Therefore the time structures of liquid argon doped with 10 ppm xenon in the VUV ((174 ± 0.5) nm) and in the NIR ((1182 ± 0.8) nm) have been measured using a standard time-to-amplitude conversion technique. The electron beam was pulsed with a repetition rate of 8 kHz and a pulse duration of 100 ns. The trigger signal of the high-voltage power supply of the cathode ray tube was used as a start signal for the time-to-amplitude converter[7] (ORTEC 566) and the photomultiplier pulse from the first detected photon was used as a stop signal. The time-to-amplitude-converter generated an analog voltage proportional to the time difference between start and stop pulse. These analog voltages were digitized with an analog-to-digital converter (ORTEC AD413A) and recorded in a histogram to obtain the time structure. The intensity of the scintillation light was adjusted by the slit width of the monochromator to detect one photon every 50 th to 100 th pulse. It has to be mentioned here that neither a variation of the photon rate nor a variation of the beam current (factor of 16) in the pulses changed the measured time structures in the VUV and the NIR.

Prior to the measurements of the time structure of the most intense scintillation features in xenon-doped liquid argon, the exact shape of the excitation pulse had to be measured. Therefore, a time-structure measurement of the third-continuum emission (see Fig. 1.5) of pure gaseous argon has been performed. It is known ([58] and references therein) that the third continuum of gaseous argon has a very short decay-time constant which should reproduce a 100 ns excitation pulse in quite an undisturbed way. Fig. 3.14 shows the measured time structure of the excitation pulse in pure gaseous argon (1261 mbar and room temperature) at a wavelength of (180 ± 2.6) nm. The excitation pulse has an overall duration of 100 ns with a substructure in intensity that peaks at 35 ns.

Fig. 3.15 presents the measured time structures of liquid argon doped with 10 ppm xenon at (131 ± 2.1) nm, (174 ± 0.5) nm and (1182 ± 0.8) nm. The latter two wavelengths correspond to the most intense emission wavelengths of the mixture. The data are shifted in time to match at zero. However, it has to be mentioned that only the measurement at 131 and at 174 nm have the same temporal zero point since they were measured using the same photomultiplier (VUV-PMT, ET Enterprises, D860B). The measurement at 1182 nm has been performed with a near-infrared photomultiplier (Hamamatsu NIR-PMT Module H10330B-45 SEL) which has a different internal delay compared to the VUV-PMT.

So far no model describing the time structures can be given since no concentration-

[7] The time range of the time-to-amplitude converter has been calibrated using a precision pulse generator (Stanford Research DG535).

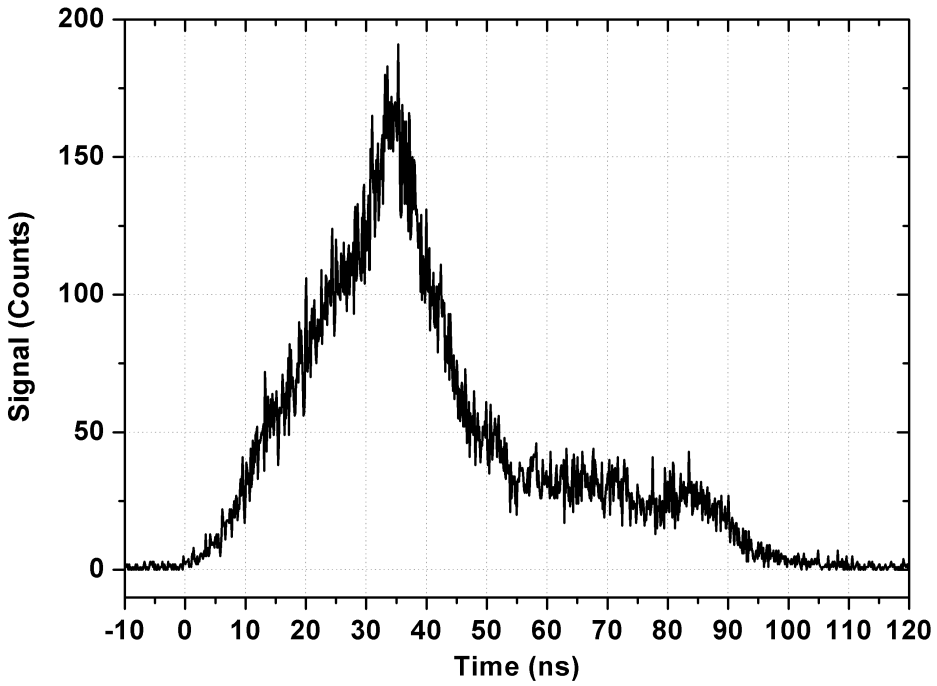

Figure 3.14: *The time structure of the excitation pulse is shown. The measurement has been performed using a pulsed electron beam with a repetition rate of 8 kHz and a pulse duration of 100 ns. The pulse shape has been measured using the third continuum emission at* (180 ± 2.6) *nm of pure gaseous argon (p = 1261 mbar) at room temperature. The pulse has an overall duration of 100 ns with a substructure in intensity which peaks at* ~ 35 *ns pulse duration.*

dependent measurements of the time structures are available to identify the different processes and the corresponding rate constants of the reaction chains. Therefore, all the decay-time constants presented in the following are just phenomenological best-fit values of exponential decays which are fitted to the data.

The VUV emission from the xenon excimers (174 nm) peaks at ~ 250 ns which is ~ 150 ns after the end of the excitation pulse. Between 250 ns and 1 μs the light intensity decreases with a continuously reduced decay-time constant. After 1 μs the decay can be described very well by an exponential decay with a decay-time constant of (240 ± 10) ns.

The red lines in Fig. 3.5 denote wavelength positions (1137, 1182, 1284, 1347 nm) where time-structure measurements of the NIR main emission have been performed. The best-fit values of the decay-time constants at these five different wavelength positions had a maximum deviation of 15 % around a mean value of 175 ns. This leads to the assumption that no further IR emitting species with significantly different time constants are involved. Time-structure measurements at more wavelength positions

with significantly higher statistics have to be performed to reduce the statistical errors and to resolve a potential wavelength-dependent time structure within this intense NIR emission. Therefore, the discussion below is related to the measured time structure at 1182 nm.

The NIR emission at 1182 nm peaks faster than the VUV emission at 174 nm. The decay of the 174 nm VUV emission can be described with a single exponential decay-time constant only after the NIR emission has decayed completely. During the decay of the NIR emission the decay-time constant of the 174 nm VUV emission changes from a slower to a faster decay. This could be a hint that the 174 nm VUV emission is a transition in a cascade following the NIR emission.

The time structure measured at 131 nm (compare Fig. 3.3, upper panel) can be attributed to the emission of argon excimers consisting of two components. A fast (singulet) component reproducing the excitation pulse (compare Fig. 3.14) and a slow component (triplet) with a time constant of (202 ± 2) ns. Here, the triplet lifetime of the argon excimers is strongly reduced due to the energy transfer from argon to xenon. The triplet lifetime in pure liquid argon measured with the present setup is of the order of 1 μs [41, 44].

In summary, both main emission features measured at 174 nm and 1182 nm have decayed completely after approximately 2.0 μs and 1.2 μs, respectively. For the application in a particle detector these time structures are well suited. No long-living components are involved which would increase the noise level and the dead time of a detector.

The time structures of the two minor near-infrared emissions at 964 and 1024 nm peak wavelength (see Fig. 3.5) have also been measured. Fig. 3.16 shows the time structures which have the same temporal zero point since both were measured using the same NIR-PMT. Both emission features have much longer decay times than the decay times of the main emission features at 174 nm and 1182 nm (black and red curve in Fig. 3.15, respectively).

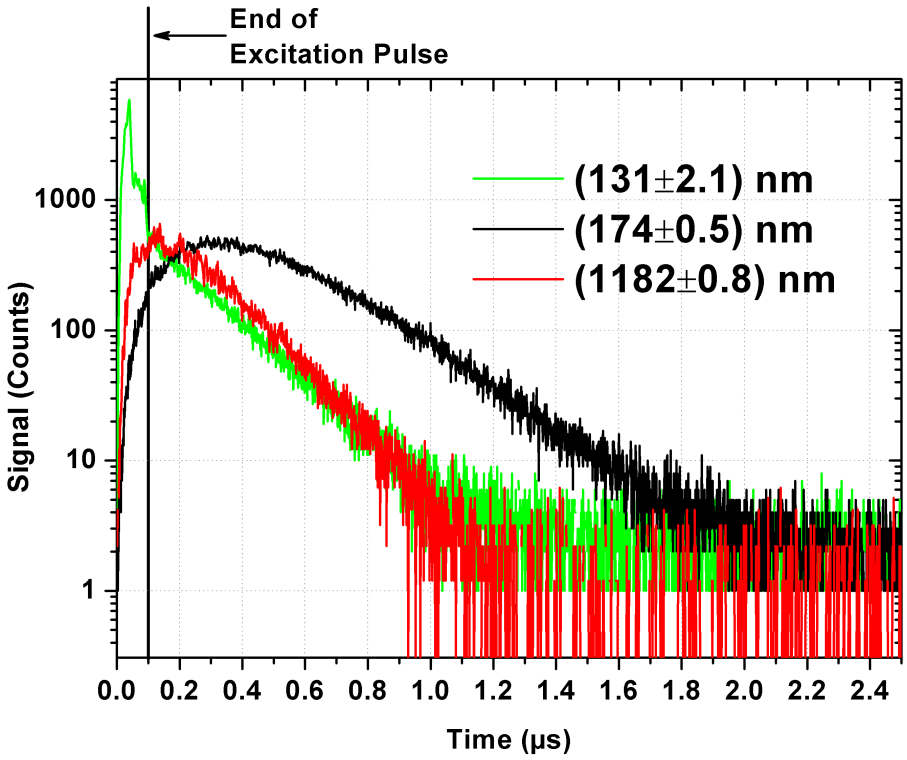

Figure 3.15: *The time structures of the scintillation light (VUV and NIR) of electron-beam-excited liquid argon doped with 10 ppm are shown. The excitation pulse had a duration of 100 ns with a substructure in intensity which can be seen in Fig. 3.14. The black curve shows the time structure of the most intense emission feature in the VUV measured at 174 nm (Xe excimer). The red curve shows the time structure of the most intense emission structure in the NIR measured at 1182 nm. For comparison, in green, also the emission in the VUV at 131 nm is shown which can be attributed to argon excimers. For details see text. This figure is adapted from ref [32].*

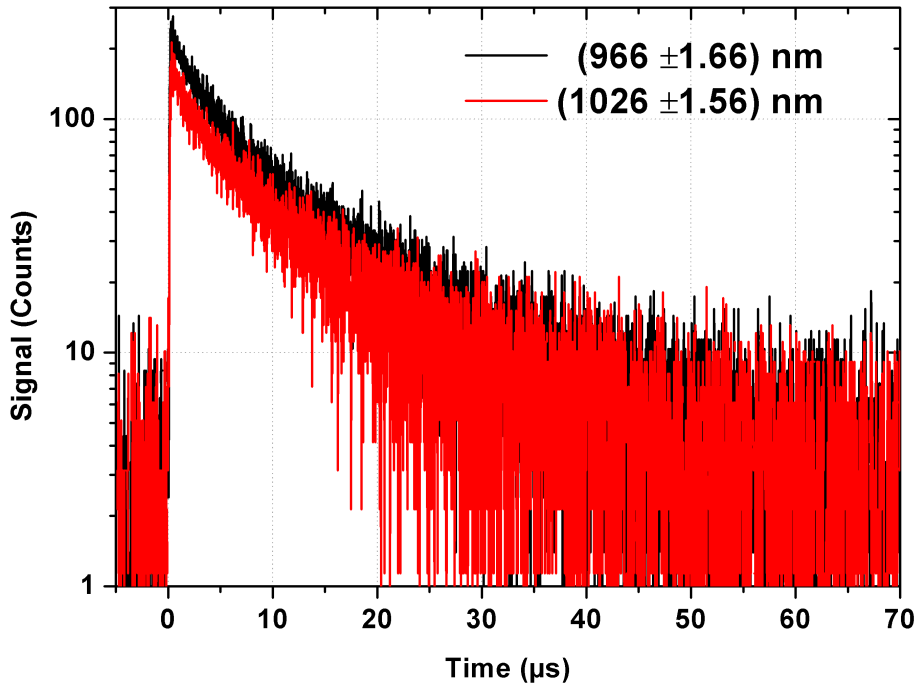

Figure 3.16: *The time structures of electron-beam induced scintillation of the near-infrared emission features measured at* (966 ± 1.66) *(black curve) and* (1026 ± 1.56) *nm (red curve) are presented. The excitation pulse had a duration of 100 ns (see Fig. 3.14). Both emission features have much longer decay times than the main emission features in the VUV as well as in the NIR (compare Fig. 3.15). This figure is adapted from ref. [32].*

Chapter 4

Optical Transmission of Liquid Noble Gases in the Vacuum Ultraviolet

One way to increase the sensitivity of a liquid noble-gas particle-detector is to increase its sensitive volume (i.e. the scintillating volume). A general trend towards increasing detector volumes can be observed in currently working as well as future experiments (see section 1.2 and references therein) using liquid noble gases to detect rare events[1]. Therefore, it is important not only to have a high scintillation efficiency and a well suited scintillation time structure but also a transparent medium for its own scintillation light. Increasing the detector volumes leads to increased optical path lengths the scintillation light has to traverse until it is detected.

A figure of merit for the transparency of a scintillator for its own scintillation light is the so-called attenuation length Λ_{att}. The attenuation length is the distance after which the initial intensity of light traversing a scintillator has dropped by a factor of $\frac{1}{e}$.

The attenuation of light is the sum of absorption and scattering losses and is described according to equation 4.1:

$$I(x,\lambda) = I_0(\lambda) \cdot \exp\left(-\frac{x}{\Lambda_{att}(\lambda)}\right) \tag{4.1}$$

$$\rightarrow \Lambda_{att}(\lambda) = \frac{x}{\ln\left(\frac{I_0(\lambda)}{I(x,\lambda)}\right)} \tag{4.2}$$

$$\rightarrow \Lambda_{att}(\lambda) = \frac{x}{\ln\left(\frac{1}{T(x,\lambda)}\right)} \tag{4.3}$$

$I(x,\lambda)$**:** Wavelength-dependent light intensity after a traversed optical path length x

[1]Events like a WIMP recoiling off a target nucleus, a neutrino recoiling off an electron of the scintillator medium or the neutrinoless double-beta decay.

$I_0(\lambda)$**:** Wavelength-dependent initial intensity (e.g. the scintillation spectrum)

$\Lambda_{att}(\lambda)$**:** Wavelength-dependent attenuation length

$T(x, \lambda)$**:** Wavelength-dependent transmission of a layer of thickness x

The transmission of a liquid noble gas sample with a certain optical path length is the parameter which has to be measured to obtain the attenuation length. An important novel aspect compared to previous publications on attenuation length measurements of liquid noble gas samples [90, 91, 92, 93] is the wavelength-resolved measuring principle. A wavelength-integrated measuring principle cannot disentangle the influence of impurities like water vapor, oxygen, or other noble gases which have a strong impact on the measured transmission [33, 42]. Impurities, depending on their concentrations, affect both the emission as well as the transmission spectrum. Any wavelength-integrated measuring principle can therefore only measure a combined effect of emission and transmission. Thus, the obtained "attenuation length" strongly depends on impurities.

Here, it has to be noted that the results on the attenuation of vacuum ultraviolet light in pure liquid argon are also published in ref. [33] and - focusing on the technical apects of attenuation measurements in a more general sense - in ref. [53]. The results on the attenuation of vacuum ultraviolet light in xenon-doped liquid argon are published in ref. [94]. Due to the very detailed descriptions in the publications mentioned above the systematic effects are only briefly discussed in the present thesis.

In the following sections the experimental setup is briefly described and the results are presented with a strong focus on the main physical results.

4.1 Experimental Setup

A cut through the experimental setup used for the transmission measurements of the liquid noble gas samples is shown in Fig. 4.1. A basic optical setup was used to avoid complications (e.g. changes due to geometry when the sample cell is cooled down) in the interpretation of the results. Vacuum ultraviolet light from a deuterium light source (Cathodeon Model V03) was sent through 11.6 cm sample of liquid noble gas. A spectrum of the deuterium lamp after passing the evacuated sample cell with two MgF_2 windows is shown in Fig. 4.2.

The transmitted light was analyzed using an evacuated VUV spectrometer (f=30 cm McPherson 218 monochromator with image intensified diode detector array). The cell containing the liquid noble gas samples was mounted inside an evacuated vacuum cross piece with 100 mm inner diameter (CF100). The gas handling system is depicted in Fig. 2.3 and described in section 2.2. Due to the larger volume ($\sim 13\,\mathrm{cm}^3$) of the inner cell in Fig. 4.1 compared to the scintillation cell ($\sim 2\,\mathrm{cm}^3$) depicted in Fig. 2.2 both reservoirs (L and M in Fig. 2.3) were used to prepare the gas samples for the transmission measurements. Temperature regulation of the inner cell was performed via a computer-controlled temperature-regulation system based on a PI

regulation loop. A platinum resistive sensor (Pt100) glued to the inner cell provided the temperature information and a heating resistor (47 Ω, 20 W) was used for temperature regulation.

In the following the term "attenuation of light" instead of "absorption of light" is used since sending a light beam through a sample and comparing the light intensity for a filled and an empty inner cell cannot disentangle the effect of absorption and light scattering.

A VUV sensitive detector was mounted under an angle of 90° with respect to the VUV beam probing the sample to test if there is a significant amount of stray- and scintillation light. The VUV photodiode (Opto Diode Corp. model AXUV20A, attached to flange D in Fig. 4.1) could observe the sample at a distance of ~ 17 cm. It was read out by a nanoamperemeter with a sensitivity down to 20 nA full scale. The VUV photodiode had a responsivity of $0.15\frac{\mathrm{A}}{\mathrm{W}}$ [95] at a wavelength of 127 nm which leads to an optical sensitivity of ~ 133 nW for reemitted scintillation light. However, in none of the measurements, neither in pure liquid argon nor in xenon-doped liquid argon a significant signal has been measured by the VUV photodiode.

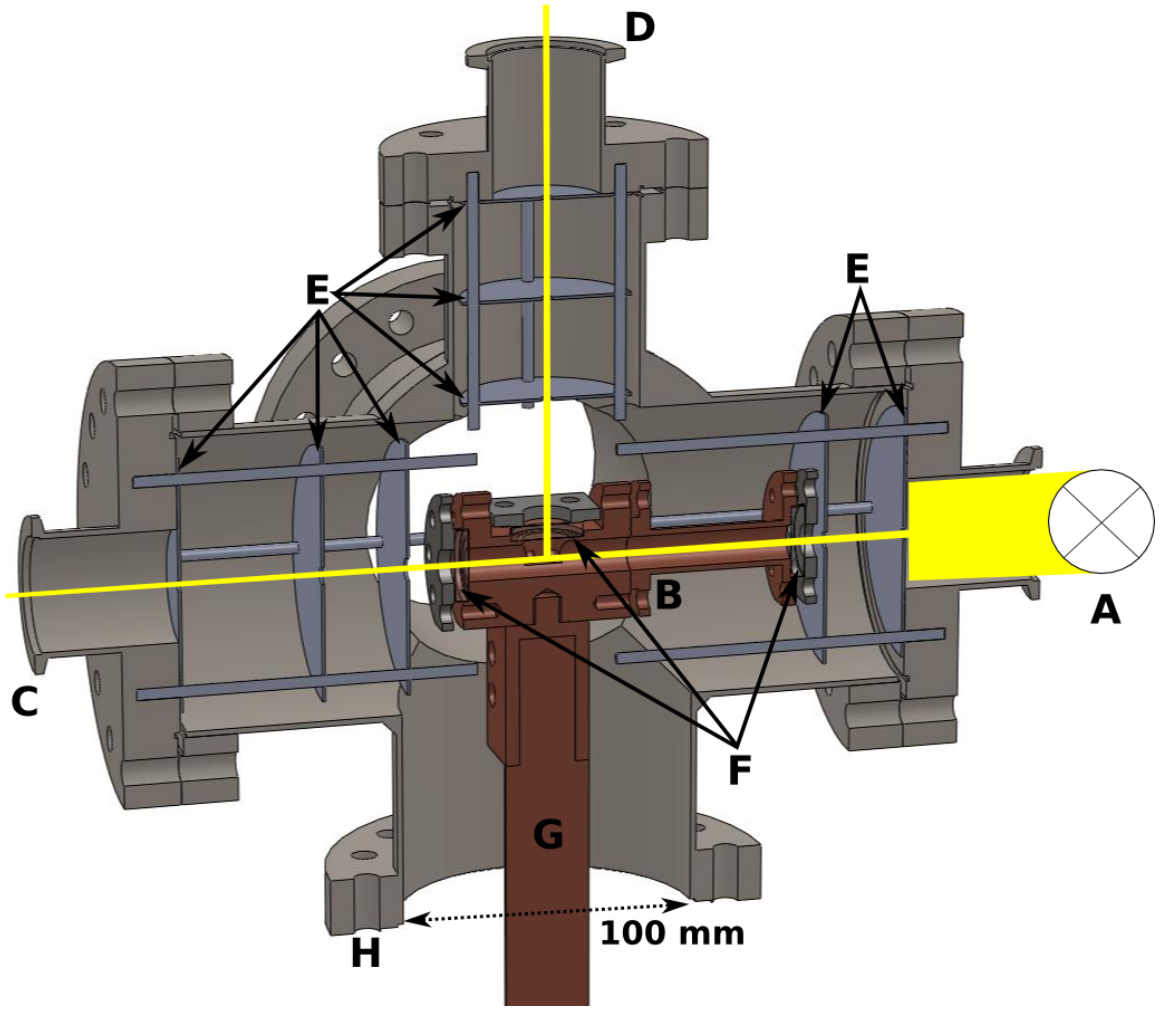

Figure 4.1: *The optical transmission of pure and xenon-doped liquid argon in the vacuum ultraviolet has been measured using a deuterium light source (A, Cathodeon Model V03) which was attached to an evacuated cross piece (CF100) of 100 mm inner diameter (outer cell, H). The light was sent through a cryogenic copper cell (inner cell or sample cell, B) containing the liquid noble gas samples (liquid volume: $\sim 13\,cm^3$) and analyzed with a VUV spectrometer (McPherson 218 monochromator with image intensified diode detector array) attached to flange C. For measuring light scattered at an angle of 90° a VUV photodiode (Opto Diode Corp. model AXUV20A) was attached to flange D at a distance of approximately 17 cm and was read out by a nanoamperemeter. Stray light was avoided by apertures (E) in front of and behind the inner cell and in front of the VUV photodiode. The light entered and exited the inner cell through MgF_2 windows (F). The optical path length the light had to traverse in the liquid noble gas samples was 11.6 cm. The inner cell was connected to a liquid nitrogen dewar via a copper rod (G) for cooling and positioning.*

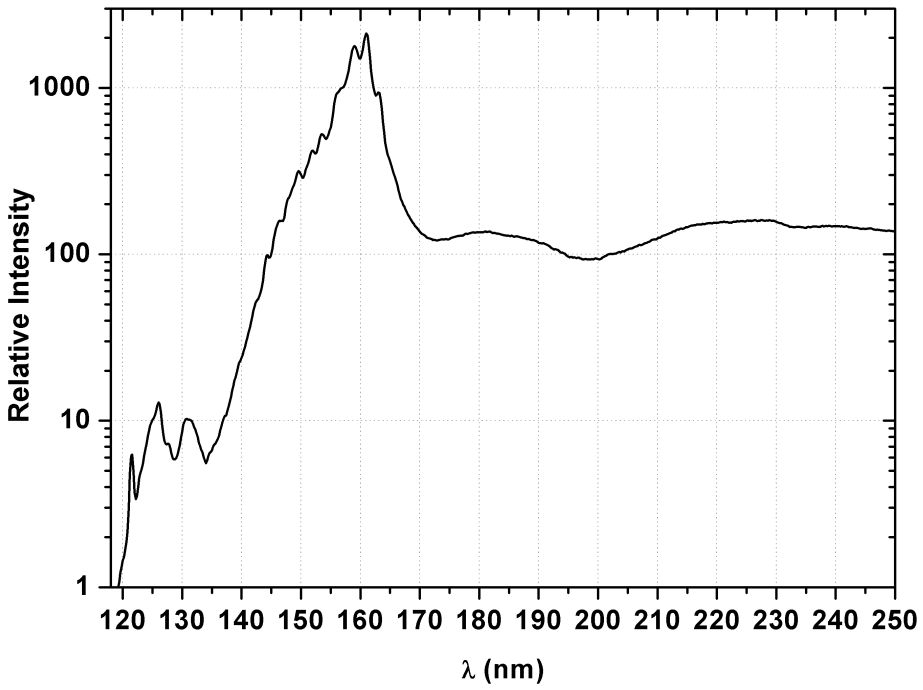

Figure 4.2: *A raw-data emission spectrum of the deuterium arc lamp (Model Cathodeon V03) with MgF_2 window used for the transmission measurements is shown. Note, that the light has to traverse three MgF_2 windows before reaching the detector which leads to a strong reduction of the signal at short wavelengths.*

4.2 Systematic Effects - Transmission values above one

To obtain the wavelength-dependent transmission curves the basic concept was to divide spectra recorded with the filled sample cell by spectra recorded afterwards[2] with the cold evacuated sample cell. Prior to division, the spectra were background and stray-light corrected (for details see ref. [33, 42]). However, three systematic effects could be identified that artificially increase the measured transmissions. These effects are described very detailed in refs. [33, 42, 53] and will be discussed briefly in the next three subsections.

4.2.1 Fresnel Effect

Filling the inner cell with a liquid noble gas sample with a refractive index n > 1 leads to a reduced reflection of light at the surface transitions between MgF_2 window and liquid noble gas sample ("Fresnel Formulas" for normal incidence of light). Hence, more light is transmitted when the cell is filled with a liquid noble gas sample. Consequently a division of spectra recorded with the cell filled by spectra recorded with the evacuated cell leads to an artificially increased transmission. Using the experimental setup depicted in Fig. 4.1, the expected transmission of a fully transparent liquid noble gas sample can be calculated according to eq. 4.4.

$$T_{Fr} = \left(\frac{1 - \left(\frac{n_{MgF_2} - n_{LNG}}{n_{MgF_2} + n_{LNG}} \right)^2}{1 - \left(\frac{n_{Vak} - n_{MgF_2}}{n_{Vak} + n_{MgF_2}} \right)^2} \right)^2 \tag{4.4}$$

$\mathbf{T_{Fr}} = \mathbf{T_{Fr}}(\lambda)$ Wavelength-dependent transmission without any attenuation features due to the "Fresnel effect"

$\mathbf{n_{MgF_2}} = \mathbf{n_{MgF_2}}(\lambda)$ Wavelength-dependent refractive index of magnesiumfluoride

$\mathbf{n_{LNG}} = \mathbf{n_{LNG}}(\lambda)$ Wavelength-dependent refractive index of a liquid noble gas sample

$\mathbf{n_{Vak}} = 1$ Refractive index of vacuum

Data as well as model calculations for the wavelength-dependent refractive index of cryogenic MgF_2 in a wavelength range from 103 to 200 nm are available in ref. [75]. For pure liquid argon and xenon-doped liquid argon no measurements of the wavelength-dependent refractive indices were found in the literature. However, data and model calculations for the wavelength-dependent refractive index of pure

[2]The evaporation of the gas samples and the following evacuation of the inner cell took less time ($\sim$ 30 minutes) than the preparation (e.g. purification and distillation of pure liquid argon) and following condensation ($\sim$ 3 hours) of the gas samples into the inner cell. Therefore, reference spectra were recorded after the spectra with the inner cell filled with the liquid had been measured.

gaseous argon at standard conditions in a wavelength range from 140 to 254 nm are available [74]. An estimate of the refractive index of liquid argon is based on a density scaling from the gas into the liquid phase in analogy to the strategy in ref. [73]. The estimate of the wavelength-dependent refractive index of liquid argon compared to MgF_2 is presented in Fig. 6 in ref. [53] and in Fig. 2.9 of the present thesis. However, for pure liquid argon, it turned out that a "Fresnel correction[3]" of the raw data alone could not explain[4] (non-physical) transmission values above unity measured with the experimental setup in Fig. 4.1. Consequently, at least one further effect artificially increasing the transmission has to be identified.

4.2.2 Finite Divergence of the Light Source

It turned out that a second effect also leads to increased transmission values in the experimental setup shown in Fig. 4.1. A geometrical effect due to a change of the refraction of light at the inner surfaces of the MgF_2 windows when the cell is filled with the liquid also has to be taken into account. In analogy to the "Fresnel effect" also this "finite divergence effect" leads to excessive transmission values. This effect is visualized by the schematic drawing in Fig. 4.3 and acts as if filling the inner cell with a medium with refractive index $n > 1$ leads to a displacement of the light source closer to the detector behind the cell (at a distance z) leading to an increase in intensity. This effect can become very significant when light of finite divergence is used to probe the attenuation. If a point like source is positioned at a distance x from the entrance window of an absorption cell, the light travels more collimated through the cell (length y) when it is filled with a medium with refractive index larger than one. Exiting the cell (filled as well as empty) the light propagates with the same divergence as in front of the cell. However, it has to be mentioned that the integral amount of transmitted light is not affected by the "finite divergence effect". This effect only becomes visible when restricting optical elements (e.g. apertures, or the sensitive area of the detector is smaller than the area of the beam profile) are positioned in the optical path between light source and the sensitive area of a detector. Using a detector with a sensitive area larger than the beam profile would result in the same integral intensity with a more focused beam profile in the case of the filled sample cell.

The expected transmission value can be described according to equation 4.5 which has been derived using the geometrical effect as shown in Fig. 4.3. The impact of the "finite divergence effect" is quantified using the position of the virtual source and the $\left(\frac{r_1}{r_2}\right)^2$ law for the intensity ratio, where r_1 and r_2 are the distances from the detector to the real and virtual source, respectively.

[3] "Fresnel correction" means dividing the measured transmission curve above one by equation 4.4 to obtain transmission values below one.

[4] As an example, at a wavelength of 180 nm a transmission of 6 % above one instead of the measured 20 % (see Fig. 4 in ref. [53]) could be explained using the estimated refractive index of liquid argon.

$$\left(\frac{\mathrm{r}_1}{\mathrm{r}_2}\right)^2 = \left(\frac{x+y+z}{x+\frac{y}{n_{\mathrm{LNG}}}+z}\right)^2 \tag{4.5}$$

$\mathbf{r}_1$ Distance between detector and real source

$\mathbf{r}_2$ Distance between detector and virtual source

x Distance between light source and sample cell

y Length of the sample cell (11.6 cm in the experimental setup in Fig. 4.1)

z Distance between sample cell and detector

$n_{\mathbf{LNG}} = n_{\mathbf{LNG}}(\lambda)$ Wavelength-dependent refractive index of a liquid noble gas sample

It has been shown [53] that the finite thickness of the optical windows of 5 mm can be neglected. The approximation for paraxial rays ($\sin(\alpha) \sim \alpha$, $\sin(\beta) \sim \beta$) shows that the effect does not disappear for that case and is actually independent of the angles.

Here it has to be noted that the finite divergence effect has also been verified[5] in the ultraviolet, visible and near infrared wavelength regions which excludes some uncontrolled behaviour of the experimental setup in the vacuum ultraviolet wavelength region [53]. Furthermore, sending a He-Ne laser beam with a beam divergence of only ~ 0.5 mrad through the sample cell and analyzing the beam intensity as well as the beam profile with a position-sensitive detector with a high spatial resolution allowed to measure the "finite divergence effect" directly. The intensity of the laser beam was measurably enhanced due to the Fresnel and the "finite divergence effect" and the beam profile was measurably narrowed when the sample cell was filled with pure liquid argon compared to the evacuated sample cell [53].

However, also a combination[6] of the corrections for the "Fresnel" and the "finite divergence effect" could not scale the measured transmission of pure liquid argon into the physical reasonable region below one. In addition, one further systematic effect has been discovered which also leads to excessive transmission values. This effect is called "fogging-effect" and is described in the next subsection.

4.2.3 "Fogging" of the MgF_2 Windows

The transmission measurements performed with the experimental setup depicted in Fig. 4.1 rely on a time-invariant transmission of the cryogenic MgF_2 windows in the optical path. In particular, this requirement is a stringent condition during the time interval between measurement of the spectrum with a filled sample cell and

[5] Decreasing source distances x lead to increasing transmission values.

[6] Combination means a division of the measured transmission spectrum of pure liquid argon by the product of equations 4.4 and 4.5 to correct the spectrum for the "Fresnel effect" and the "finite divergence effect".

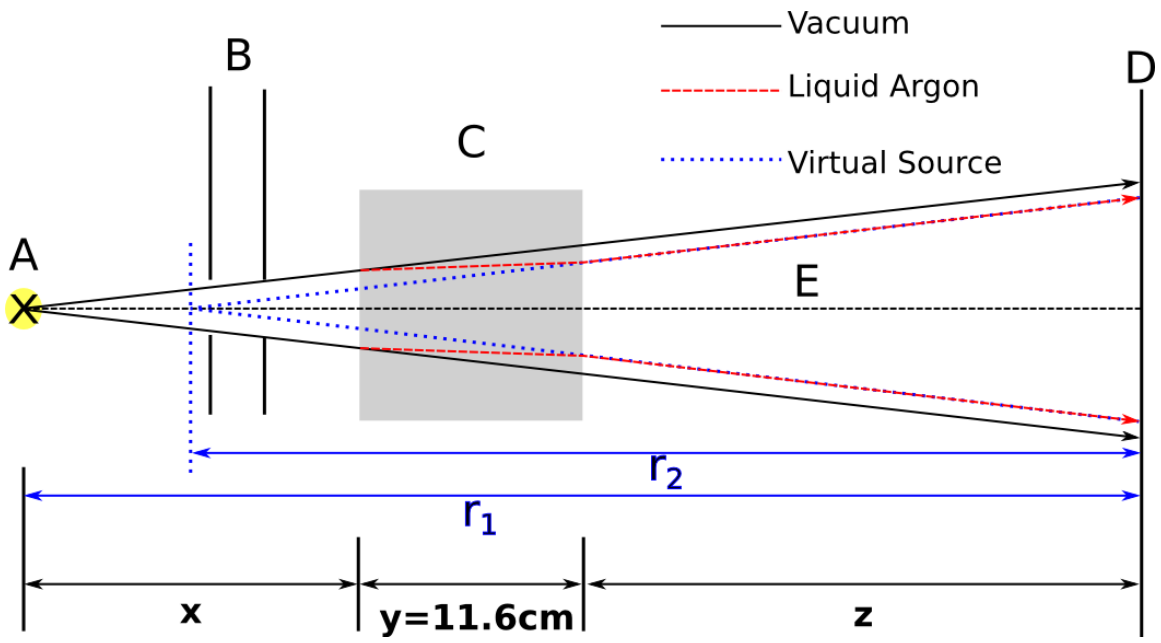

Figure 4.3: *A simplified schematic drawing of the experimental setup (see Fig. 4.1) without MgF_2 windows is shown. The drawing describes the influence of a light source (A) with finite divergence at a distance r_1 from the detector plane (D). The apertures (B) had a diameter of 4 mm and led to a divergent beam profile through the sample cell (C). The black solid arrows indicate the beam profile when the sample cell is evacuated and the red dashed arrows indicate the beam profile when the sample cell is filled with a medium with a refractive index larger than one (e.g. liquid argon or xenon-doped liquid argon). The narrowed beam profile leads to a higher intensity at the detector plane (D) when the sample cell is filled. The narrowing of the beam profile can be treated in analogy to a virtual source on the optical axis (E) which has been moved from an initial source distance r_1 to a new virtual source distance r_2 closer to the detector plane. The impact on the measured transmission is an increased intensity at the detector plane by a factor of $\left(\frac{r_1}{r_2}\right)^2$ when the cell is filled with a sample. x,y and z describe the distances which are used in equation 4.5. In the case of the deuterium source the distances were x=17.5 cm, y=11.6 cm and z=36.5 cm. The other light sources (halogen lamp, He-Ne laser) used and the corresponding distances probed are summarized in table 2 in ref. [53].*

measurement of the corresponding reference spectrum with an evacuated sample cell, afterwards. In the following the spectrum measured with the filled sample cell will be called "measurement spectrum" and the spectrum measured with the evacuated sample cell will be called "reference spectrum".

It turned out that the cryogenic sample cell and consequently also the cryogenic MgF_2 windows act as a cold trap within the evacuted outer cell (H in Fig. 4.1). The pressure in the outer cell, when the inner cell was at room temperature, was typically $\sim 8 \cdot 10^{-6}$ mbar and decreased during the cooling-down of the inner cell to a value of

typically $\sim 7 \cdot 10^{-7}$ mbar when the inner cell was filled with a liquid noble-gas sample.

Therefore, a measurement campaign was initiated to test whether the transmission of the cryogenic MgF_2 windows is dependent on the time of the sample cell being cold. A reference spectrum was recorded when the evacuated sample cell was at room temperature. Then, a clock was started when liquid nitrogen was filled into the dewar to start the cooling-down process. In time intervals of 30 minutes spectra were recorded and transmission spectra at different times relative to the cooling-down of the inner cell were calculated.

The results are presented wavelength resolved in Fig. 4.4 and time resolved for a set of selected wavelengths in Fig. 4.5. The spectra clearly demonstrate that the transmission decreases with time being cold. The strong absorption minimum in Fig. 4.4 at 142 nm center wavelength can be attributed to an absorption band of ice which is formed due to condensation of rest-gas components (presumably water vapor frozen to ice) onto the outer MgF_2 surfaces. Water frozen to ice (dependent on the substrate temperature) is known to have strong absorption bands in the VUV [96, 97].

When the sample cell was filled with a liquid noble gas sample (i.e. pure liquid argon or xenon-doped liquid argon) the measurment spectrum has been recorded typically two hours and the corresponding reference spectrum typically three hours after filling the dewar with liquid nitrogen. Recording a spectrum typically took 6 minutes. The decreasing transmission between measurement and reference spectrum due to the "fogging effect" leads to an artificially decreased reference spectrum and, thus, to an artificially increased transmission spectrum. The recording time relative to filling the dewar with liquid nitrogen was documented for every spectrum and the fit values obtained from Fig. 4.5 were used to correct the excessive transmission values due to the "fogging effect" at each wavelength position (for details see refs. [33, 53]). This correction is extremely reliable for wavelengths longer than 160 nm. Below 160 nm an additional systematic error of the order of 5 % is introduced [53] in the transmission spectra of pure and xenon-doped liquid argon, respectively (see the error bars in Figs. 4.6 and 4.7).

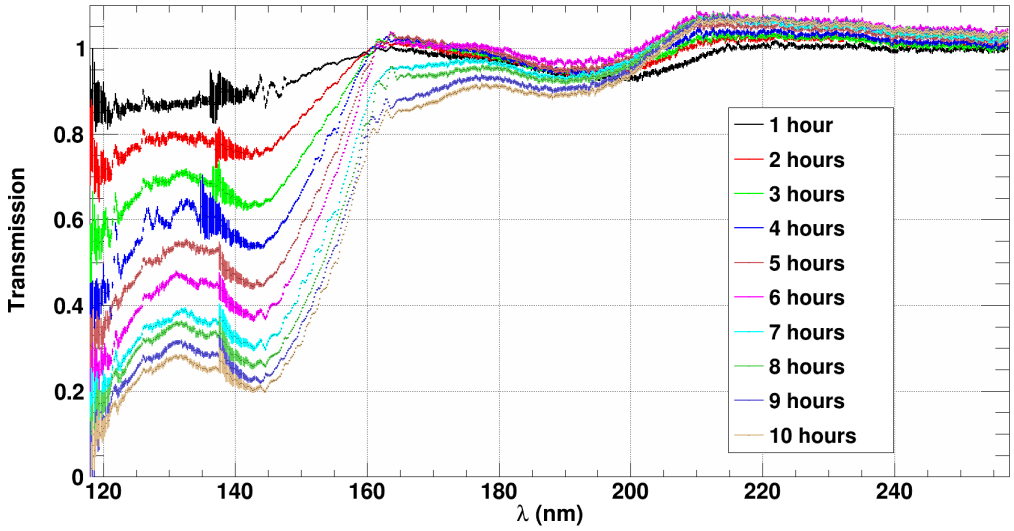

Figure 4.4: *The transmission curves of the cooled and evacuated sample cell after different times relative to filling the dewar with liquid nitrogen are shown. The reference spectrum has been recorded when the sample cell was at room temperature. Every 30 minutes a spectrum has been recorded and the transmission has been calculated. For reasons of clarity only transmission spectra measured after full hours are presented. In the measurements the temperature of liquid argon is reached after about two hours. Below 160 nm the drop of the transmission is severe which can be attributed to the formation of ice from water vapor frozen onto the outer MgF_2 window surfaces. Water frozen to ice (dependent on the substrate temperature) can have strong absorption bands in the VUV [96, 97]. This shows that the sample cell basically acts as a cold trap for rest-gas components in the evacuated outer cell. Note the enhanced transmission values above 210 nm. Two possible explanations are considered: The coating of the cryogenic MgF_2 windows could lead to a layer which has a refractive index between one and that of MgF_2 which leads to an enhanced transmission (optical coating). A second tentative explanation could be resonance fluorescence of the components frozen to the cold MgF_2 windows. This figure is adapted from ref. [53].*

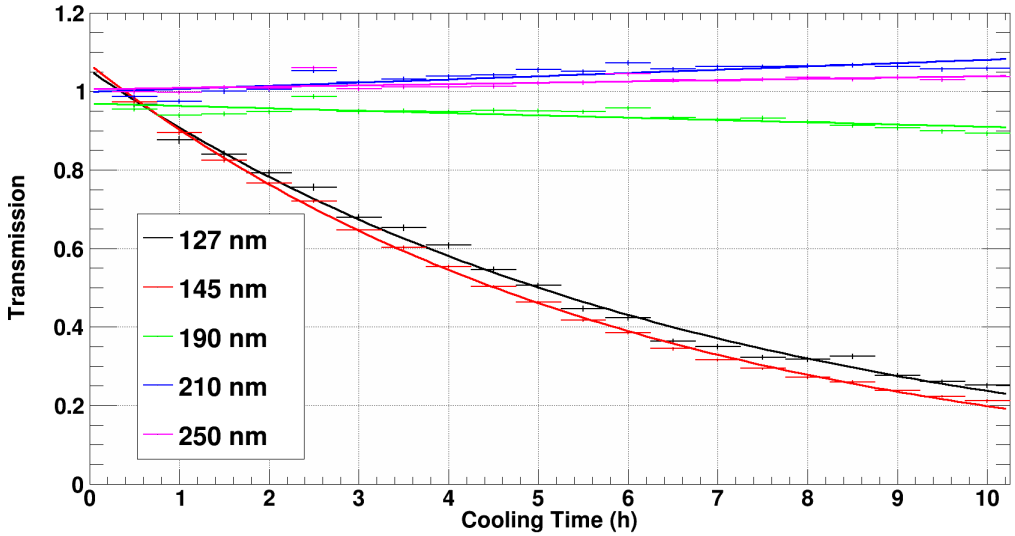

Figure 4.5: *The time evolution of the transmission depicted in Fig. 4.4 is shown for a set of selected wavelengths in steps of 30 minutes. A wavelength-resolved correction of the "fogging effect" has to rely on a precise knowledge of the time-dependent wavelength-resolved transmission of the cold MgF_2 windows. The solid lines show exponential fits to the time evolution of the transmission of the evacuated and cold sample cell. The results obtained from these fits were used to correct the measured transmission spectra of pure and xenon-doped liquid argon for this effect at each wavelength position. Note that here only a set of selected wavelengths is shown. The exponential fits have been performed for every wavelength shown in Fig. 4.4. This figure is adapted from ref. [53].*

4.3 Optical Transmission of 11.6 cm pure Liquid Argon in the VUV

The main goal of this chapter is to provide an attenuation length of pure liquid argon for its own scintillation light. Therefore, the undisturbed transmission spectrum of a sample of pure liquid argon has to be recorded in a wavelength region where pure liquid argon scintillates. Due to the identification of several systematic issues described above ("Fresnel effect","finite divergence effect" and "fogging effect") a transmission spectrum of 11.6 cm pure liquid argon (measured with a deuterium light source) corrected for all the above-mentioned effects is presented in the upper panel of Fig. 4.6. Note that the thickness of the measured transmission curve is caused by error bars and not by signal fluctuations. The error bars are a sum of two components: Firstly, the statistical errors from the intensity and the exposure times of the deuterium light source, secondly, the systematic errors from the "fogging correction" which leads to increasing error bars below 160 nm.

The first major result is that the decreased transmission towards shorter wavelengths in Fig. 6 in ref. [33] was caused by a residual xenon impurity and not by liquid argon itself. The length of the sample cell has been doubled in the present thesis compared to ref. [33] which leads to a higher sensitivity. If the decreasing transmission towards the short-wavelength end of the setup would be an intrinsic feature of pure liquid argon, this effect is expected to be strongly enhanced. However, this is not observed and, thus, demonstrates that the distillation procedure removed xenon from argon so efficiently that no[7] xenon-related absorption features can be identified.

Above $\sim$ 160 nm the transmission is still 4 % too high which could be a hint to a still unresolved systematic effect. However, it has to be emphasized that the systematic corrections described above ("Fresnel effect" and "finite divergence effect") rely on the wavelength-dependent refractive index of pure liquid argon which has not yet been measured. A density scaling from the gas into the liquid phase seems reasonable but below 140 nm not even data about the refractive index of gaseous argon (see ref. [74]) are available. That means below 140 nm the refractive index of liquid argon is based on wavelength-extrapolated values from the gas phase. Since the scintillation of liquid argon peaks at $\sim$ 127 nm (see lower panel in Fig. 4.6) no measured information about the refractive index of argon in the gas as well as in the liquid phase is available at these wavelengths. An estimate of the actual impact of the refractive index on the transmission data presented in the upper panel of Fig. 4.6 has been performed at an example wavelength of 200 nm [53]. It turned out that a 12 % relative variation of the refractive index of liquid argon can scale the transmission to a physically reasonable value of one at a wavelength of 200 nm.

However, it has to be noted that liquid argon must have a high[8] transparency for its own scintillation light: The systematic effects described above were only discovered

[7] On the current level of sensitivity with a length of the sample cell of 11.6 cm.

[8] The transparency must be so high that systematic effects shifting the transmission above one must have a higher impact than real attenuation effects shifting the measured transmission to lower values.

due to the measured transmission being above one. In any other case where the transmission is below one (e.g. due to a longer sample cell, or intrinsic absorption features) it is difficult to identifiy these systematic effects since the impact of these effects and real attenuation are difficult to disentangle.

The red curve in the upper panel of Fig. 4.6 shows the expected transmission of a 11.6 cm long liquid argon sample according to a Rayleigh scattering length of 90 cm at 128 nm [98]. The measurement indicates a slightly decreasing trend towards the short-wavelength end of the spectrum as may be the case due to Rayleigh scattering. However, even a scaling of the transmission curve to values of one for wavelengths longer than 160 nm indicates a Rayleigh scattering longer than 90 cm. The black asterisk at 128 nm in the upper panel of Fig. 4.6 shows the expected transmission (of 11.6 cm liquid argon) for an attenuation length of 66 ± 3 cm at 128 nm measured by Ishida et al. [92]. The wavelength-resolved transmission spectrum shown in Fig. 4.6 indicates a longer attenuation length with a lower limit of ~ 1.10 m (see discussion below).

Due to the lack of information on the wavelength-dependent refractive index of pure liquid argon it is difficult to give a reliable statement on the attenuation length based on a 11.6 cm long sample used in the present experiment. Therefore, a Rayleigh scattering length of 90 cm can neither be confirmed nor excluded as long as no measured values for the wavelength-dependent refractive index of liquid argon are available. However, a very conservative approach based on the lower limits of the error bars in the upper panel of Fig. 4.6 can be used to give a lower limit for the attenuation length. The scintillating region of pure liquid argon (see lower panel in Fig. 4.6) is between 122 and 135 nm. In this wavelength region a transmission better than ~ 0.9 has been measured even if the transmission curve is scaled to match one for wavelengths longer than 160 nm. Consequently, with a length of the sample cell of 11.6 cm a lower limit of ~ 1.10 m [53] for the attenuation length can be calculated.

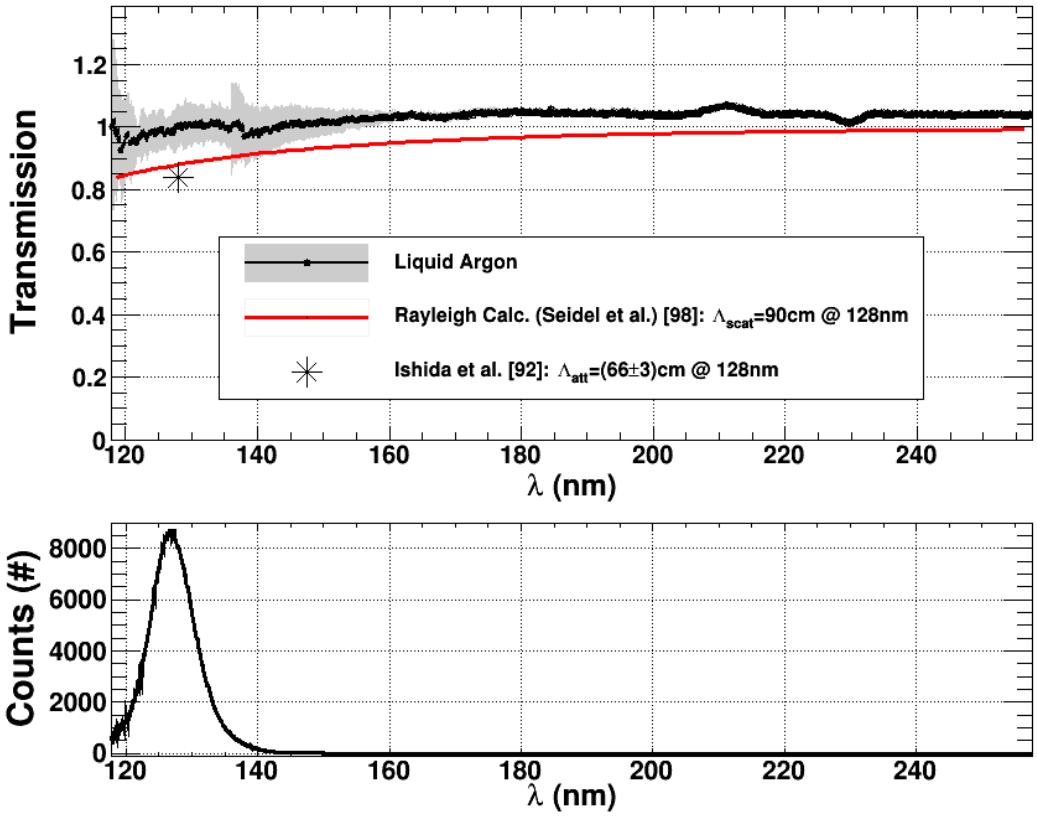

Figure 4.6: *Upper panel: The transmission of 11.6 cm pure liquid argon is shown (black curve with grey error bars). On the current level of sensitivity no xenon-related absorption effects could be identified and pure liquid argon is fully transparent down to the short-wavelength cut-off of the system at 118 nm. Note that above 160 nm the transmission is still* ~ 4 *% too high (for explanations see text). The red line shows the expected transmission of a sample of 11.6 cm pure liquid argon according to a value of a Rayleigh scattering length of 90 cm at 128 nm (*$\Lambda_{scat} = 90$ *cm at 128 nm) [98]. The black asterisk shows, for comparison, the expected transmission value of 11.6 cm pure liquid argon for an attenuation length of* (66 ± 3) *cm at 128 nm (*$\Lambda_{att} = (66 \pm 3)$ *cm at 128 nm) adapted from ref. [92]. The lower panel shows, for comparison, the electron-beam induced emission of pure liquid argon (adapted from ref. [44]).*

4.4 Optical Transmission of 11.6 cm Xenon-doped Liquid Argon in the VUV

The investigation of the optical transmission spectrum of xenon-doped liquid argon in the VUV is interesting for three reasons:

Firstly, in ref. [33] xenon has been identified as a critical impurity for pure liquid-argon particle-detectors. However, the actual xenon concentration in those experiments could only be estimated since no transmission measurements were performed where xenon was added deliberately to the liquid argon samples. Adding xenon deliberately to pure liquid argon and measuring the transmission spectrum of a sample with a certain optical path length provides a scale for the purity[9] which has to be achieved in pure liquid-argon particle-detectors in order to avoid too much absorption of scintillation light due to xenon.

Secondly, transmission measurements in xenon-doped liquid argon provide complementary information to the electron-beam induced emission spectra presented in Figs. 3.2 and 3.3. This complementary information could be useful in the assignment of the species which is responsible for the recently discovered intense near-infrared scintillation in xenon-doped liquid argon (see Fig. 3.4). So far no assignment was possible and a tentative attempt for an assignment will be presented in the next chapter.

Thirdly, if it turns out that xenon-doped liquid argon is a suitable scintillator material for future particle detectors, a transmission spectrum in the VUV provides information about the attenuation of scintillation light in the VUV. Due to the above-mentioned general trend towards increasing detector volumes in rare-event physics, the attenuation length of a scintillator for its own scintillation light is a critical parameter when large detector volumes are involved.

Fig. 4.7 shows the measured transmission spectra of 11.6 cm liquid argon doped with xenon concentrations varied by factors of 10 from 0.1 ppm to 1000 ppm. The measurements were performed using the experimental setup depicted in Fig. 4.1. The preparation of the gas samples has been performed in exactly the same way as already explained in section 3.2. In the transmission measurements $\sim 35\,\%$ of the initial gas volume is condensed into the sample cell. This corresponds to a maximum deviation of the xenon concentration in the liquid sample by a factor of ~ 2.8 if all the xenon is condensed out of the buffer volume into the cryogenic sample cell (see section 3.2 for details). All the xenon concentrations stated below refer to the gas phase at room temperature when the argon-xenon mixtures were prepared. Here it has to be noted that the transmission spectra were corrected only for the "fogging effect" (see section 4.2). Due to the lack of information about the wavelength-dependent refractive index of xenon-doped liquid argon it is not possible to correct the transmission spectra for the "Fresnel effect" and the "finite divergence effect". Therefore, the transmission spectra presented in Fig. 4.7 are scaled to a value of ~ 1 for a wavelength of 160 nm where no absorption features related to xenon were measured. The slightly decreasing

[9] An upper limit for xenon in pure liquid argon.

transmission values for wavelengths larger than 160 nm could be related to refractive index issues since an analogue feature has been observed in the raw data of the transmission of pure liquid argon (see Fig. 4 in ref. [53]).

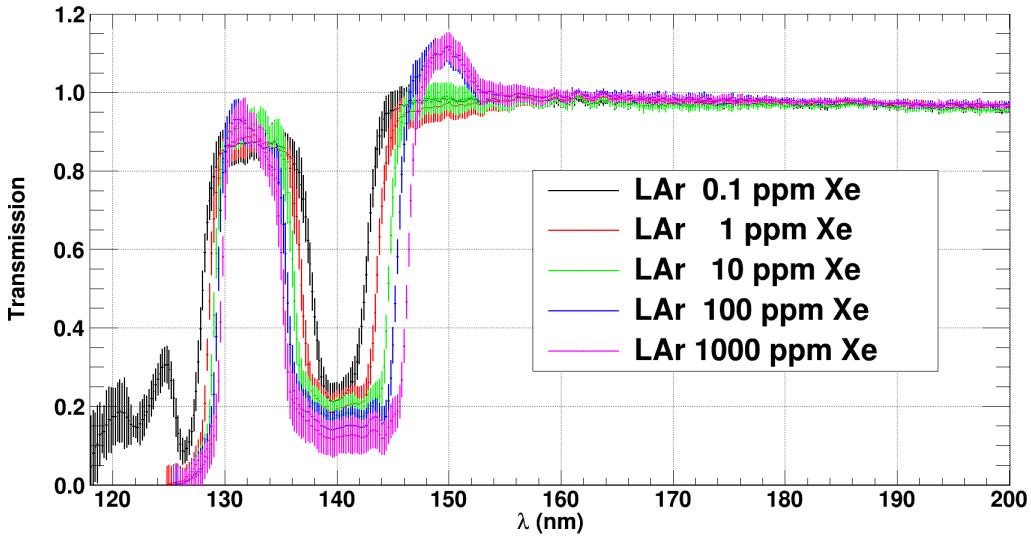

Figure 4.7: *The transmission of 11.6 cm liquid argon doped with different amounts of xenon is presented. The xenon concentrations have been increased by factors of 10 from 0.1 ppm to 1000 ppm. The most prominent absorption band at 140 nm broadens with increasing xenon concentration. For a xenon concentration above 0.1 ppm the mixture is not transparent below 130 nm for a length of the optical path of 11.6 cm. Three different absorption bands related to xenon can be identified in liquid argon doped with 0.1 ppm xenon. The center wavelengths of the transmission minima are at 122.2 nm and 140.0 nm and can be attributed to perturbed* $^1P_1$ *(n=1,* $^2P_{\frac{1}{2}}$*) and* $^3P_1$ *(n=1,* $^2P_{\frac{3}{2}}$*) atomic xenon states [82]. The third transmission minimum is centered at 126.5 nm and can be attributed to a trapped exciton (Wannier-Mott) impurity state [82]. The transmission values above one at* ~ 150 *nm for the 100 ppm and 1000 ppm mixtures are attributed to resonance flourescence (details see text). This emission feature is also visible in the electron beam induced emission spectra of these mixtures (see Figs 3.2 and 3.3). This figure is adapted from ref. [94].*

Xenon-doped liquid argon shows strong xenon-related absorption features. The most prominent absorption band is centered at 140 nm and broadens with increasing xenon concentration. In the transmission spectrum of liquid argon doped with 0.1 ppm xenon (black line in Fig. 4.7) three different absorption bands can be identified. The center wavelengths of the transmission minima are at 122.2 and 140.0 nm and can be attributed to perturbed ($\sim$ 7 nm blue shifted) $^1P_1$ (n=1, $^2P_{\frac{1}{2}}$) and $^3P_1$ (n=1, $^2P_{\frac{3}{2}}$) atomic xenon states [82]. The third transmission minimum is centered at 126.5 nm an can be attributed to a n=2 ($^2P_{\frac{3}{2}}$) trapped exciton (Wannier-Mott) impurity state [82] which has no parentage in the states of isolated xenon atoms.

Increasing the xenon concentration leads to a broadening of the 140 nm absorption band. The 126.5 nm absorption band becomes completely opaque below 130 nm for xenon concentrations higher than 0.1 ppm and an optical path length of 11.6 cm.

Both, the 100 and the 1000 ppm xenon in liquid argon mixtures show a transmission above one which peaks at a wavelength of approximately 150 nm. The mixtures investigated here in transmission have also been studied wavelength resolved in emission by electron-beam excitation (see Figs. 3.2 and 3.3). Emission features which depend on the concentration of xenon in liquid argon can be observed at these wavelengths. Therefore, these transmission features above one are tentatively attributed to resonance fluorescence. The results of the measurement of the scattered light with the photodiode lead to the conclusion that the emission was too weak to be detected with the AXUV diode. So far, however, further unknown systematic effects responsible for the transmission features at 150 nm cannot be be excluded completely.

To quantify the optical influence of xenon in liquid argon the area of the transmission minimum at 140 nm has been calculated for all five measured xenon-concentrations. The result is presented in Fig. 4.8 (black dots) and has been obtained from integrating the spectra shown in Fig. 4.7 from 132 nm to 147 nm according to equation 4.6:

$$A_{140\,nm} = \int_{132\,nm}^{147\,nm} (1 - T(\lambda))d\lambda \tag{4.6}$$

$A_{140\,nm}$ Area or equivalent width of the transmission minimum at 140 nm center wavelength

$T(\lambda)$ Measured transmission in Fig. 4.7

The equivalent width of the xenon-related absorption feature is descriptively explained as follows: The xenon-related absorption feature has a certain concentration-dependent area. The equivalent width of this absorption feature is the width which would be necessary to form a rectangular absorption feature with the same area which drops to zero transmission.

The areas of the transmission minima show a logarithmic trend with increasing xenon concentration in liquid argon and can be treated in analogy to equivalent widths. In astrophysics, equivalent widths of absorption lines from atmospheres of stars are used to derive information about the concentration of the corresponding element in the stellar atmosphere. Here, the area of the transmission minimum at 140 nm provides information for the determination of the xenon concentration in liquid argon. If wavelength-resolved information on the transmission of liquid argon deliberately doped (or contaminated in the case of pure liquid argon) with xenon is available, the xenon concentration can be estimated using the calibration curve presented in Fig. 4.8. The x-axis in Fig. 4.8 shows the so-called column density which is the concentration of xenon atoms times the optical path length (11.6 cm in the present setup).

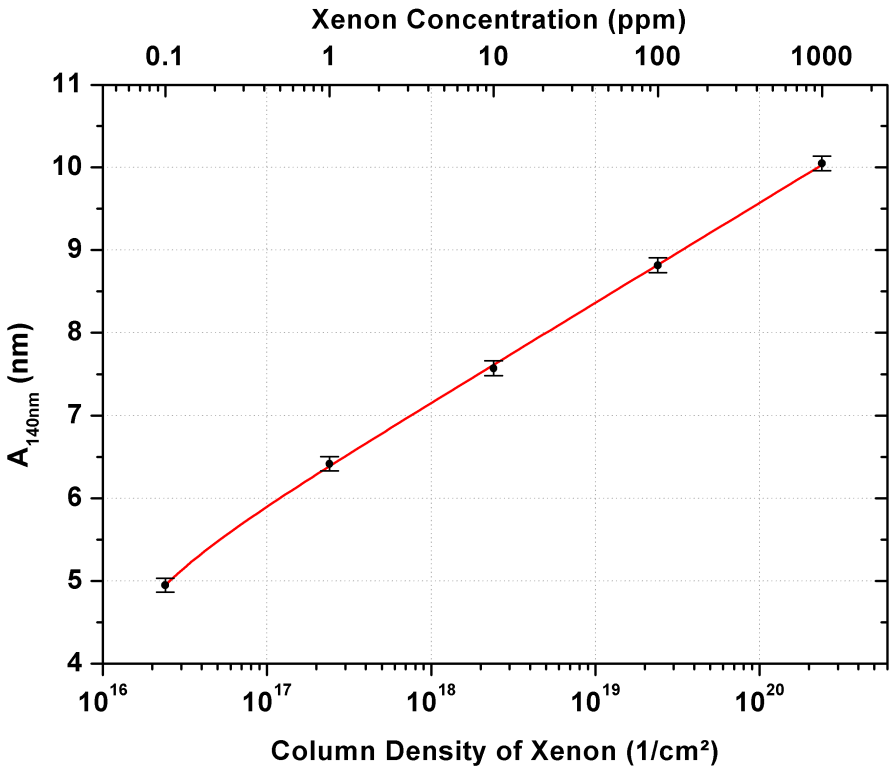

Figure 4.8: *The equivalent widths of the 140 nm transmission minima from Fig. 4.7 for liquid argon doped with 0.1 ppm to 1000 ppm xenon are presented (black dots). The integration was performed from 132 nm to 147 nm according to equation 4.6. The y-axis shows the equivalent width ($A_{140\,nm}$) and the lower x-axis the so-called column density of xenon atoms in liquid argon. The column density is the density of xenon atoms times the optical path length (here 11.6 cm). The upper x-axis shows, for comparison, the corresponding xenon concentrations when the argon-xenon mixtures were prepared. The data points are fitted with a natural logarithmic function represented by the red line:* $y = a - b \cdot \ln(x + c)$.
The best-fit parameters have been determined as:
$a = -14.6 \pm 0.4, b = -0.525 \pm 0.008, c = -(9 \pm 2) \cdot 10^{15}$. *This figure is adapted from ref. [94].*

Chapter 5

Discussion of the Results and Motivation for Future Experiments

So far, no unambiguous identification of the near-infrared emitting species in xenon-doped liquid argon was possible. However, from a spectroscopic point of view an assignment would be important. Furthermore, a deeper understanding of the processes leading to the formation of the intense near-infrared emission could create the possibility to enhance the light output when certain parameters are optimized. In addition, predictions and interpretations concerning the projectile dependence of the near-infrared emission can be deduced if the formation and light-emitting processes are identified. Therefore, a tentative approach to an assignment of the near-infrared emitting species is presented in the following section.

5.1 A Tentative Assignment of the Intense Near-Infrared Emission in Xenon-doped Liquid Argon

From experiments with pulsed electric discharges in xenon-doped (10 ppm - 1000 ppm) gaseous argon it is known that xenon acts as a very efficient electronic energy acceptor in argon-xenon mixtures [99]. At these low xenon concentrations (< 1000 ppm) the direct excitation of xenon atoms in argon-xenon mixtures can be neglected. Therefore, the modification of the emission spectra in the vacuum ultraviolet wavelength region is assigned to energy transfer processes from argon to xenon. Two efficient energy transfer mechanisms were identified in ref. [99] and will be explained briefly in Fig. 5.1:

Firstly, due to the close coincidence between the 9d (J=1, J=2) levels of pure xenon and the ($^1P_1$) state of pure argon, large energy-transfer cross-sections have been measured ($\sigma \sim 10^{-14}\,\mathrm{cm}^2$ [99]). This energy transfer mechansim is illustrated by the horizontal black arrows in the upper part of Fig. 5.1. Secondly, due to the overlap between the energy released by the decay of argon excimers (second excimer continuum of pure argon) and the $^1P_1$ state of pure xenon also an energy transfer from argon excimers to xenon atoms in the ground state is possible which are then

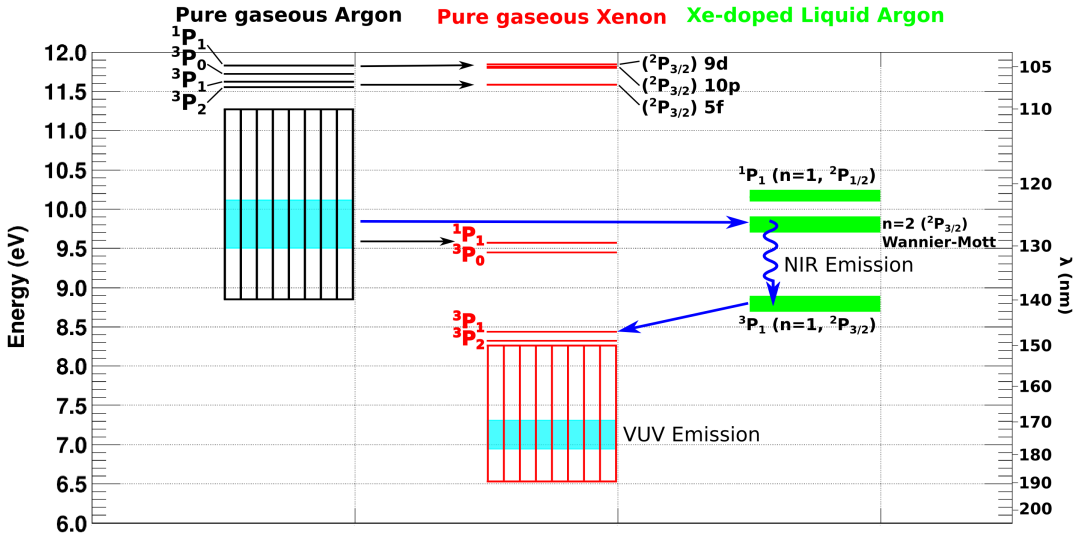

Figure 5.1: *The lower atomic levels and the energy released in molecular emissions, respectively, of pure gaseous argon (black), pure gaseous xenon (red), and xenon-doped liquid argon (green) are shown. The atomic levels are adapted from [50]. The left ordinate shows the energy in eV and the right ordinate shows the corresponding wavelength in nm. The vertically shaded areas denote the energy regions where the second excimer continua of pure gaseous argon and pure gaseous xenon are located. The blue regions in the vertically shaded areas denote the peak emission wavelengths with full width at half maximum of the corresponding excimer emissions. The green bands correspond to the energy levels where strong xenon-related absorption features have been measured. The absorption features can be seen as transmission minima in xenon-doped liquid argon in Fig. 5.2. The identification of the different states in xenon-doped liquid argon is adapted from [82]. The blue arrows indicate energy transfer and emission processes which could explain the observed near-infrared and VUV emission in xenon-doped liquid argon. The newly found near-infrared emission is tentatively assigned to a transition from a n=2 ($^2P_{\frac{3}{2}}$) Wannier-Mott impurity state to a perturbed $^3P_1$ (n=1, $^2P_{\frac{3}{2}}$) state of xenon. The thick green lines in xenon-doped liquid argon rather represent band structures in disordered systems than atomic transitions in gases. This figure is adapted from ref. [94].*

excited to the $^1P_1$ state. According to ref. [99] the following reaction is proposed:

$$Ar_2\left(^{1,3}\Sigma_u\right) + Xe\left(^1S_0\right) \rightarrow 2Ar\left(^1S_0\right) + Xe\left(^1P_1\right) \tag{5.1}$$

This energy transfer mechanism is illustrated in Fig. 5.1 by the horizontal black arrow from the energy released by decaying argon excimers[1] to the $^1P_1$ state of pure xenon. Large energy transfer cross-sections of the order of $10^{-14}\,\mathrm{cm}^2$ have been mea-

[1] $Ar_2\left(^{1,3}\Sigma_u\right)$ mean excimers in pure argon which are formed either in singlet or triplet states (see chapter 1.4).

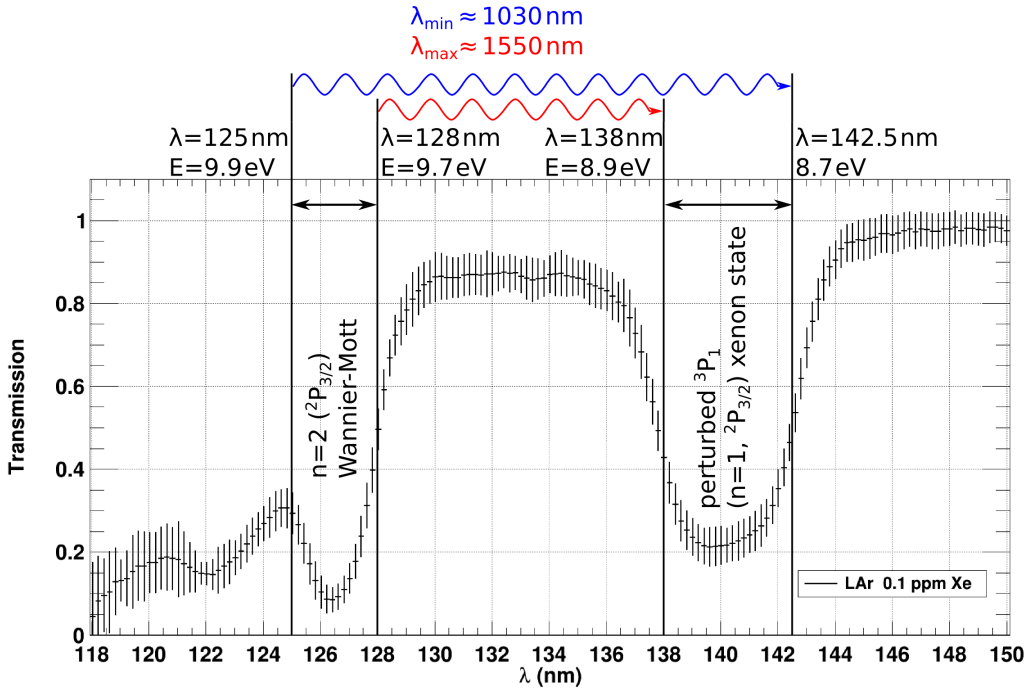

Figure 5.2: *The optical transmission in the VUV of a sample of xenon-doped (0.1 ppm) liquid argon with an optical path length of 11.6 cm is shown. The transmission spectrum is a zoomed view adapted from Fig. 4.7. Two strong xenon-related absorption features are visible which can be attributed to a n=2 ($^2P_{\frac{3}{2}}$) Wannier-Mott impurity state and a perturbed $^3P_1$ (n=1, $^2P_{\frac{3}{2}}$) state of xenon [82]. The vertical lines indicate wavelength regions with strong absorption. The transition which is assumed to be responsible for the newly found near-infrared emission (see, e.g. Fig. 1.8) is indicated by the curly arrows in the upper part. The energy differences between the absorption features could explain a near-infrared emission in the wavelength region from 1030 to 1550 nm. This wavelength region coincides almost exactly with the measured wavelength region (from 1100 to 1550 nm).*

sured for reaction 5.1 [99]. Consequently, in xenon-doped gaseous argon two energy transfer-processes which have high and comparable energy transfer cross-sections lead to an efficient energy transfer from argon to xenon. This is a unique feature of argon-xenon mixtures which is absent in argon-krypton mixtures [99].

In analogy to the arguments stated above an energy transfer from argon to xenon is also proposed in liquefied xenon-doped argon. However, it has to be emphasized that the following model is just an attempt for an assignment of the near-infrared emitting species and no final conclusion. Further experiments will be proposed (see section 5.2) and have to be performed to obtain a conclusive result.

As the density increases from the gas phase to the liquid phase, the discrete level scheme of isolated atoms is changed to band structures in a disordered insulator. This is also visible in the transmission of xenon-doped liquid argon (see Fig. 5.2) since the transmission minima in the vacuum ultraviolet wavelength region are rather broad

absorption features than discrete atomic absorption lines. It is known from literature that the lowest excitation energy of the solid state of a noble gas is only slightly shifted from free-atom excitation [47]. This has also been confirmed in the liquid phase due to the transmission minimum centered at 140 nm in Fig. 5.2 which has the lowest excitation energy. This absorption feature is assigned to a perturbed $^3P_1$ (n=1, $^2P_{\frac{3}{2}}$) atomic xenon state which is only shifted by $\sim$ 0.5 eV (7 nm blue shifted) towards higher energies compared to the undisturbed isolated xenon atom [82]. However, the band structures above the first excited state in xenon-doped liquid argon are significantly changed compared to the isolated xenon atom due to the surrounding argon atoms. The formation of a trapped exciton (n=2, $^2P_{\frac{3}{2}}$, Wannier-Mott) impurity state [82] of xenon in liquid argon is a unique feature of the liquid and solid phase and has no parentage in pure gaseous xenon. This Wannier-Mott impurity state can be treated in a hydrogenic approximation with an electron effective mass $m^* = 0.5 \cdot m_e$ where m_e denotes the free electron mass [82]. The size of the n=2 Wannier-Mott orbital is $\sim$ 0.6 nm in liquid as well as in solid xenon-doped argon and overlaps $\sim$ 40 atomic sites [82].

A transition with an energy difference of $\sim$1 eV between the Wannier-Mott (n=2, $^2P_{\frac{3}{2}}$) impurity state in xenon-doped liquid argon and the perturbed $^3P_1$ (n=1, $^2P_{\frac{3}{2}}$) atomic xenon state could explain the intense near-infrared emission (see Fig. 5.1 and the red and blue arrows in Fig. 5.2). Fig. 5.2 shows the transmission of a sample of liquid argon doped with 0.1 ppm xenon. The length of the optical path was 11.6 cm. This concentration was chosen as representative since it was the only concentration with the current optical path length of 11.6 cm which allowed to observe both, the (n=2, $^2P_{\frac{3}{2}}$) Wannier-Mott as well as the perturbed $^3P_1$ (n=1, $^2P_{\frac{3}{2}}$) atomic xenon state in absorption. A transition between the regions of strong absorption could explain emitted wavelengths from $\sim$ 1030 nm to $\sim$ 1550 nm which coincide almost perfectly with the measured wavelength region ($\sim$ 1100 nm - $\sim$ 1550 nm, see Fig. 1.8, upper panel). At the moment no conclusive assumption can be given whether further xenon atoms in the ground state are involved forming an excimer-like potential with xenon atoms in the Wannier-Mott impurity state. This indeed could explain the continuum character of the near-infrared emission. However, a comparison of the relative variation of the integrated near-infrared signal (green triangles in Fig. 3.13) for xenon concentrations of 0.1, 1 and 10 ppm in liquid argon leads to the conclusion that the trend can be described by an initially linearly increasing signal with xenon concentration followed by a beginning saturation. A quadratically increasing signal seems unlikely since the variation of the near-infrared signal is too low. Therefore, a light-emission process where two xenon atoms are involved seems unlikely since a quadratically increasing near-infrared signal with xenon concentration would be expected. Consequently, the band structure alone could also be responsible for the continuous character of the near-infrared emission. For the formation of the Wannier-Mott impurity states in xenon-doped liquid argon the following energy transfer reaction in analogy to reaction 5.1 is proposed:

$$Ar_2\left(^{1,3}\Sigma_u\right) + Xe\left(^1S_0\right) \rightarrow 2Ar\left(^1S_0\right) + Xe\left(n = 2,\, ^2P_{\frac{3}{2}}\right) \tag{5.2}$$

Note that the excitation energy of the Wannier-Mott impurity state [82] coincides almost exactly with the peak emission wavelength of the excimer emission of pure liquid argon which could be a strong indication for an efficient energy transfer from argon to xenon. This energy transfer is illustrated in Fig. 5.1 by the blue horizontal arrow from the argon excimer emission to the perturbed Wannier-Mott impurity state of xenon-doped liquid argon. The curly vertical arrow denotes the transition which is assumed to be responsible for the newly found near-infrared emission (see, e.g., Fig. 1.8, upper panel). After a collisional deexciation of the xenon atoms to the $^3P_1$ and $^3P_2$ states, xenon excimers are formed which decay into the dissociative ground state, thereby emitting the characteristic xenon excimer radiation in the vacuum ultraviolet. Two minor emission features which were actually also observed in the emission spectra presented in the upper panel of Fig. 3.3 can also lead to a further deexcitation of the xenon atoms to the ground state. Either the formation of weakly bound ArXe* excimers [83] which lead to the weak emission feature centered at 149 nm or a direct transition of xenon ($^3P_2 \rightarrow {}^1S_0$) to the ground state and thereby emitting the characteristic resonance emission at 147 nm.

The concentration-dependent behaviour of the intense near-infrared emission with increasing xenon concentration depicted in Fig. 3.4 could be explained by the present model as follows: An increasing concentration of xenon atoms in the Wannier-Mott impurity state $\left(n = 2,\, {}^2P_{\frac{3}{2}}\right)$ in liquid argon initially leads to an increasing near-infrared signal. When the xenon-doping concentration becomes so high that the xenon atoms begin to aggregate and form clusters, the excitation energy of the Wannier-Mott impurity state $\left(n = 2,\, {}^2P_{\frac{3}{2}}\right)$ begins to rise from the value in the liquid phase ($\sim 9.8\,\mathrm{eV}$) to the value in the solid phase ($\sim 10.1\,\mathrm{eV}$ [82]) and is therefore changed to a region where the argon excimer emission becomes weaker. This could lead to a decreasing energy transfer and, thus, to a decreasing near-infrared signal with increasing xenon concentration. Here it is interesting to note that the Van-der-Waals minimum of xenon has a depth of 24 meV [61]. Integrating the Boltzmann energy distribution of xenon atoms at 86 K (liquid argon temperature) from zero to 24 meV leads to the conclusion that 91 % of all xenon atoms in xenon-doped liquid argon have a thermal energy lower than the depth of the Van-der-Waals minimum. Thus, with an increasing concentration there is a strong trend of xenon atoms to form clusters. Actually, for xenon concentrations larger than 30 ppm in pure liquid argon a xenon-aggregation has been observed [82]. This concentration is in agreement with the results obtained in the present thesis where the peak near-infrared emission has been observed with a concentration of 10 ppm xenon in liquid argon.

Furthermore, the measured time structure of the near-infrared emission and the following xenon excimer emission (see section 3.5) can also be explained qualitatively since the xenon excimer emission in the vacuum ultraviolet is a transition in a cascade following the near-infrared emission.

In this context it is also interesting to note that Borghesani and coworkers [84] discovered an intense near-infrared emission in pure high-pressure xenon gas and in a 90 % argon, 10 % xenon gaseous mixture. They detected a broad near-infrared

continuum centered at $\sim 1.3\,\mu$m. The continuum shifts towards longer wavelengths with increasing pressure. Therefore, a simple density related effect shifting the near-infrared emission from $1.3\,\mu$m in the gas phase to $1.17\,\mu$m peak wavelength in the liquid phase seems unlikely. The authors of ref. [84] propose a xenon excimer transition of highly excited xenon excimers from a bound to a repulsive state to be responsible for their observed near-infrared emission.

5.2 Proposal of Future Experiments to Address so far Unanswered Questions

To clarify the origin of the newly found near-infrared emission in xenon-doped liquid argon, selective excitation using synchrotron radiation (SR) is proposed. Exciting xenon-doped liquid argon with SR to the energy which corresponds to the perturbed $^3P_1$ xenon state and performing absorption spectroscopy with infrared radiation could lead to complementary information whether the newly-found near-infrared emission is also visible in absorption. Furthermore, laser-induced fluorescence could also be used to probe the different energy levels involved in the generation of the newly found near-infrared emission.

Between the detection of two intense scintillation signals (VUV and NIR) in xenon-doped liquid argon and an application in a liquid noble-gas particle-detector several still open questions have to be answered. At the moment probably the most important one is whether particle discrimination on an event-by-event basis using both scintillation signals is feasible and superior to state of the art liquid noble-gas particle-detectors. Exciting xenon-doped liquid argon with pulsed ion beams[2] or radioactive sources and recording the scintillation time structures and the signal ratios for different exciting particles could answer this question. The most important particle discrimination which has to be performed is between electron recoils and nuclear recoils. In terms of natural radioactivity, exciting xenon-doped liquid argon with alpha particles, electrons[3] and gammas could simulate the most abundant background sources which have already been identified in other experiments in rare-event physics. The excitation with a pulsed beam of neutrons of various energies could simulate the signals of nuclear recoils which can be expected when a WIMP transfers momentum to a target nucleus.

A further question which has to be clarified is the long-term stability of the xenon-doping in liquid argon. Detectors aiming to detect rare events usually have long measurement periods where a stable operation is mandatory. Therefore, the xenon atoms in liquid argon have to be dissolved homogeneously in liquid argon. Xenon-concentration gradients within a particle detector would lead to position-dependent

[2]To probe different linear energy transfers (LETs) similar to the experiments Doke et al. had performed [87] with pure liquid argon.

[3]The excitation of xenon-doped liquid argon with low-energy electrons has already been performed in the present thesis. However, a variation of the electron-energy could provide information about an energy dependence.

scintillation signals which would complicate the identification of different incident particles. This question could be addressed in a low-volume prototype-detector with a radioactive source and monitoring the scintillation signals over long periods of time at different positions within the detector volume.

Concerning integral light-yield optimization, the xenon concentrations should be varied in linear steps around the mixture with 10 ppm xenon in liquid argon. At 10 ppm xenon in liquid argon, the integral scintillation light intensity (VUV plus NIR) showed a maximum (see Fig. 3.13). In the present thesis the xenon concentrations in liquid argon were varied only by factors of 10. Furthermore, varying the xenon concentrations in linear steps and recording the scintillation time structures of the VUV and the NIR emissions will provide information on the rate constants for the energy transfer from liquid argon to xenon. These rate constants could also help identifying the near-infrared emitting species in xenon-doped liquid argon. A further information which can be derived from linear xenon doping is whether only one or multiple xenon atoms are involved in the processes to form the intense near-infrared emitting species. A linear signal variation with xenon concentration means that one xenon atom is involved and a quadratic signal variation with xenon concentration means that two xenon atoms are involved in the processes to form the near-infrared emitting species.

Transmission measurements of pure liquid argon to obtain the attenuation length should be performed with a longer (than 11.6 cm) sample cell to increase the sensitivity. In this context also wavelength-resolved measurements of the refractive index of pure and xenon-doped liquid argon should be performed since the refractive index is a crucial parameter when the attenuation length has to be determined with low systematic errors. To measure the refractive index of liquid argon one could, for example, use a cell containing liquid argon (similar to that in Fig. 4.1) and a pulsed VUV light source of variable frequency. If the pulse durations are short enough and the time resolution of the detector is high enough (picosecond resolution), a measurement of the speed of light in liquid argon can be used to calculate the wavelength-dependent refractive index. As an example, a light source capable of producing femtosecond pulses of synchrotron radiation in a range from the infrared to the x-ray regime is described in ref. [100].

5.3 Simultaneous Detection of the VUV and IR Emission - A Novel Concept for Particle Discrimination

The main result of the present thesis is the discovery of an intense scintillation signal from xenon-doped liquid argon in the near-infrared [68]. In addition, also an intense scintillation signal in the vacuum ultraviolet is observed [32]. A novel particle-discrimination concept using both scintillation signals simultaneously could be a promising extension (or alternative) to state of the art single-phase as well as double-phase liquid noble-gas particle-detectors (see section 1.3). In the following

section a possible concept of such a detector is presented.

In single-phase liquid noble-gas particle-detectors (see Fig. 1.2) the scintillation time structure is used for event-by-event particle discrimination. In double-phase liquid noble-gas particle-detectors (see Fig. 1.4) the charge and the scintillation light produced in an event are used to discriminate different particles. However, it has to be noted that the charge released in an event has to be drifted towards the upper gas-liquid phase-transition using a strong electrical field ($\sim 1\frac{\mathrm{kV}}{\mathrm{cm}}$). A constant electrical field requires higher voltages which cause technical challenges when the detector volumes are increased. Consequently, in a double-phase liquid-noble gas particle-detector the second signal (charge besides scintillation light) leads to technical challenges (due to high-voltage) when the sensitive detector volumes are increased.

Using xenon-doped liquid argon as the scintillator material in a particle detector instead of pure liquid argon or pure liquid xenon leads to two optically well separated scintillation signals. Both signals can be detected simultaneously on a pure optical basis and could improve the discrimination power of a particle detector. The intense VUV emission at 174 nm peak wavelength and the strong near-infrared emission at 1173 nm peak wavelength can be detected completely independent (see Fig. 3.1, lower panel) of each other since the VUV detector is "blind" in the near-infrared and the near-infrared detector is "blind" in the VUV.

A new detector concept using both emissions (VUV as well as NIR) is illustrated in Fig. 5.3. A spherically symmetric design can be used in analogy to the single-phase liquid noble-gas particle detector depicted in Fig. 1.2 to optimize the optical coverage. A high optical coverage leads to a low threshold which is crucial to compete with other experiments. In an alternating pattern, VUV and NIR detectors are mounted to detect both, the VUV emission as well as the NIR emission. The information which can be read out event-by-event is the time structure of the VUV emission, the time structure of the NIR emission and the ratio between the VUV and NIR signals. In the optimum case all three parameters can be used for particle discrimination. Compared to single-phase pure liquid-argon detectors (see e.g. Fig. 1.2) it seems that an event-by-event particle discrimination based on time information alone (pulse shape analysis, see e.g. Fig. 1.3) is not possible anymore. The time structures of both scintillation signals (VUV at 174 nm and NIR at 1182 nm) depicted in Fig. 3.15 do not exhibit time structures which can be described by two considerably different decay-time constants, which would favour an event-by-event particle identification like in pure liquid argon. It is assumed that the VUV emission is a transition in a cascade following the NIR emission. This might lead to the speculation that the time structures (VUV and NIR) will show the same trend under excitation with different particles. However, it has to be emphasized that at the moment no measurements are available which show the time structures of both (VUV and NIR) scintillation signals under particle and energy variation. A conclusive result, whether the time structure can be used as a discrimination parameter (and whether it is competitive to pure liquid argon) can only be obtained after further measurements. Therefore, further experiments have to be performed to investigate the particle-dependence of

all three[4] parameters (for more details see section 5.2) concerning the discrimination power between electron and nuclear recoils.

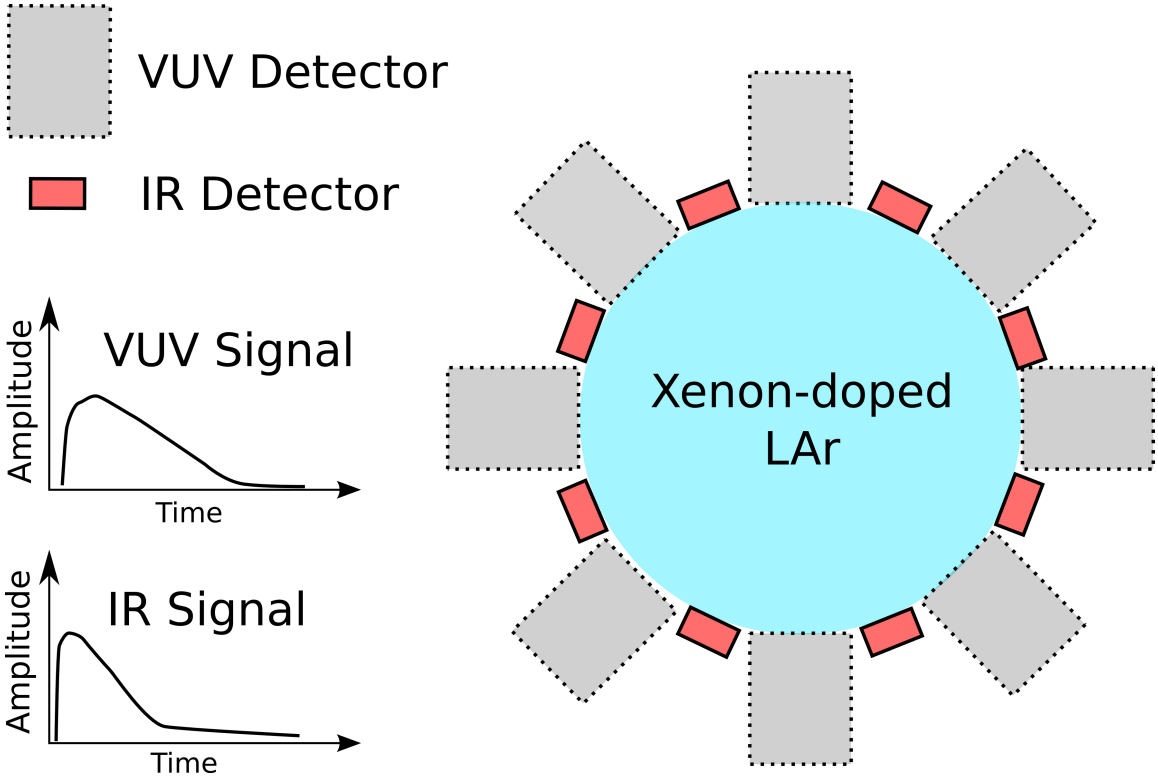

Figure 5.3: *A novel detector concept of a single-phase liquid noble-gas particle-detector is illustrated. The scintillating medium is xenon-doped liquid argon which emits scintillation light in the VUV as well as in the NIR. A spherically-symmetric detector geometry offers a high optical coverage and, thus, a low threshold. For scintillation-light detection VUV and IR detectors are mounted in an alternating pattern to record both (VUV and IR) emissions simultaneously. The time structures and the signal ratio of the VUV and the IR scintillation signal can be recorded and eventually used for event-by-event particle identification.*

For the detection of the VUV emission, photomultipliers with a photocathode sensitive down to the VUV can be used. The shift of the main emission in the VUV from the argon excimers (127 nm peak wavelength) to the xenon excimers (174 nm peak wavelength) is a benefit in two ways: Firstly, the VUV emission is shifted to a wavelength region where photomultipliers with quartz entrance-windows without wavelength shifters (e.g. the photomultipliers described in ref. [101]) can be used. Secondly, the emission is shifted to a wavelength region where xenon-doped liquid argon shows a high transmission (see Fig. 3.3). Xenon in liquid argon leads to a transmission minimum at 126.5 nm (see Fig. 4.7) which coincides almost exactly with the peak emission wavelength of pure liquid argon (127 nm). Therefore, xenon can

[4]The signal ratio of VUV and NIR signals and the time structures of the VUV and the NIR signals.

act as a critical impurity for large pure liquid argon detectors aiming to detect the scintillation light of pure liquid argon at 127 nm.

For the detection of the IR emission also photomultipliers can be used (e.g. the same NIR-PMT as in the present experiments, see Fig. 2.16). However, one major drawback at the moment is the price compared to conventional photomultipliers. An alternative could be solid state detectors based on semiconductors with an appropriate band gap to detect infrared emission with a peak wavelength at $\sim 1.17\mu$m (e.g. InGaAs). To compare the performance of different solid state materials for their application as an infrared detector the so-called specific detectivity D^* [102, 103] is introduced according to equation 5.3:

$$\mathrm{D}^* = \frac{\sqrt{\mathrm{A}}}{\mathrm{NEP}} \tag{5.3}$$

$$\mathrm{NEP} = \frac{\mathrm{P}}{\frac{\mathrm{S}}{\mathrm{N}} \cdot \sqrt{\Delta \mathrm{f}}} \tag{5.4}$$

D^*: Specific detectivity $[\frac{\mathrm{cm}\cdot\sqrt{\mathrm{Hz}}}{\mathrm{W}}]$

A: Area of the photosensitive region [cm^2]

NEP: Noise-equivalent power $\left[\frac{\mathrm{W}}{\sqrt{\mathrm{Hz}}}\right]$

Δf: Bandwidth [Hz]

P: Power of incident radiation [W]

$\frac{\mathrm{S}}{\mathrm{N}}$: Signal-to-noise ratio

A descriptive way to interpret the noise-equivalent power (NEP) of a detector is as follows: Assume a light flux irradiates a photosensitive detector with a constant optical power. The signal from the detector (either voltage or current) is sampled at a certain sampling rate. To measure the signal with a bandwidth of 1 Hz the sampled values have to be averaged over a time[5] of 0.5 s. If the signal-to-noise ratio (average value divided by the standard deviation) of the sampled values equals 1, the incoming optical power equals the noise-equivalent power. Briefly, the noise-equivalent power is the power of incident light equal to the intrinsic noise of a detector, or in other words, it is the power of incident light which is needed to produce an output signal with a signal-to-noise-ratio equal to 1. Therefore, a low noise-equivalent power characterizes a detector with a high sensitivity. The specific detectivity D^* is the square root of the photosensitive area divided by the noise-equivalent power. Consequently, a higher specific detectivity indicates a higher sensitivity of the corresponding detector material.

Fig. 5.4 shows an overview of the specific detectivity D^* of different materials used to detect infrared radiation (here, as an example, offered by Hamamatsu Photonics

[5]The factor of 0.5 is due to the Nyquist-Shannon sampling theorem.

[104]). The peak wavelength of the near-infrared emission from xenon-doped liquid argon is at $\sim 1.17\mu$m (see Fig. 1.8, upper panel and Fig. 3.5). The InAs infrared photodiode (see Fig. 2.12) which has been used in the present thesis has a wider sensitive wavelength region (see Fig. 2.13) compared to InGaAs. However, in the wavelength region where xenon-doped liquid argon scintillates, InGaAs has a specific detectivity which is a factor of $\sim$ 30 higher than the specific detectivity of InAs. Therefore, the most promising material for the detection of the NIR emission from xenon-doped liquid argon in a particle detector is InGaAs. However, note that these solid state detectors have to be segmented to cover large areas in a particle detector. A larger sensitve area causes higher electronic noise and, thus, the signal-to-noise ratio decreases. One could also think of segmented InGaAs avalanche photodiodes for single photon detection.

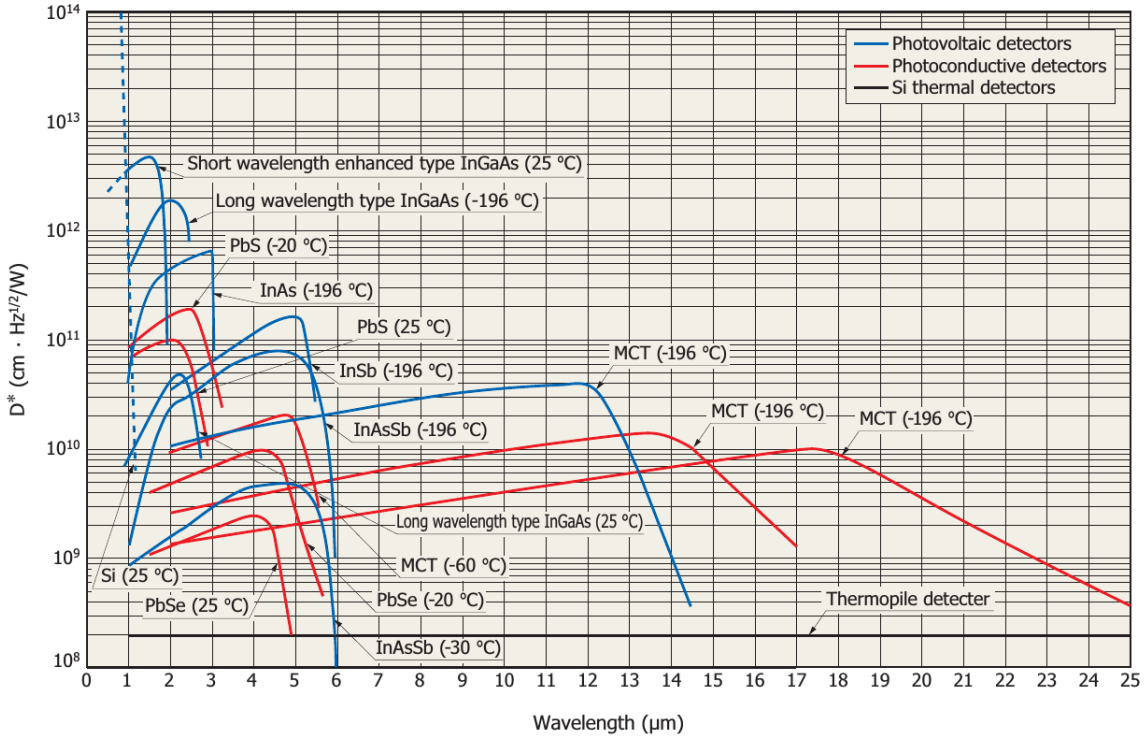

Figure 5.4: *The specific detectivity D^* of various detector materials used for the detection of infrared radiation is presented for a large wavelength range. The peak emission wavelength of xenon-doped liquid argon is at $\sim 1.17\,\mu m$ (compare Fig. 1.8, lower panel and Fig. 3.5). Compared to the InAs photodiode which has also been used in the present thesis (see Fig. 2.12) InGaAs has a ~ 30 times higher specific detectivity at the peak scintillation wavelength of xenon-doped liquid argon. Therefore, InGaAs is the most promising detector material to be used in a liquid noble-gas particle-detector to record infrared scintillation light from xenon-doped liquid argon. This figure is adapted from the selection guide for infrared detectors from Hamamatsu Photonics[104].*

Chapter 6

Summary and Outlook

Liquid noble gases are highly efficient scintillators which are used as scintillator material in particle detectors. From the last decades until now liquid noble gases have gained a lot of attention. Especially in the sector of rare-event physics such as the direct search for dark matter, high-energy neutrino physics, and the search for the neutrinoless double-beta decay, liquid noble gases are used extensively. A detection of these rarely occurring events relies on a detailed understanding of the background which is orders of magnitude higher than the expected signal rates induced by rare events. Therefore, an event-by-event particle discrimination is necessary which requires a profound knowledge of the scintillation properties of the detector material.

The main goal of the present thesis is a detailed investigation of the scintillation properties of xenon-doped compared to pure[1] liquid argon. The scintillation of pure and xenon-doped liquid argon has been investigated wavelength and time resolved. The excitation of the noble-gas samples was based on a low-energy (12 keV) electron beam sent through a 300 nm thin ceramic membrane into the liquid noble-gas samples. The scintillation light was analyzed with a VUV monochromator (McPherson 218) and detected over a wide wavelength range from 115 - 3500 nm using different detectors. For the vacuum ultraviolet, ultraviolet, and visible wavelength regions, a photomultiplier (sensitive from 115 - 850 nm) with S20 cathode and MgF_2 entrance window was used. The visible and infrared wavelength regions were scanned using an InAs photodiode with preamplifier in a lock-in configuration sensitive from 500 - 3500 nm. For high-resolution and time-resolved measurements in the infrared a near-infrared photomultiplier with InGaAsP/InP cathode sensitive from 950 - 1350 nm was used. Time-resolved scintillation data were obtained by pulsing the electron beam with a pulse duration of 100 ns and recording the time evolution of the scintillation light at selected wavelength positions.

Pure liquid argon shows a dominating scintillation signal in the vacuum ultraviolet at 127 nm peak wavelength (FWHM: 7.4 nm) which can be attributed to the well-known second excimer continuum of argon [44]. Doping pure liquid argon with xenon

[1] The scintillation of pure liquid argon has already been investigated in former works [39, 40, 41, 44]. However, for a direct comparison under the same experimental conditions these measurements were repeated to some extent using the present experimental setup.

leads to a shift of the main emission from the argon excimers to the xenon excimers at 174 nm peak wavelength (FWHM: 8.6 nm). This happens already at very low xenon concentrations of the order of ppm (see Figs. 3.2 and 3.3). In addition, an intense asymmetrically shaped scintillation feature in the near-infrared at 1173 nm peak wavelength (FWHM: 99 nm) appears (see Fig. 3.4). At a concentration of 10 ppm xenon in pure liquid argon the near-infrared emission shows maximal intensity and the energy transfer in the vacuum ultraviolet from argon to xenon is almost complete (86 % compared to a 1000 ppm xenon in liquid argon mixture, see Fig. 3.13). The 10 ppm mixture also shows maximal integral (vacuum ultraviolet plus near-infrared) light emission. High-resolution measurements with the near-infrared photomultiplier allowed the detection of two minor scintillation features in xenon-doped (10 ppm) liquid argon with peak wavelengths of 964 and 1024 nm.

To judge whether an application of both (VUV and NIR) emission features in a liquid noble-gas particle-detector is feasible, the scintillation efficiencies have been measured. Under the present experimental conditions pure liquid argon shows a scintillation efficiency of (22 000±3 000) photons per MeV electron energy deposited. The vacuum ultraviolet emission in xenon-doped (10 ppm) liquid argon has a scintillation efficiency of (20 000±6 000) photons per MeV electron energy deposited and the simultaneously emitted near-infrared emission has a scintillation efficiency of (13 000±4 000) photons per MeV electron energy deposited. Consequently, xenon-doped liquid argon shows two intense and spectrally well-separated scintillation signals with comparable scintillation efficiencies. Under the present experimental conditions the conversion efficiency of electron-beam power to excimer light is (21 ± 3) % for pure liquid argon. In xenon-doped liquid argon the integral (vacuum ultraviolet + near-infrared) conversion efficiency from electron-beam power to light is (15.3±4.4) %. An overview spectrum from the vacuum ultraviolet to the infrared comparing pure liquid argon and liquid argon doped with 10 ppm xenon can be seen in Fig. 3.1.

The time structure of both scintillation signals of liquid argon doped with 10 ppm xenon has also been investigated (see Fig. 3.15). The results obtained so far show that both emission features have a rather fast time structure with an overall duration of $\sim 2\,\mu$s for the vacuum ultraviolet emission and of $\sim 1.2\,\mu$s for the near-infrared emission. The duration of both scintillation signals is well suited for a particle detector since no intense and long-living components are involved which might increase the noise and the dead time of a particle detector. From a first tentative interpretation of the data it seems that the vacuum ultraviolet emission is a transition in a cascade following the near-infrared emission. However, so far no detailed model can be presented due to the lack of information on the rate constants concerning the energy transfer from argon to xenon. The time constants which have been fitted to the data for a phenomenological description are discussed in section 3.5. In terms of event-by-event particle discrimination it seems that a particle identification analogous to pure liquid argon using the singlet-to-triplet ratio of the excimer molecules is not possible anymore. However, detailed investigations of the scintillation properties of xenon-doped liquid argon under variation of the exciting particles have to be performed to obtain a conclusive result. The time structure of the near-infrared emission has been

measured at five different wavelength positions (see Fig. 3.5). On the current level of sensitivity and the statistics which has been collected no wavelength-dependent time structure within the near-infrared emission has been observed.

A tentative assignment of the newly found near-infrared emitting species in xenon-doped liquid argon is also presented and attributed to a transition from a Wannier-Mott impurity state to a perturbed atomic xenon state. The Wannier-Mott impurity state has no parentage in pure gaseous xenon. The model can explain qualitatively the xenon-concentration dependence, the observed time structure, and the emission wavelength.

Besides the emission features of pure and xenon-doped liquid argon also the transmission has been measured wavelength resolved. The transmission of a sample with a certain length is the parameter which has to be determined in an experiment to calculate the attenuation length. The attenuation length is a figure of merit for the transparency of a scintillator for its own scintillation light and describes the length after which the initial scintillation-light intensity has decreased by a factor of $\frac{1}{\mathrm{e}}$. The attenuation length becomes an important parameter for particle detectors with large sensitive volumes where the scintillation light has to traverse long optical path lengths until it is detected.

A basic optical setup (see Fig. 4.1) with light from a deuterium arc lamp traversing a 11.6 cm long sample cell allowed to measure the transmission of pure and xenon-doped liquid argon. Various systematic effects (see section 4.2) artificially increasing the measured transmission could be identified, quantified and corrected. The measured transmission of pure liquid argon was so high that only a lower limit of 1.10 m for the attenuation length of pure liquid argon for its own scintillation light can be given at present. To increase the sensitivity a sample cell with a length of the order of one meter would be needed. A further reduction of the systematic errors could be obtained when wavelength-resolved measurements of the refractive index of pure liquid argon would become available.

Doping liquid argon with xenon leads to three broad absorption bands centered at 122.2, 126.5 and 140.0 nm. The transmission minima at 122.2 and 140.0 nm can be attributed to perturbed ($\sim$ 7 nm blue shifted) n=1 ($^2P_{\frac{1}{2}}$) and n=1 ($^2P_{\frac{3}{2}}$) atomic xenon states [82]. The third transmission minimum is centered at 126.5 nm and can be attributed to a n=2 ($^2P_{\frac{3}{2}}$) trapped exciton (Wannier-Mott) impurity state [82] which has no parentage in the states of isolated xenon atoms. Increasing the xenon concentration leads to a broadening of the 140 nm absorption band. The 126.5 nm absorption band becomes completely opaque below 130 nm for xenon concentrations higher than 0.1 ppm and an optical path length of 11.6 cm. Especially the transmission minimum centered at 126.5 nm is critical for pure liquid argon detectors since it coincides almost exactly with the peak emission wavelength of pure liquid argon. Therefore, xenon can act as a critical impurity for pure liquid argon detectors and can easily be underestimated. A simple conventional chemical purification of the detector medium can not remove xenon. Therefore, an examination of the argon gas for traces of xenon prior to filling the scintillator volume of a particle detector is strongly recommended. A calibration curve showing the equivalent widths of the

140 nm transmission minimum versus column density of xenon atoms in liquid argon is provided for that purpose (see Fig. 4.8).

Comparing the emission with the transmission of xenon-doped liquid argon (see Fig. 3.3) shows that the main emission in the VUV is shifted to a wavelength region where xenon-doped liquid argon is highly transparent. Furthermore, the main emission in the vacuum ultraviolet is shifted to a wavelength region where photomulipliers generally become more sensitive due to the responsivities of the photocathodes and the transmission of the window materials used.

The last part (section 5) of the present work focuses on a proposal for a detector concept using both emissions of xenon-doped liquid argon simultaneously to improve the particle-discrimination performance. However, from the discovery to an application of the newly found near-infrared emission, several issues have to be clarified which are also discussed in detail. Experiments to address so far unanswered questions are proposed.

Appendix

List of abbreviations

Al-MgF$_2$ Aluminum-coated magnesiumfluoride

BK7 Borosilicate glass

G1 Grating number one (1200 $\frac{\text{Lines}}{\text{mm}}$, Blaze wavelength: 150 nm)

G3 Grating number three (300 $\frac{\text{Lines}}{\text{mm}}$, Blaze wavelength: 1 μm)

EPL Europhysics Letters

FWHM Full width at half maximum

GAr Gaseous argon

GEANT4 Geometry and Tracking, Simulation toolkit for the passage of particles through matter

InAs Indium arsenide

InGaAs Indium gallium arsenide

InGaAsP Indium gallium arsenide phosphide

InP Indium phosphide

IR Infrared

LAr Liquid argon

LiF Lithium fluoride

LN$_2$ Liquid nitrogen

LNG Liquid noble gas

LTP Classical left turning point

LXe Liquid xenon

NIR Near-infrared

NIR-PMT Near-infrared photomultiplier

NIST National Institute of Standards and Technology

MgF_2 Magnesiumfluoride

PMT Photomultiplier

PPM Parts per million

PTB Physikalisch-Technische Bundesanstalt

Si_3N_4 Silicon nitride

SiO_2 Silicon oxide

SR Synchrotron radiation

TPC Time projection chamber

VIS Visible wavelength region

VUV Vacuum ultraviolet

VUV-PMT Vacuum ultraviolet photomultiplier

WIMP Weakly interacting massive particle

List of Figures

Bibliography

[1] Y. Tanaka and M. Zelikoff. *"Continuous Emission Spectrum of Xenon in the Vacuum Ultraviolet Region". JOSA,* ***44*** *3 pp. 245-255*, 1954.

[2] Y. Tanaka. *"Continuous Emission Spectra of Rare Gases in the Vacuum Ultraviolet Region". JOSA,* ***45*** *9 pp. 710-713*, 1955.

[3] Y. Tanaka. *"Continuous Emission Spectrum of Neon in the Vacuum Ultraviolet Region". JOSA,* ***47*** *1 pp. 105-105*, 1957.

[4] Y. Tanaka, A. S. Jursa and F. J. Leblanc. *"Continuous Emission Spectra of Rare Gases in the Vacuum Ultraviolet Region. II. Neon and Helium". JOSA,* ***48*** *5 pp. 304-307*, 1958.

[5] Y. Tanaka and A. S. Jursa. *"Combining of the Rare-Gas Continua". JOSA,* ***50*** *11 pp. 1118-1119*, 1958.

[6] N. G. Basov et al. *"Laser for vacuum region of the spectrum with excitation of liquid xenon by an electron beam". Zh. Eksp. Fiz. i Tekh. Pisma. Red. Nr.* ***12****, 473*, 1970.

[7] N. G. Basov et al. *"Laser Operating in the Vacuum Region of the Spectrum by Excitation of Liquid Xenon with an Electron Beam". JETP Letters* ***12****, 329*, 1970.

[8] Rhodes Ch. K. and BRAU C. *"Excimer Lasers". Springer Verlag, Berlin, Germany*, 1984.

[9] A. Ulrich. *"Light emission from particle beam induced plasma: An overview". Laser and Particle Beams* ***30****, 2 pp. 199-205*, 2012.

[10] J. Wieser et al. *"Vacuum ultraviolet rare gas excimer light source". Rev. Sci. Instrum.* ***68*** *1360*, 1997.

[11] A. Ulrich et al. *"Anregung dichter Gase mit niederenergetischen Elektronenstrahlen". Physikalische Blätter* ***56****, Nr. 6*, 2000.

[12] A. Ulrich et al. *"Electron beam induced light emission". Eur. Phys. J. Appl. Phys.* ***47****, 22815*, 2009.

[13] A. Ulrich. *"Private Communication"*. 2014.

[14] A. Morozov et al. *"Conversion efficiencies of electron beam energy to vacuum ultraviolet light for Ne, Ar, Kr, and Xe excited with continuous electron beams"*. *J. Appl. Phys.* ***103*** *103301*, 2008.

[15] E. Aprile et al. *"Noble gas detectors"*. *Wiley-VCH Verlag GmbH und Co KgaA., Weinheim Germany*, 2006.

[16] The ArDM collaboration. *"Status of the ArDM Experiment: First results from gaseous argon operation in deep underground environment"*. *arXiv:1307.0117v1 [physics.ins-det]*, 2013.

[17] DarkSide Collaboration. *"First Results from the DarkSide-50 Dark Matter Experiment at Laboratori Nazionali del Gran Sasso"*. *arXiv:1410.0653v1 [astro-ph.CO]*, 2014.

[18] K. Rielage et al. *"Update on the MiniCLEAN Dark Matter Experiment"*. *arXiv:1403.4842v1 [physics.ins-det]*, 2014.

[19] M.G. Boulay, for the DEAP Collaboration. *"DEAP-3600 Dark Matter Search at SNOLAB"*. *J. Phys.: Conf. Ser.,* ***375*** *012027*, 2012.

[20] P. Gorel, for the DEAP Collaboration. *"Search for Dark Matter with Liquid Argon and Pulse Shape Discrimination: Results from DEAP-1 and Status of DEAP-3600"*. *arXiv:1406.0462 [astro-ph.IM]*, 2014.

[21] M. Schumann for the DARWIN consortium. *"DARWIN"*. *arXiv:1111.6251 [astro-ph.IM]*, 2011.

[22] The ICARUS Collaboration. *"ICARUS at FNAL"*. *arXiv:1312.7252v1 [physics.ins-det]*, 2013.

[23] LBNE Collaboration. *"The Long-Baseline Neutrino Experiment: Exploring Fundamental Symmetries of the Universe"*. *arXiv:1307.7335 [hep-ex]*, 2014.

[24] M. Auger et al. *"The EXO-200 detector, part I: detector design and construction"*. *JINST* ***7*** *P05010*, 2012.

[25] EXO-200 Collaboration. *"Search for Majoron-emitting modes of double-beta decay of* ^{136}Xe *with EXO-200"*. *arXiv:1409.6829v2 [hep-ex]*, 2014.

[26] J. J. Gomez-Cadenas. *"The NEXT experiment"*. *arXiv:1411.2433v1 [physics.ins-det]*, 2014.

[27] M. Agostini et al. *LArGe - Active background suppression using argon scintillation for the GERDA* $0\nu\beta\beta$*-experiment"*. *arXiv:1501.05762v1 [physics.ins-det]*, 2015.

[28] M. Schumann. *"Dark Matter Search with liquid Noble Gases". arXiv:1206.2169v1 [astro-ph.IM]*, 2012.

[29] M. Schumann. *"Dual-Phase Liquid Xenon Detectors for Dark Matter Searches". arXiv:1405.7600v2 [astro-ph.IM]*, 2014.

[30] R. Acciari et al. *"Oxygen contamination in liquid Argon: combined effects on ionization electron charge and scintillation light". JINST* ***5****, P05003 [arXiv:0804.1222 [nucl-ex]]*, 2010.

[31] T. Heindl et al. *"Table-top setup for investigating the scintillation properties of liquid argon". JINST* ***6*** *P02011*, 2011.

[32] A. Neumeier et al. *"Intense vacuum ultraviolet and infrared scintillation of liquid Ar-Xe mixtures". Europhys. Lett.* ***109*** *12001*, 2015.

[33] A. Neumeier et al. *"Attenuation of vacuum ultraviolet light in liquid argon". Eur. Phys. J. C* ***72****:2190*, 2012.

[34] W.E. Forsythe. *"Smithsonian Physical Tables". 9th revised edition, The Lord Baltimore Press, Smithsonian Institution*, 1951.

[35] M.I. Lopes and V. Chepel. *"Liquid rare gas detectors: Recent developments and applications". IEEE T. Dielect. El. In.* ***10*** *994*, 2003.

[36] R.B. Firestone. *"Table of Isotopes Eighth Edition". Wiley-Interscience, p.807*, 1996.

[37] H.O. Back et al. *"Depleted Argon from Underground Sources". Phys. Proc.* ***37*** *1105*, 2012.

[38] G. Bertone. *"The moment of truth for WIMP dark matter". Nature* ***468*** *389*, 2010.

[39] M. Hofmann. *"Liquid scintillators and liquefied rare gases for particle detectors.". Ph.D. thesis, Technische Universität München, https://mediatum.ub.tum.de/doc/1115726/1115726.pdf*, 2012.

[40] M. Hofmann et al. *"Ion-beam excitation of liquid argon". Eur. Phys. J. C* ***73****:2618*, 2012.

[41] T. Heindl. *"Die Szintillation von flüssigem Argon". Dissertation, Technische Universität München, https://mediatum.ub.tum.de/doc/1080148/1080148.pdf*, 2011.

[42] A. Neumeier. *"Optical Transmission of Liquid Argon in the Vacuum Ultraviolet". Diploma thesis, Technische Universität München*, 2012.

[43] N.G. Basov et al. *"Luminescence of condensed Xe, Kr, Ar and their mixtures in vacuum region of spectrum under excitation by fast electrons". J. Lumin.* ***12*** *834*, 1970.

[44] T. Heindl et al. *"The scintillation of liquid argon". Europhys. Lett.* ***91*** *62002*, 2010.

[45] E. Morikawa et al. *"Argon, krypton, and xenon excimer luminescence - from the dilute gas to the condensed phase". J. Chem. Phys.* ***91*** *1469*, 1989.

[46] O. Cheshnovsky, B. Raz, and J. Jortner. *"Emission Spectra of Deep Impurity States in Solid and Liquid Rare Gas Alloys". J. Chem. Phys.* ***57*** *4628*, 1972.

[47] J. Jortner et al. *"Localized Excitons in Condensed Ne, Ar, Kr, and Xe". J. Chem. Phys.* ***42*** *4250*, 1965.

[48] T. Doke et al. *"LET Depedence of Scintillation Yields in Liquid Argon". Nucl. Instr. Meth. A* ***269*** *291*, 1988.

[49] A. Fedenev et al. *"Applications of a broadband electron-beam pumped XUV radiation source". J. Phys. D Appl. Phys.* ***37*** *1586*, 2004.

[50] Kramida, A., Ralchenko, Yu., Reader, J. and NIST ASD Team. *"NIST Atomic Spectra Database (version 5.2)". National Institute of Standards and Technology, Gaithersburg, MD. online: http://physics.nist.gov/asd*, 2014.

[51] N.B. Vargaftik. *"Handbook of physical properties of liquids and gases - pure substances and mixtures". Hemisphere Pub. Corp., second edition, Washington USA*, 1983.

[52] E.A. Colbourn and A.E. Douglas. *"The spectrum and ground state potential curve of Ar_2". J. Chem. Phys.* ***65*** *1741*, 1976.

[53] A. Neumeier et al. *"Attenuation of vacuum ultraviolet light in liquid argon revisited". Nucl. Instrum. Methods Phys. Res. A, 2015, http://dx.doi.org/10.1016/j.nima.2015.07.051*, 2015.

[54] T. Dandl et al. *"Electron-beamignited, high-frequencydriven vacuum ultraviolet excimer light source". EPL-Europhys. Lett.* ***94*** *53001*, 2011.

[55] T. Möller et al. *"Oscillatory structures in bound-free fluorescence spectra of Xe_2, Kr_2 and Ar_2". Chem. Phys. Lett.* ***117*** *3*, 1985.

[56] H. Langhoff. *"The origin of the third continua emitted by excited rare gases". Opt. Commun.* ***68*** *31*, 1988.

[57] W. Krötz et al. *"Third excimer continuum of argon excited by a heavy-ion beam". Phys. Rev. A* ***43****, 6089*, 1991.

[58] J. Wieser et al. *"Novel pathways to the assignment of the third rare gas excimer continua". Opt. Comm.* ***173*** *233*, 2000.

[59] A. Hitachi et al. *"Effect of ionization density on the time-dependence of luminescence from liquid argon and xenon". Phys. Rev. B****27*** *5279*, 1983.

[60] P. Peiffer et al. *"Pulse shape analysis of scintillation signals from pure and xenon-doped liquid argon for radioactive background identification". JINST* ***3*** *P08007*, 2008.

[61] G. Nowak, L. Frey, and J. Fricke. *"Ar_2^*, Kr_2^*, Xe_2^* excimer formation from metastable and alpha-particle impact on solid rare-gas layers". J. Phys. B: At. Mol. Phys.* ***18*** *2851-2860*, 1985.

[62] J. Franck and E. G. Dymond. *"Elementary processes of photochemical reactions". Trans. Faraday Soc.* ***21*** *536*, 1926.

[63] E. Condon. *"A Theory of Intensity Distribution in Band Systems". Phys. Rev.* ***28*** *1182*, 1928.

[64] G. Bressi et al. *"Infrared scintillation in liquid Ar and Xe". Nucl. Instrum. Meth. A* ***440*** *254*, 2000.

[65] A. Buzulutskov, A. Bondar and A. Grebenuk. *"Infrared scintillation yield in gaseous and liquid argon". Europhys. Lett.* ***94*** *52001*, 2011.

[66] A. Bondar et al. *"Study of infrared scintillations in gaseous and liquid argon. Part I: methodology and time measurements". JINST* ***7*** *P06015*, 2012.

[67] A. Bondar et al. *"Study of infrared scintillations in gaseous and liquid argon. Part II: light yield and possible applications". JINST* ***7*** *P06014*, 2012.

[68] A. Neumeier et al. *"Intense infrared scintillation of liquid Ar-Xe mixtures". Europhys. Lett.* ***106*** *32001*, 2014.

[69] A. Morozov et al. *"Transmission of $\sim 10\,keV$ electron beams through thin ceramic foils: Measurements and Monte Carlo simulations of electron energy distribution functions". Eur. Phys. D.* ***48*** *383*, 2008.

[70] S. Agostinelli et al. *"GEANT4 - a simulation toolkit". Nucl. Instrum. Meth. A* ***506****, 250*, 2003.

[71] McPherson Inc.
http://www.mcphersoninc.com/spectrometers/vuvuvvis/model218.htm,
retrieved 2015-03-17.

[72] Edited by J.A.R. Samson and D.L. Ederer. *"Vacuum Ultraviolet Spectroscopy I". Academic Press, San Diego*, 1998.

[73] M. Antonello et al. *"Detection of Cherenkov light emission in liquid argon". Nucl. Instrum. Meth. A* ***516****, 348*, 2004.

[74] A. Bideau-Mehu et al. *"Measurement of Refractive Indices of Neon, Argon, Krypton and Xenon in the 253.7-140.4 nm Wavelength Range. Dispersion Relations and Estimated Oscillator Strengths of the Resonance Lines". J. Quant. Spectrosc. Radiat. Transfer* ***25****, 395*, 1981.

[75] P. Laporte et al. *"Vacuum-ultraviolet refractive index of LiF and MgF_2 in the temperature range 80-300 K". JOSA,* ***73*** *8 pp. 1062-1069*, 1983.

[76] Korth Kristalle GmbH. http://www.korth.de/index.php/material-detailansicht/items/21.html, retrieved 2014-12-10.

[77] McPherson Inc. http://www.mcphersoninc.com/reflectivity.htm, retrieved 2014-12-10.

[78] McPherson Inc. http://www.mcphersoninc.com/howtoselectagrating.htm, retrieved 2015-01-26.

[79] Korth Kristalle GmbH. http://www.korth.de/index.php/material-detailansicht/items/5.html, retrieved 2014-12-10.

[80] C.J. Gerritsma and J.H. Haanstra. *"Infrared transmission of air under laboratory conditions". Infrared Physics* ***10*** *79-90*, 1970.

[81] Korth Kristalle GmbH. http://www.korth.de/index.php/material-detailansicht/items/28.html, retrieved 2014-12-11.

[82] B. Raz and J. Jortner. *"Experimental evidence for trapped exciton states in liquid rare gases". Proc. Roy. Soc. Lond. A* ***317*** *113-131*, 1970.

[83] G. Nowak and J. Fricke. *"The heteronuclear excimers $ArKr^*$, $ArXe^*$ and $KrXe^*$". J. Phys. B: At. Mol. Phys.* ***18*** *1355-1367*, 1985.

[84] A. Borghesani et al. *"Infrared fluorescence of Xe_2 molecules in electron/proton beam excited pure Xe gas and in Ar/Xe gas mixture". J. Chem. Phys.* ***115****, 13*, 2001.

[85] A. Borghesani et al. *"Environmental influence on the IR fluorescence of Xe_2^* molecules in electron beam excited Ar-Xe mixture at high density". Eur. Phys. J. D* ***35****, 299*, 2005.

[86] T. Doke et al. *"Estimation of absolute photon yields in liquid argon and xenon for relativistic (1 MeV) electrons". Nucl. Instrum. Meth. A* ***291****, 617*, 1990.

[87] T. Doke et al. *"Absolute Scintillation Yields in Liquid Argon and Xenon for Various Particles". Jpn. J. Appl. Phys.* ***41*** *(2002), 1538*, 2002.

[88] A. Hitachi, T. Doke and A. Mozumder. *"Luminescence quenching in liquid argon under charged-particle impact: Relative scintillation yield at different linear energy transfers". Phys. Rev. B* ***46****, 18*, 1992.

[89] S. A. Payne et al. *"Nonproportionality of scintillator detectors: Theory and experiment II". IEEE Trans. Nucl. Sci.* ***58****, 3392*, 2011.

[90] A. Braem et al. . *"Performance of a liquid xenon calorimeter cell". Nucl. Instrum. Meth. A* ***326*** *325-331*, 1993.

[91] N. Ishida et al. *"Measurement of attenuation length of scintillation light in liquid xenon". Nucl. Instrum. Meth. A* ***327*** *152-154*, 1993.

[92] N. Ishida et al. *"Attenuation length measurements of scintillation light in liquid rare gases and their mixtures using an improved reflection suppresser". Nucl. Instrum. Meth. A* ***384*** *380-386*, 1997.

[93] V.Y. Chepel et al. . *"Purification of liquid xenon and impurity monitoring for a PET detector". Nucl. Instrum. Meth. A* ***349*** *500-505*, 1994.

[94] A. Neumeier et al. *"Attenuation of vacuum ultraviolet light in pure and xenon-doped liquid argon - An approach to an assignment of the near-infrared emission from the mixture". Europhys. Lett.* ***111*** *12001*, 2015.

[95] Opto Diode Corp,
750 Mitchell Road, Newbury Park, California 91320. *"Model: AXUV20A". http://optodiode.com/pdf/AXUV20A.pdf, retrived 2015-01-28.*

[96] M. Blackman and N. D. Lisgarten. *"The Cubic and Other Structural Forms of Ice at Low Temperature and Pressure". Proc. Roy. Soc.* ***239*** *93*, 1957.

[97] R. Onaka and T. Takahashi. *"Vacuum UV Absorption Spectra of Liquid Water and Ice". J. Phys. Soc. Jap.* ***24*** *548*, 1968.

[98] G.M. Seidel, R.E. Lanou, and W. Yao. *"Rayleigh scattering in rare-gas liquids". Nucl. Instrum. Meth. A* ***489*** *189*, 2002.

[99] A. Gedanken et al. *"Elecronic energy transfer phenomena in rare gases". J. Chem. Phys.* ***57*** *8, 3456*, 1972.

[100] R. W. Schoenlein et al. *"Generation of Femtosecond Pulses of Synchrotron Radiation". Science* ***24****, 287*, 2000.

[101] K. Lung et al. *"Characterization of the Hamamatsu R11410-10 3-in. photomultiplier tube for liquid xenon dark matter direct detection experiments". Nucl. Instrum. Meth. A* ***696****, 32*, 2012.

[102] R. C. Jones. *"Quantum efficiency of photoconductors". Proc. IRIS* ***2****, 9*, 1957.

[103] R. C. Jones. *"Proposal of the detectivity D** for detectors limited by radiation noise". J. Opt. Soc. Am.* ***50****, 1058*, 1960.

[104] Hamamatsu Photonics K.K., Solid State Division, 1126-1, Ichino-cho, Higashi-ku, Hamamatsu City, 435-8558, Japan. *"Infrared Detectors - Selection guide - March 2013". http://www.hamamatsu.com/resources/pdf/ssd/infrared_kird0001e.pdf, retrived 2015-02-08.*

Danksagung

Nun ist die Zeit gekommen, dass ich mich bei bestimmten Leuten, die das Eine oder Andere zum Gelingen dieser Arbeit beigetragen haben, bedanke. So eine Arbeit entsteht ja nicht im stillen Kämmerlein bzw. im luftleeren Raum, sondern unter Anderem auch durch ein gewisses Maß an Interaktion mit anderen Personen.

Als erstes möchte ich mich bei Prof. Dr. Stefan Schönert dafür bedanken, dass er mir diese Arbeit überlassen hat und mich am Lehrstuhl E15 aufgenommen hat. Vielen Dank für das Vertrauen und die Möglichkeit mich wissenschaftlich, kulturell und persönlich weiter zu entwickeln. Die Summer School am SNOLAB und die Konferenz in Tomsk sollen hier als Highlights genannt werden.

Ein riesengroßer Dank geht an PD Dr. Andreas Ulrich, der es mir durch seine angenehm lockere Art ermöglicht hat Wissenschaft auf einem hohen Niveau mit jugendlicher Neugier an der eigentlichen Sache zu kombinieren. Dein schier unerschöpfliches Wissen über Optik im Allgmeinen und VUV Optik im Besonderen ersparte mir eine Menge Probleme und erlaubte eine überaus effiziente Bearbeitung der Kernthemen.

Ein sehr großer Dank geht an meinen Bürokollegen und Freund Thomas Dandl. Danke für die Zeit, die wir miteinander geforscht, gelacht und (über was auch immer...) diskutiert haben. Danke für deine stetige Hilfsbereitschaft in allen Belangen des Laboralltags. Danke dafür, dass du das ganze Papier, was ich im Laufe dieser Zeit geschwärzt habe, Korrektur gelesen hast und für deine geduldigen und gerechtfertigten Korrekturvorschläge, die bei mir manchmal etwas mehr Zeit brauchten, um zu reifen. ... Aber so soll Wissenschaft ja sein, hab ich mal gelesen :-).
Fast hätte ich es vergessen:
Danke für deinen Beitrag zur Zukunft der Laserphysik in Russland!

Ein ganz herzlicher Dank geht an Andreas Himpsl. Mit dir bekommt das Thema einen würdigen Nachfolger, der mit großem Durchhaltevermögen gesegnet ist, was eine absolut essenzielle Eigenschaft eines Wissenschaftlers ist. Vielleicht kannst du das Thema ja bis zu einer größeren Anwendung treiben. Ruf mich doch bitte vorher an, wenn es soweit ist, damit ich es nicht erst aus dem Fernsehen erfahren muss :-).

Diesen kurzen Abschnitt widme ich Dr. Walter Potzel. Es ist nicht zuletzt dein Verdients, dass die ganzen Publikationen, welche in den letzten vier Jahren entstanden sind, zügig ohne große Referee Kommentare veröffentlicht wurden. Deine Erfahrungen und deine Kentnisse in der Beurteilung wissenschaftlicher Texte sind gelinde gesagt extrem wertvoll. Ich hoffe du bleibst dem Lehrstuhl noch lange erhalten und "potzelst" noch viele Arbeiten :-).

Ein großer Dank geht an Dr. Martin Hofmann, Dr. Thomas Heindl und Dr. Jochen Wieser. Dir Martin danke ich für die hervorragende Betreuung als Werkstudent und Diplomand. Ich denke, dass auch dein Verdienst in diesen Seiten verankert ist. Thomas, vielen Dank, dass du so eine erstklassige Apparatur gebaut hast. Jochen, vielen Dank für den tollen Aufenthalt in Russland, die sehr guten Kommentare und Hilfestellungen und deine einfach angenehme Art.

Vom Lehrstuhl E15 möchte ich mich besonders bei Dominikus Hellgartner bedanken. Deine Hilfsbereitschft in Software- und Hardware Angelegenheiten kann man nicht hoch genug einschätzen.

Ein nicht minder großer Dank geht an Hermann Hagn. Vielen Dank für Ihre stetige Hilfsbereitschaft in elektronischen Angelegenheiten. Durch Sie lernte ich sehr viel über Analogelektronik und elektronisches Rauschen. Ich empfehle der TUM dringend, eine Vorlesung über die Grundlagen der Analogmesstechnik mit Ihnen als Dozent anzubieten. Ihre praktischen Tipps und Tricks, wenn es um die Messung von kleinen Signalen, bzw. die Verbesserung des Signal/Noise Verhältnisses ging, sind von unschätzbarem Wert. Vielen Dank!

Bei Sabine Roth möchte ich mich für die Hilfe und die Erklärungen zu den Quenching Prozessen in Szintillatoren bedanken. Vielen Dank, dass du mitgeholfen hast. Es war stets eine angenehme Arbeitsatmosphäre.

Bei Andrea Münster und Victoria Wagner möchte ich mich für den schönen Aufenthalt bei der Summer School am SNOLAB in Kanada bedanken. Es freut mich, dass ihr dabei wart.

Michael Franke, Vincenz Zimmer und Andreas Zöller: Danke für die tollen Gespräche und eure angenehme Art.

In diesem Sinne möchte ich mich auch beim technischen Personal, vor allem der E15 Werkstatt und den Leuten von der Beschleunigerwerkstatt bedanken. Ohne eure stets hilfsbereite Art ist so eine Arbeit überhaupt nicht möglich. Vielen Dank Harry, Erich, Thomas, Fritz und Georg.

Ich bedanke mich auch bei Maria Bremberger und Sabine Kaps. Bei euch funktionierte die Zusammenarbeit stets tadellos und der Gang zum Sekretariat war nie unangenehm.

Es gibt natürlich auch abseits der Physik eine Menge Menschen, die einen Dank verdient haben:

Als erstes kann ich hier den EV Aich nennen:
Ohne die Abwechslung und den Sport mit tollen unkomplizierten Leuten als Ausgleich wäre diese Arbeit mit Sicherheit nicht möglich gewesen. Hervorheben möchte ich hier Stefan Bruckmaier, Andreas Schmid, Andreas Weinberger und Raphael Wild. Ihr seid meine coole Truppe für Trainings- und Auswärtsfahrten. Ich hatte in den letzten 20 Jahren, die ich jetzt schon spiele, noch nie so tolle unkomplizierte Mitspieler. Danke!

Im privaten Freundeskreis möchte ich mich bei Philipp Welter, Florian Tristl, Manfred Wild und Thorsten Donhauser bedanken. Die Schafkopfrunden, die Hartz-IV Tage, die Grillfeiern am Weiher und einfach alles - Genial und danke für die schönen Momente! Die Mittwochsfußballer, die Ski- und Snowboardtruppe und die Mountainbike-Mitfahrer seien hier auch erwähnt. Es hat immer Spaß gemacht.

Ein großer Dank geht an Evelyne und Heinz Bauer. Danke für die Unterstützung und die familiäre Atmosphäre auch während schwieriger Zeiten!

Diesen Absatz widme ich dir liebe Rebekka. Dein Verständnis und dein Rückhalt haben einen Großteil zum Gelingen dieser Arbeit beigetragen. Danke für deine Hilfe und deine aufmunternden Worte, vor allem in schwierigen Zeiten.

Der letzte, aber größte Dank geht an meine Eltern. Durch euch habe ich diesen Weg überhaupt erst einschlagen können. Ohne eure Unterstützung und eure Geduld würde ich diese Zeilen jetzt nicht schreiben. Danke für Alles, was ihr mir gegeben habt!

Zuletzt bin ich dankbar für einen kosmisch nicht näher definierbaren Zufall, dass ich in einer gesunden friedlichen Umgebung geboren bin und aufwachsen durfte. Diese machte es überhaupt erst möglich, mich auf die Wissenschaft zu konzentrieren. Ich schätze die Wahrscheinlichkeit in einem ärmeren Land mit schlechterer Infrastruktur oder in einem Krisengebiet geboren zu werden relativ hoch ein, im Vergleich dazu hier geboren zu werden. Ich danke daher der Familie und allen lieben Freunden, die mich auf dem Weg in einen neuen Lebensabschnitt begleiten.

Bescheidenheit schickt sich für den Gelehrten,
aber nicht für die Ideen, die in ihm wohnen
und die er verteidigen soll.
- M. Curie (1867 - 1934)